

Study of Quality and Field Limitation of  
Superconducting 1.3 GHz 9-Cell  
RF-Cavities at DESY

by

Felix Schlander



Study of Quality and Field Limitation of  
Superconducting 1.3 GHz 9-Cell  
RF-Cavities at DESY

**Dissertation**

zur Erlangung des Doktorgrades  
des Fachbereichs Physik  
der Universität Hamburg

vorgelegt von

FELIX SCHLANDER

aus Lindenfels

Hamburg  
2012

Gutachter der Dissertation:	Prof. Dr. Eckhard Elsen Dr. Bernhard Schmidt
Gutachter der Disputation:	Prof. Dr. Eckhard Elsen Dr. Jens Osterhoff
Datum der Disputation:	20.12.2012
Vorsitzende des Prüfungsausschusses:	Prof. Dr. Caren Hagner
Vorsitzender des Promotionsausschusses:	Prof. Dr. Peter Hauschildt
Dekan der MIN Fakultät:	Prof. Dr. Heinrich Graener
Leiterin des Department Physik:	Prof. Dr. Daniela Pfannkuche

## Abstract

The European XFEL and the International Linear Collider are based on superconducting rf cavities made of niobium. Their advantages are low ohmic losses which allow high duty cycles and the possibility to use a large beam aperture which is substantial to prevent wake fields at high current accelerators. To reach the theoretical limits of superconducting cavities, it is required to understand the present performance limitations. These are field emission, thermal breakdown (quench) and the ohmic losses dependent on the accelerating field, which are expressed in the quality factor. As the limiting mechanisms themselves are understood in general, the origin of the quench is often unclear.

To determine the quench locations, a localisation tool for thermal breakdown using the second sound in superfluid helium has been installed at the cavity test facility at DESY and the results for a sample of about 30 cavities have been examined. The features of the distribution of the quench locations have been analysed and it has been found that the quench locations are in the area of the highest surface magnetic field and not necessarily at the equator of the cells.

The data sample has been extended in an attempt to characterise the average behaviour of the quality factor related to the accelerating field. An analysis of the surface resistance of individual cavities shows that a recently developed model for the surface resistance of niobium is not able to describe the measurement in all detail, but the application of an additional mechanism showed promising results.

## Zusammenfassung

Der European XFEL und der International Linear Collider basieren auf supraleitenden Hochfrequenz-Beschleunigungsstrukturen aus Niob, die im Betrieb nur sehr geringe Verlustleistungen aufweisen. Diese Kavitäten erlauben eine hohe relative Einschaltdauer und eine große Öffnung für den Teilchenstrahl zur Vermeidung von an den Wänden induzierten Feldern bei Beschleunigern mit hohem Strahlstrom. Um zu den im Idealfall erreichbaren Parametern der supraleitenden Strukturen vorzustoßen, ist es erforderlich die derzeitigen Begrenzungen wie Feldemission, thermischen Zusammenbruch (Quench) und die Güte des Resonators, die Aufschluss über die ohmschen Verluste in Abhängigkeit von der elektrischen Beschleunigungsfeldstärke gibt, zu verstehen. Obwohl die begrenzenden Mechanismen selbst im Großen und Ganzen verstanden sind, sind die Ursachen für den Quench oft unklar.

Um die Quenchpositionen der Beschleunigungsstrukturen zu bestimmen, wurde ein Messaufbau zur Ortung des zweiten Schalls im suprafluiden Helium, der beim Quench entsteht, im Kavitäten-Testfeld bei DESY installiert und Daten bei ca. 30 Beschleunigungsstrukturen genommen. Die Auffälligkeiten der Verteilung der Quenchorte wurden untersucht und es ergab sich, dass die gemessenen Positionen üblicherweise in der Region mit den höchsten magnetischen Oberflächenfeldern waren, jedoch nicht notwendigerweise am Äquator der Zellen.

Zur Untersuchung der Güte in Abhängigkeit von der Beschleunigungsfeldstärke wurden weitere Messdaten von Beschleunigungsstrukturen untersucht. Eine Analyse des Oberflächenwiderstandes von einzelnen Kavitäten ergab, dass ein aktuelles Oberflächenwiderstandsmodell für Niob die Messergebnisse nicht in allen Einzelheiten beschreiben kann, aber die Berücksichtigung eines weiteren Mechanismus zeigte erste vielversprechende Ergebnisse.

# Contents

<b>Introduction</b>	<b>1</b>
<b>1 Particle Acceleration</b>	<b>3</b>
1.1 History and modern particle accelerators . . . . .	3
1.1.1 European XFEL . . . . .	4
1.1.2 International Linear Collider . . . . .	5
1.2 Radio frequency acceleration . . . . .	6
1.3 Essentials of cavities and superconductivity . . . . .	8
1.3.1 Accelerating field . . . . .	9
1.3.2 Superconductivity . . . . .	11
1.3.3 Quality factor and surface resistance . . . . .	13
1.3.4 Power dissipation in an rf cavity . . . . .	18
1.4 Performance limitations . . . . .	20
1.4.1 Hydrogen Q-Disease . . . . .	20
1.4.2 Multipacting . . . . .	21
1.4.3 Field emission . . . . .	22
1.4.4 Thermal instabilities and thermal breakdown (Quench) . . . . .	23
<b>2 Cavity Production and Preparation</b>	<b>25</b>
2.1 Cavity Fabrication . . . . .	26
2.1.1 Niobium . . . . .	26
2.1.2 Assembly and Welding Procedure . . . . .	27
2.1.3 Cavities made of Large Grain Niobium . . . . .	27
2.2 Surface Treatments . . . . .	28
2.2.1 Buffered Chemical Polishing . . . . .	28
2.2.2 Electropolishing . . . . .	29
2.2.3 Centrifugal barrel polishing . . . . .	30
2.3 Cavity preparation . . . . .	30
<b>3 Cavity performance test</b>	<b>33</b>
3.1 Vertical rf measurement setup . . . . .	33
3.2 Vertical test . . . . .	35
3.3 Diagnostic tools . . . . .	38

3.3.1	Temperature mapping . . . . .	39
3.3.2	Quench localisation using second sound . . . . .	40
3.3.3	Optical surface inspection . . . . .	45
3.3.4	Defect Treatment . . . . .	47
<b>4</b>	<b>Results of quench localisation</b>	<b>49</b>
4.1	Data sample . . . . .	49
4.2	Quench distribution along the cavity axis . . . . .	51
4.2.1	Distribution within a cell . . . . .	54
4.2.2	Fields at thermal breakdown . . . . .	57
4.2.3	Thermal breakdown fields in each cell . . . . .	58
4.3	Angular distribution . . . . .	59
4.3.1	Investigation of the shape of the angular distribution . . . . .	60
4.3.2	Angular distribution per insert . . . . .	63
4.4	Correlations with surface inspection . . . . .	64
4.4.1	Cavity Z161 . . . . .	65
4.4.2	Cavity AC126 . . . . .	66
4.4.3	Equator weld overlap . . . . .	66
4.5	Summary . . . . .	67
<b>5</b>	<b>Quality factor analysis</b>	<b>69</b>
5.1	Data sample . . . . .	70
5.2	Average quality factors of cavities . . . . .	70
5.2.1	$Q_0$ dependence on surface treatments . . . . .	70
5.2.2	Large grain and fine grain material . . . . .	73
5.2.3	Influence of RRR on the quality factor . . . . .	74
5.3	Surface resistance model . . . . .	74
5.3.1	Fit parameters for 21 cavity tests . . . . .	77
5.3.2	Additional resistance contribution . . . . .	82
5.4	Summary . . . . .	86
<b>6</b>	<b>Conclusion and Outlook</b>	<b>87</b>
	<b>Abbreviations</b>	<b>89</b>
<b>A</b>	<b>Quench localisation</b>	<b>91</b>
A.1	Measurement Accuracy . . . . .	91
A.2	Installation Issues . . . . .	91
A.2.1	High Voltage . . . . .	91
A.2.2	Electronic Noise . . . . .	92
A.2.3	Helium Bath . . . . .	92
A.3	Oscillating Superleak Transducers . . . . .	92
A.4	Electronics . . . . .	95



<b>B Used Datasets</b>	<b>97</b>
B.1 Second Sound Data . . . . .	97
B.2 Quality Factor Data . . . . .	102
B.2.1 Data for Averaged Quality Factors . . . . .	103
B.2.2 Data for Surface Resistance Model . . . . .	105
<b>List of Figures</b>	<b>I</b>
<b>List of Tables</b>	<b>V</b>
<b>References</b>	<b>XVII</b>
<b>Acknowledgements</b>	<b>XIX</b>



# Introduction

Exciting discoveries in particle physics in the last decades were only possible with experiments at particle accelerators providing high energy particle beams and collisions. The developments of accelerator and detector technology allowed the discovery of the elementary particles quarks, leptons and gauge bosons, and particle structure and their interaction mechanisms.

The latest accelerator for elementary particle research is the Large Hadron Collider (LHC) at the European Organization for Nuclear Research (CERN), providing two oppositely circulating proton beams with beam energies up to 7 TeV per beam. Results obtained by the LHC, especially the new particle at about  $125 \text{ GeV}/c^2$  presented in 2012, which is most probably the Higgs boson. This requires a more detailed examination, which is difficult at the LHC as the analysis of the data already requires model assumptions. An  $e^+e^-$  collider will provide a better environment to study the discoveries at the LHC, since the initial state of electrons and positrons is precisely defined and they do not possess a substructure. There are several proposals for  $e^+e^-$  colliders, including synchrotrons which have to deal with high synchrotron radiation losses and a new technology to generate very high accelerating fields at a linear accelerator. The aforementioned machines are at the early planning stage. The most advanced accelerator project, the International Linear Collider (ILC), evolved from a similar accelerator project proposed in 2001 at Deutsches Elektronen-Synchrotron (DESY), the Superconducting Electron-Positron Linear Collider with an Integrated X-Ray Laser Laboratory (TESLA). Hence the ILC is also based on 1.3 GHz 9-cell TESLA type superconducting radio frequency cavities.

At DESY the Tesla Test Facility (TTF) was built as a proof of principle for the TESLA technology. It succeeded to show the ability to build whole accelerator modules and a test accelerator, which is since 2005 a user facility providing Free-Electron Laser (FEL) light for users: the Free-Electron Laser in Hamburg (FLASH). With FLASH serving as a proof of principle accelerator, the European X-Ray Free Electron Laser (European XFEL), is under construction since 2009 and will be set into operation approximately in 2015. The industrial state-of-the-art production and treatment of 800 cavities has just started and will provide information about the potential of industrial mass production.

Superconducting cavities made of niobium are the basis of many particle accelerators around the world. Their advantages compared to normal conducting resonators,

usually made of copper, are lower power losses. The surface resistances are several orders of magnitude lower, which allows much higher duty cycles and accelerating fields for standing wave operation. Although the operating temperature of a few Kelvin requires liquid helium as cryogen, and hence a power consuming cryo plant, the overall power consumption of SRF operation is lower compared to normal conducting rf.

The ILC cavity design accelerating field of 35 MV/m, and an operational accelerating field of 31.5 MV/m for the ILC were chosen as an ambitious goal in 2005, which is optimised in respect of cost efficiency. The cavity design value is exceeded on a regular basis at laboratories all around the world. In 2011, two cavities reached 45 MV/m in the performance test already. Nevertheless, the reliable mass production of cavities with accelerating gradients of this order is still a challenge.

The ohmic losses are caused by the surface resistance of the superconducting resonator, which is strongly dependent of the purity and hence material parameters of the used niobium. While this basic relation is mostly understood, the field dependence of the surface resistance, is still lacking a proper explanation.

For a better understanding of the quench mechanism, a setup to localise the thermal breakdown by detecting the second sound in superfluid helium has been set up during the course of this work. After commissioning, about 30 cavity tests using the quench localisation have been carried out with recent cavities at DESY and statistical features of the thermal breakdown have been analysed. The results provide information for the production of future cavities, as the ultimate goal is maximisation of the mean accelerating electric field to reduce the overall length and cost of an accelerator.

The minimisation of ohmic losses, thus the maximisation of the quality factor  $Q_0$  is required to keep the cost for the required cryoplant low. To investigate the current performance of cavities, the test results of some 50 recent cavities with state-of-the-art treatments have been examined in two ways. The first goal was to study the average  $Q_0$  performance at different accelerating fields, to make global observations on the overall performance for particle accelerators using the 1.3 GHz cavities. The trend of the quality factor with increasing accelerating field for individual cavities has been examined and compared with models describing the evolution of  $Q_0$ . As  $Q_0 \propto 1/R_s$  describes the surface resistance  $R_s$ , an analysis of different loss mechanisms and their contribution to the total power loss has been done.

The thesis is divided into six chapters. In the first chapter particle accelerators and the basic principles of particle acceleration using superconducting cavities are introduced. This is followed by a summary of cavity fabrication and treatment in the subsequent chapter. The cavity performance test methods and the application of diagnostics tools are explained in chapter 3. Chapter 4 shows the results obtained from localisation of the cavity thermal breakdown using the second sound method, followed by the discussion of the quality factors and the surface resistance of cavities from recent productions at DESY in chapter 5. Chapter 6 summarises and shows the impact of these results.

# CHAPTER 1

## Particle Acceleration

---

During the 20th century the knowledge about fundamental aspects of matter has evolved and expanded rapidly. This is substantially due to the development of particle accelerators and detectors. Using high momentum particles, for example electrons and protons, colliding or scattering with each other, allows to study fundamental forces which are at work at very small scales. In addition 'new' elementary particles have been discovered and larger accelerator facilities allowed to study the properties of these particles. It is also possible to collide ions with each other to create a quark gluon plasma, a state of matter as it is expected to exist shortly after the big bang. In addition, particle accelerators are used to generate synchrotron light to screen molecular samples or do materials science as for example at PETRA III at DESY [1].

### 1.1 History and modern particle accelerators

In the beginning electrostatic fields as in Van-de-Graaff accelerators have been used for acceleration of charged particles. These are limited by voltage breakdown at some 10 MV of electric potential, hence the particles cannot gain more energy than some 10 MeV. The voltage breakdown is caused by the electrostatic field ionising the air and thereby causing a current to flow. To overcome this threshold and to be able to deal with particles with a velocity close to the speed of light, the idea of using alternating fields in the rf regime was applied first by Wideroe in the late 1920s [2]. As the direction of the electric field alternates in the MHz to GHz regime, the time required to ionise the gas is too long compared to an rf cycle.

The next step was to use the rf accelerating section efficiently, hence multiple times, to keep the accelerator small and increase the beam energy as much as possible. This required circular accelerators, where two types have been developed: Cyclotrons [3] are the accelerator of choice for experiments which require 'slow' particles compared to the speed of light. A simple cyclotron consists of two 180° bending magnets and an alternating rf field for particle acceleration in-between. Since the particles gain energy, the bending radius of the particles increases with each turn. As the principle

of acceleration in a cyclotron is based on the assumption, that the energy gain of the particles is proportional to the velocity, their application is limited.

The so-called synchrotrons proposed independently by E. McMillan and V. Veksler [4] in the 1940s, allow to ramp up the magnetic field in the bending magnets to keep the beam at the same orbit during acceleration. It requires a pre-accelerated beam, usually provided by a linear accelerator, as the particle source cannot be placed in the synchrotron itself. In comparison to cyclotrons this allows particle acceleration up to velocities very close to the speed of light.

At CERN, the largest synchrotron ever, the LHC [5] is in operation since 2008. It is designed to collide two proton beams accelerated in opposite directions with up to 7 TeV energy per beam. One of the main physics goals of the LHC is the discovery of the Higgs boson, which describes the origin of mass in the standard model. A Higgs-like boson has been found recently [6, 7], which requires a more detailed examination.

Linear accelerators (linacs) came into focus of attention for acceleration of light particles like electrons and positrons, because particle energies in synchrotrons are limited by energy loss due to synchrotron radiation [8]. The Stanford Linear Accelerator Center (SLAC) was founded in 1962 and the two-miles normal-conducting accelerator was brought into service in 1966 [9]. It was later extended to the Stanford Linear Collider (SLC) [10] which collided electrons and positrons starting in 1989, and hence was the first large linear collider operating.

To avoid ohmic losses in normal conducting accelerators and to allow higher duty cycles, superconducting accelerators came into focus. Although smaller superconducting linear accelerators like the S-DALINAC [11] and CEBAF [12] have been built and operated earlier, a first real large scale linear collider project was the TESLA project [13] with a total length of about 30 km. Although TESLA has not been built, the superconducting technology (and spin-offs) which has been developed for the accelerator and tested in the Tesla Test Facility (TTF) at DESY are used for several accelerators. The test of the demonstrating linac at the TTF was very successful and the FEL became available for user experiments: Since 2005 the roughly 250 m long FLASH [14, 15] user facility reliably provides FEL radiation created by an electron beam.

While current x-ray FEL facilities like the Linac Coherent Light Source (LCLS) at Stanford [16] and the SPring-8 Angstrom Compact Free Electron Laser (SACLA) [17] use normal conducting accelerator technology, the idea to build a superconducting accelerator for electrons to achieve FEL radiation in the x-ray regime like proposed for TESLA is currently realised: The European XFEL.

### 1.1.1 European XFEL

The successful test and use of the TESLA technology in the FLASH accelerator facility gave the impulse to construct a larger accelerator with the same technology: The European XFEL [18] was proposed in 2007 and is currently under construction

at DESY. It consists of an accelerator with a total length of 2.1 km followed by 1.2 km of beam lines to generate and to transport the FEL light to the ten experiment stations. The European XFEL will provide x-ray pulses to a wavelength down to 0.1 nm and light pulse lengths of a few femtoseconds. These parameters are of importance, as it is possible to study the movement of atoms or molecules during reactions, for example.

The design parameters of the European XFEL are listed in Table 1.1.

**Table 1.1:** Design parameters of the European XFEL accelerator [18]

beam energy	17.5 GeV
nominal accelerating field	23.6 MV/m
number of 1.3 GHz 9-cell cavities	800
effective acceleration length	$\approx 800$ m
operating temperature	2 K
radio frequency pulse length	1.4 ms
maximum number of $e^-$ bunches per pulse	3250
repetition rate	10 Hz
average beam current during pulse	5 mA

### 1.1.2 International Linear Collider

The LHC results, especially the recently discovered Higgs-like particle at  $125 \text{ GeV}/c^2$ , require a more detailed examination at a new collider. Protons have a complex parton structure and hence the initial state at the collision is not well defined at the LHC. For precise measurements with perfect initial conditions, an  $e^+ e^-$  linear collider is the accelerator of choice as elementary particles are used. This allows, for example, a precise determination of the branching ratios of the Higgs. The main Higgs production channel at the ILC is the so-called Higgs-strahlung: this leading order mechanism results in a  $Z$  and a Higgs boson after the collision of  $e^+ e^-$  at sufficiently high energies. In addition, in comparison to circular accelerators, energy losses arising from synchrotron radiation can be avoided. The ILC [19, 20] meets these requirements and is at the planning stage. It is designed to collide electrons with positrons at a center-of-mass energy of up to 500 GeV and a peak luminosity of  $2 \times 10^{34} \text{ cm}^{-2} \text{ s}^{-1}$ . An overview of the facility is shown in Fig. 1.1. The whole research complex will be about 31 km long with a large central campus, where the  $e^+ e^-$  interactions will take place underground in one of the two detectors [19]. Furthermore, the polarised electron source and the damping rings (see later) will be close to the campus area. To both sides each, a roughly 15 km long straight tunnel extends, containing the main accelerator, beam transport line and additional components e.g. for vacuum and electronics.

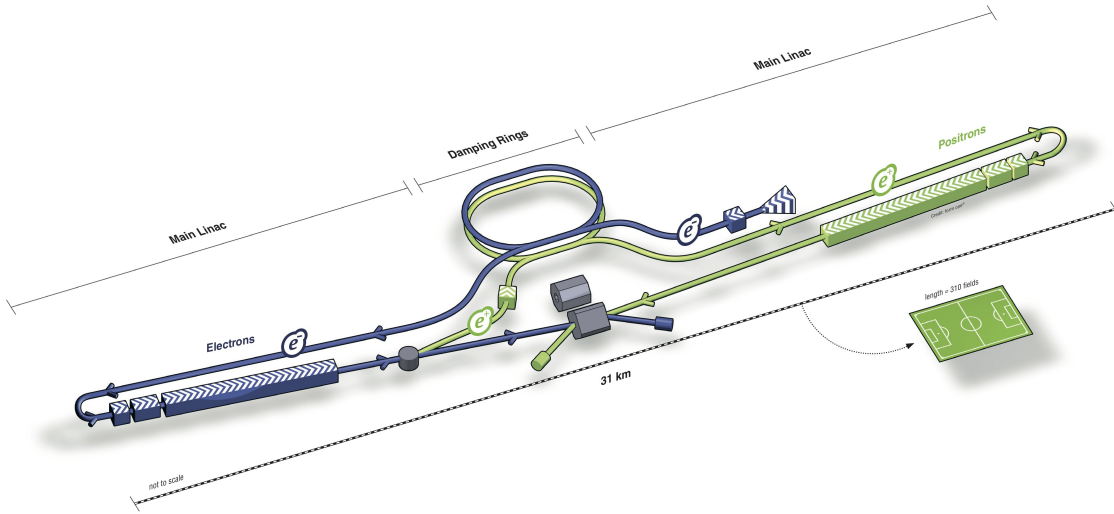


**Figure 1.1:** Schematic overview of the International Linear Collider [21].

**Table 1.2:** Design parameters of the ILC main linacs [19]

cms energy	500 GeV
nominal accelerating field	31.5 MV/m
total number of 1.3 GHz 9-cell cavities	16000
effective acceleration length	$\approx 16000$ m
operating temperature	2 K
radio frequency pulse length	1.6 ms
maximum number of bunches per pulse	5340
repetition rate	5 Hz
average beam current during pulse	9 mA

The accelerator consists of a polarised electron source and the positrons are produced by injecting the 150 GeV electron beam to an undulator. After this the generated photons hit a metal target and the positrons are generated via pair production. Before injecting the 5 GeV  $e^+$  and  $e^-$  beams into the main linacs, the beams circulate in a 3.2 km circumference damping ring to reduce the emittance of the beams required for higher luminosity. The technical parameters of the main linacs are given in Tab. 1.2. Most parameters of this project are very ambitious, especially it is very demanding to produce more than 16,000 superconducting cavities and maintaining the required average accelerating field.

## 1.2 Radio frequency acceleration

The acceleration of charged particles is possible with electric fields. As mentioned earlier, the use of electrostatic fields is very limited, as a voltage breakdown occurs



latest at an electric field of some 10 MV/m. This is due to the ionisation of gas particles causing sparks and discharges.

To overcome this threshold, alternating radio frequency (rf) fields are the method of choice for particle acceleration. A schematic rf particle accelerator is shown in Fig. 1.2. The alternating current is generated by a rf generator, which 'charges'

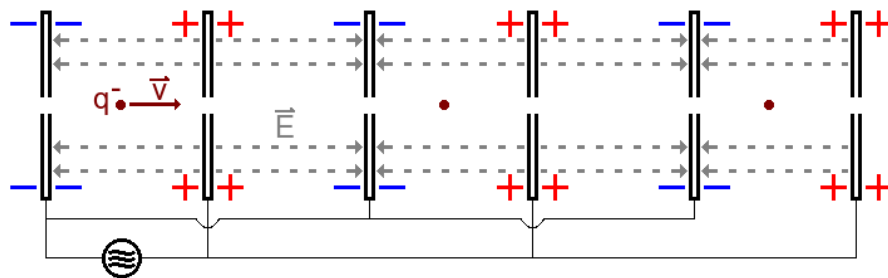


**Figure 1.2:** Schematic rf accelerator: The negatively charged particles  $q^-$  are accelerated by an alternating electromagnetic field, when they are injected in the right phase (as shown).

the plates and creates an electric field in between neighbouring plates. In the given example a particle bunch  $q^-$ , negatively charged, travels through the accelerating section. If the particles are injected with the right phase, into a so-called 'bucket', they experience an accelerating force by the electric field and thus gain energy. As this amount of energy is withdrawn from the rf system, the accelerating field has to be restored. Usually the demands for the bunch charge are too high and the recovery of the rf field requires several rf cycles (Technical Design Report for the European XFEL: 200 ns equals 260 rf cycles) before the next bunch can be injected into a bucket.

The use of high frequencies in the rf regime is of importance: even if the particles travel only at some percent of the speed of light - 10% for example - and assume an rf frequency of 100 MHz, the particle already travels 15 cm in half an rf period: low frequencies result in very long accelerators. As shown in the previous figure, the length of the drift tubes increases. This is the case for particles, where the energy gain still results in an increment of velocity. So the distance the particles travel during half a rf cycle increases. Particles travelling with a velocity close to the speed of light also gain additional energy, but this essentially causes a higher relativistic mass and the length of the drift tubes remains constant. For acceleration of particles close to the speed of light, usually a special type of resonators, so-called cavities are used, which will be described in the following section.

### 1.3 Essentials of cavities and superconductivity

A resonator is an oscillating system, which can be used to store energy if it is driven with the systems resonance frequency or close to it. A measure for this ability is the quality factor  $Q$ . It defines the number of oscillations until only  $1/e$  of the initial energy is left after leaving the oscillator without its driving force with  $e$  being Euler's number. If a system consists of  $N$  coupled resonators, it has  $N$  resonance frequencies.

A special class of resonators are cavities being used in physics to accumulate energy. A well-known example is the optical cavity within a laser system storing photons and causes the spontaneous emission of additional photons in the laser medium.

Cavities made of conducting metal (e.g. copper, niobium) are used for storing electromagnetic waves to provide electric fields for acceleration of charged particles. There are different types of cavities for different particles. As protons at rest for example require very high kinetic energies to reach a velocity close to the speed of light (to reach a relativistic  $\beta = 0.94$ , a kinetic energy of 1.81 GeV of the protons is required), for lower energies the cavities have to be adapted to the current velocity of the particles. Thus accelerators for protons and heavy ions consist of different types of cavities depending on the velocity of the particles, while for the 'light' electrons only an adaption at the very beginning of the accelerator is required.

Electrons are very light particles and if they experience an accelerating field of  $E_{\text{acc}} = 1 \text{ MV/m}$  over 1 m, which can be easily achieved with an electrostatic field, their velocity is already 94 % of the speed of light. The cavities in use for  $e^-$  or  $e^+$  basically require a design for a relativistic  $\beta = 1$ . The common shape of these cavities is elliptical for superconductors, as shown schematically in Fig. 1.3. Details of the shape vary, depending on the accelerator requirements.

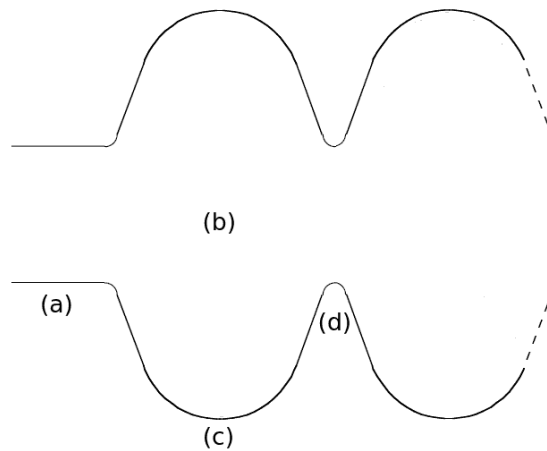


**Figure 1.3:** Schematic view of a part of a cavity with (a) cut-off tube, (b) cell, (c) equator and (d) iris.

Characterising the performance of those cavities is usually done with two parameters: the accelerating electric field  $E_{acc}$  and the unloaded quality factor  $Q_0$  (see section 1.3.3). Both will be introduced in the following sections and the use of superconducting radio frequency (SRF) will be motivated.

### 1.3.1 Accelerating field

A charged particle bunch (e.g. a bunch of electrons) enters the cavity and is exposed to an electromagnetic field and gains energy by the electric field component. Usually the phase velocity of the electromagnetic wave is similar to the velocity of the particle to allow the maximum energy gain. There are two possibilities to induce this electromagnetic field into the cavity. One can use travelling wave resonators, which indicates that the electromagnetic wave is fed into the cavity by a power coupler (see Fig. 1.4) at one side and travels through the resonator. The particles travel along the cavity at the same time and the energy is transferred from the wave to the particles. The advantage of this type of cavities is that high accelerating fields can be also achieved with copper cavities, but only for very short pulses.

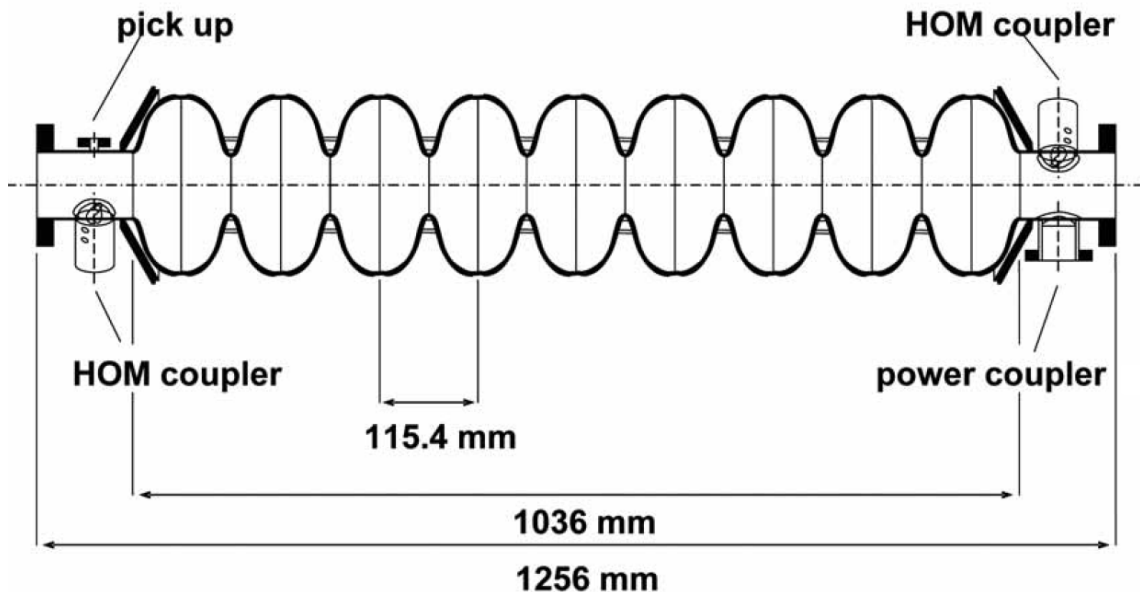


**Figure 1.4:** Overview of a 9-cell TESLA type cavity including rf power coupler, pickup for the rf signal and HOM dampers [18].

The second possibility is feeding a electromagnetic wave in the so-called  $TM_{010}$ -mode into the cavity which results in a standing wave. TM stands for transverse magnetic, this means the electric field component is excited in parallel to the flight direction of the particles, thus electric force is applied and the bunch gains energy. The magnetic field component is always perpendicular to the electric field and has a zero-crossing on beam axis, as shown schematically in Fig. 1.5.

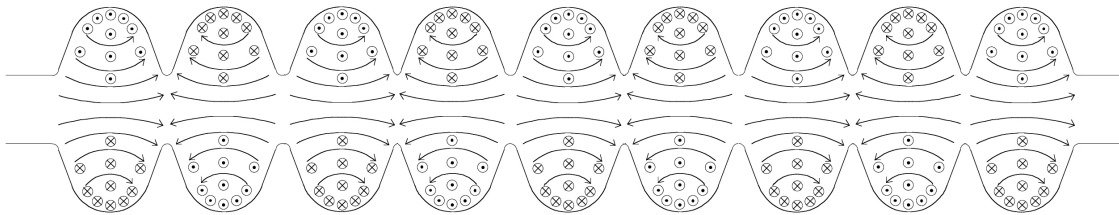


**Figure 1.5:** Overview of the electromagnetic field distribution in a 9-cell cavity in  $\pi$ -mode. The electric field is excited along the beam axis, while the magnetic field is perpendicular and induces currents in the niobium surface [23].

The particle bunch itself also excites eigenmodes of higher frequencies into the cavity due to the electromagnetic wake. These modes perturb the following particle bunches and eventually cause a total beam breakup [22]. The additional modes also generate heat losses and have to be rejected by special higher order mode (HOM) couplers, which are attached at the cut-off tube of each cavity, as shown in Fig. 1.4.

For a single cell resonator, there is only one passband mode, thus only rf signals with a frequency within the passband can feed the cavity. As a single cell cavity is a resonator with a certain frequency, a multi-cell cavity has to be treated as a coupled resonator and the number of cells lead to the number of available passband modes (eigenfrequencies). For a 9-cell cavity the nomenclature of the passband modes yields  $x/9\pi$  with  $x/9$  referring to the phase advance of the standing wave between neighbouring cells. These modes can be excited by feeding rf power with the appropriate frequency, but for acceleration, only the  $9/9\pi$ - or just  $\pi$ -mode is of practical use. The field amplitudes in a 9-cell cavity for the corresponding passband modes is given in Fig. 1.6.

The average accelerating field  $E_{acc}$  for a particle with a velocity close to the speed of light  $c$  in a rf cavity can be calculated using  $E(z)$  (electric field along beam axis),  $l$  (active length of cavity) and  $\omega = 2\pi f$  with  $f$  as rf frequency, when the electric field amplitude is at its maximum ( $E_{peak}$ ) during an rf cycle:

$$E_{acc} = \frac{1}{l} \int_{-l/2}^{l/2} E(z) \cos \frac{\omega z}{c} dz \quad (1.1)$$

The highest accelerating field for a 9-cell cavity has been achieved recently at DESY with roughly 45 MV/m [24]. Actual cavities reach accelerating fields above 25 MV/m reliably [24–26] being sufficient for the European XFEL and most of them even meet the specifications of the ILC as stated before.

The magnetic field component of the rf field has been neglected up to now, but is also of importance: The surface magnetic field induces a surface current causing resistance and heat. As shown in Fig. 1.5, the peak surface magnetic field  $B_{peak}$  is reached in the equator area, when the amplitude of the electric field is also at its

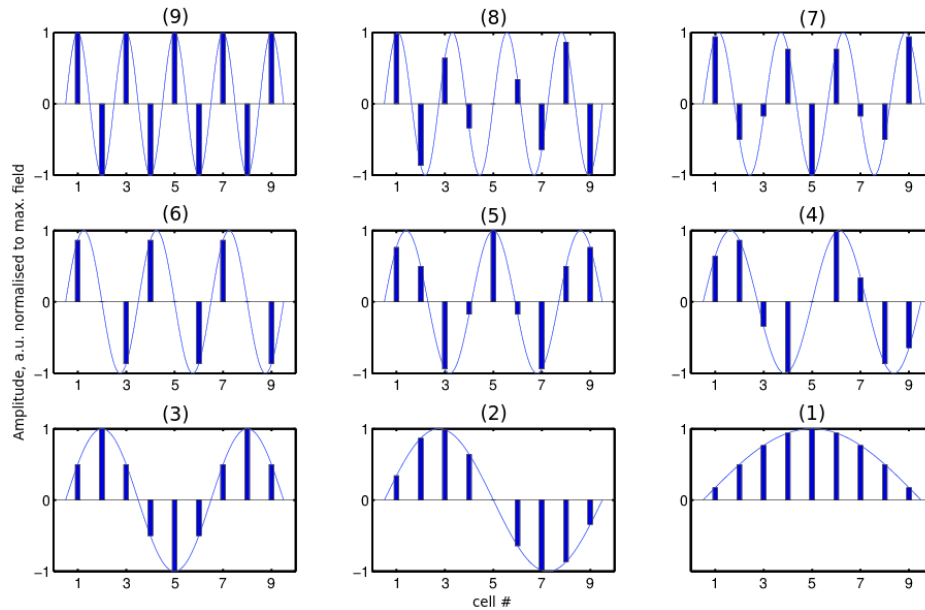


**Figure 1.6:** Field amplitudes in a 9-cell cavity depending on the mode excited. The number (x) above each plot indicates the passband mode  $x/9-\pi$ .

maximum  $E_{\text{peak}}$ . The accelerating field  $E_{\text{acc}}$  is the electric field experienced by the particle bunch. Both accelerating electric and peak surface magnetic field are linked via  $B_{\text{peak}} = c_f E_{\text{acc}}$ , so the minimisation of the conversion factor  $c_f = B_{\text{peak}}/E_{\text{acc}}$  is beneficial for the heat loss [27]. An important point to achieve a good accelerating field is 'field flatness'. In the ideal case this means that all cells of a multi-cell cavity are tuned on the same frequency, resulting in the best acceptance of rf power of the cavity and lowest measurement errors. More details about tuning can be found in section 2.3. The measurement and the uncertainties are described in chapter 3.

### 1.3.2 Superconductivity

Superconductivity has first been observed by Kamerlingh Onnes in 1911: the phenomenon of vanishing electrical direct current (dc) resistance at low temperatures. The repulsion of an applied magnetic field out of a slab of material in the superconducting phase is known as Meissner-Ochsenfeld effect. The main obstacle for reaching superconductivity is the need of very low temperatures. Below the so-called critical temperature  $T_c$ , certain materials show superconductivity. For niobium, the most common material used for superconducting cavities,  $T_c$  equals 9.2 K, if no magnetic field is applied (see Fig. 1.7).

A microscopic description of superconductivity has been developed by Bardeen, Cooper and Shrieffer (BCS theory) [28]. Below the critical temperature, the conducting electrons can form electron pairs ('Cooper pairs'). This is due to a potential

generated by a wake induced in the atomic lattice by the conducting electrons, which results in attraction of a second electron. Cooper pairs are bound states of lower energy compared to the sum of the individual electrons and flow without scattering on the material lattice, thus with zero resistance. For  $T \rightarrow 0$ , all electrons are paired.

For the description of superconductivity, two material parameters are of interest: The London penetration depth  $\lambda$  is a measure how deep the magnetic field penetrates a superconductor, and the Pippard coherence length  $\xi$  is the distance between the cooper paired electrons. The Ginzburg-Landau parameter  $\kappa$  is defined as

$$\kappa = \frac{\lambda}{\xi} \tag{1.2}$$

and describes the properties of superconducting materials. In fact, there are two types of superconductors, which can be characterised using  $\kappa$  of equation 1.2:

A type I superconductor repels the external magnetic field until a critical magnetic field  $B_c$  is reached. If  $B > B_c$ , the field fully penetrates the superconductor and superconductivity breaks down. This is the case for  $\kappa < \frac{1}{\sqrt{2}}$ , meaning that the coherence length is considerably larger than the penetration depth of the magnetic field.

For type II superconductors, the magnetic field is fully repelled up to a value  $B_{c1}$ . Above this threshold, an increasing amount of quantised magnetic fluxons with magnetic flux  $\Phi_0 = \frac{h}{2e}$  enter the material and generate tiny normal conducting locations (with  $h$  being the Planck constant,  $e$  the elementary charge). As long as the superconducting current flows on a superconducting path avoiding the normal conducting locations, superconductivity is not affected. At the thermodynamic critical field  $B_c$ , the fluxons block any superconducting path through the material, the transition to normal conducting material is completed, although superconductivity can remain locally until the upper critical field  $B_{c2}$

The achievable critical magnetic fields  $B_{ci}$  depend on the temperature, especially  $T_c$

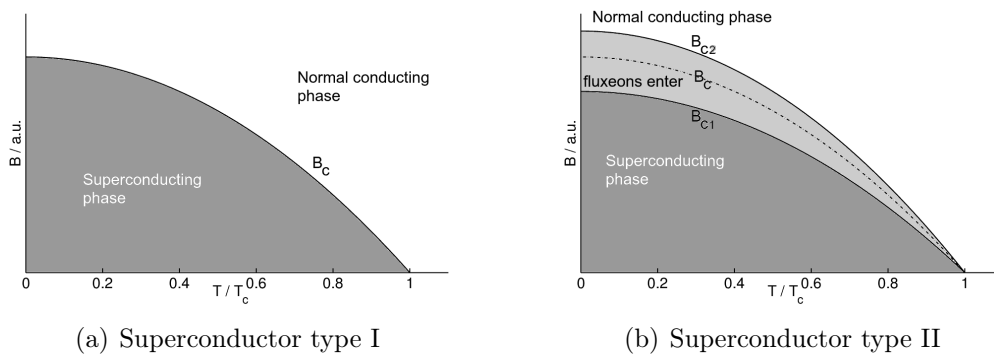


**Figure 1.7:** Phase diagram for superconductors of type I and II.

as shown in Fig. 1.7, with  $B_{ci0} = B_{ci}(T = 0)$ :

$$B_{ci}(T) = B_{ci0} \left( 1 - \left( \frac{T}{T_c} \right)^2 \right) \quad (1.3)$$

An example for a metal being type I superconductor is lead with  $\kappa \approx 0.45$  and  $B_c(T = 0) \approx 80$  mT. Niobium, which is used up to now for superconducting cavities is a type II superconductor with  $\kappa \approx 1$ . The thermodynamic critical magnetic dc field is  $B_c = 190$  mT at a temperature of  $T = 2$  K. For the rf case it can exceed  $B_c$  by about 20 % [22] due to the very short period ( $< 1$  ns) where the magnetic field is higher than  $B_c$ , the transition from superconductivity to normal conductivity cannot be completed - this effect is called 'superheating'.

### 1.3.3 Quality factor and surface resistance

The quality factor  $Q_0$  of an oscillator is a measure for the damping due to energy loss during the oscillation, and can be obtained by dividing the resonant frequency  $\omega$  by the frequency bandwidth  $\Delta\omega$ , see (1.4). For superconducting cavities with a frequency of 1.3 GHz this type of measuring the quality factor is of no use, since  $Q_0 \approx 10^{10}$  which results in  $\Delta\omega < 1$  Hz and is very difficult to measure.

For rf cavities the unloaded quality factor  $Q_0$ , which only takes the power dissipation in the cavity into account, can be calculated by acquiring the stored energy  $U$  by integration of the magnetic field in the cavity volume and the dissipated power  $P_{\text{diss}}$  by integrating the losses due to the surface resistance  $R_s(H)$  depending on the surface magnetic field  $H$  over the inner cavity surface (with  $\mu_0$  as vacuum permeability,  $dV$  as infinitesimal volume element within the cavity and  $ds$  as infinitesimal area element along the inner cavity surface):

$$Q_0 = \frac{\omega}{\Delta\omega} = \frac{\omega U}{P_{\text{diss}}} = \frac{\omega \mu_0 \int_V |H|^2 dV}{\int_s R_s(H) |H|^2 ds} = \frac{G}{R_s}. \quad (1.4)$$

Note that the last equal sign and the use of the geometry constant  $G$  as a constant is only valid by assuming  $R_s(H) = \text{const.}$  [29]. The geometry constant  $G$  indicates the shape of the cavity, but is independent of the cavity size. It is determined by the distribution of the magnetic field component within the cavity, as stated before. A constant  $G$  will be assumed in all the following discussion, since no local surface resistance data is available, and as mentioned later, no complete explanation of the  $R_s(H)$  dependence has been found so far.

While for normal conducting copper cavities in elliptical shape  $Q_0$  is in the order of some 1000s to 10000s due to their resistance in the order of m $\Omega$ ,  $Q_0$  for superconducting elliptical cavities is usually larger than  $10^{10}$  at  $T = 2$  K.

Using (1.16) and taking the specified accelerating fields for the European XFEL (23.6 MV/m) and ILC (31.5 MV/m) and  $Q_0 = 10^{10}$ , this results in continuous heat

dissipation of  $P_{\text{diss}}(23.6 \text{ MV/m}) = 58.3 \text{ W}$  and  $P_{\text{diss}}(31.5 \text{ MV/m}) = 103.8 \text{ W}$  respectively. These numbers show why these machines will be operated in pulsed rf mode and not in continuous wave operation, since each Watt of heat dissipation requires  $\approx 500 \text{ W}$  of wall plug power (1.17).

The quality factor and the surface resistance of the superconducting niobium respectively, depends on several material parameters. These are the rf frequency  $\omega$ , surface temperature  $T$ , the superconducting energy gap  $\Delta$  due to the lower bound states of electrons, and the coherence length  $\xi$  and penetration depth  $\lambda$  explained earlier. The BCS resistance yields in approximation for  $T < T_c/2$  and usual rf cavity frequencies in the GHz-regime [22]:

$$R_{\text{BCS}} = A \frac{\omega^2}{T} \exp\left(-\frac{\Delta}{k_B T}\right). \quad (1.5)$$

The parameter  $A$  includes material parameters, especially those mentioned above ( $\Delta$ ,  $\xi$  and  $\lambda$ ) and  $k_B$  is the Boltzmann constant. If the rf field is increased, the heat generated due to the Cooper pairs increases the surface temperature and the BCS resistance.

A measure for the purity of metals, in this case the purity of the niobium, is the residual resistivity ratio RRR. It is defined as the ratio of the resistance at room temperature (295 K) and at 4.2 K in the normal conducting state:

$$\text{RRR} = \frac{R(295 \text{ K})}{R(4.2 \text{ K})} \quad (1.6)$$

For niobium to be used for cavity production, the aim is  $\text{RRR} > 300$  to obtain higher thermal conductivity. It has been found for higher RRR, that the BCS resistance increases slightly [30].

Impurities, grain boundaries and thus trapped magnetic flux also contribute to the surface resistance as a constant value  $R_{\text{res}}$ , so the slight increase of  $R_{\text{BCS}}$  is acceptable: the better thermal conductivity allows higher rf fields before thermal breakdown [22].

If a constant magnetic field is applied to a superconducting cavity during cooldown from room temperature to the superconducting phase, the magnetic flux could freeze out in the bulk material which leads to higher surface resistances and higher ohmic losses, when a rf field is applied. A formula empirically found for cavities in the GHz region in [31] yields

$$R_H = \frac{H_{\text{dc}}}{H_c(0)} R^* \frac{1}{1 - (T/T_c)^2} \quad (1.7)$$

with  $H_{\text{dc}}$  as the applied magnetic field,  $H_c(0) = 198 \text{ mT}$  the thermodynamic critical field at  $T = 0$ ,  $R^* = \frac{R_{\text{NL}}}{\gamma}$  with  $R_{\text{NL}} \approx 2 \text{ m}\Omega$  as rf surface resistance of niobium at room temperature and  $\gamma = 1$  as fit parameter for frequency dependence.  $T_c = 9.2 \text{ K}$  is the critical temperature of niobium. Assume the earth magnetic field



to be  $H_{\text{dc}} = 40 \mu\text{T}$ , with (1.7) this leads to  $R_H = 424 \text{ n}\Omega$  in addition to other surface resistance components which are in the order of  $10 \text{ n}\Omega$ . Neglecting the  $10 \text{ n}\Omega$  with equation 1.4 this leads to a limitation to  $Q_0 = 6 \times 10^8$  which is more than one order of magnitude lower compared to the specifications for current accelerators.

This simple picture of the surface resistance  $R_s = R_{\text{BCS}} + R_{\text{res}}$  has been found to be incomplete [32]. The observation implies that contributions of other resistance components depending on the surface magnetic field and the electric field exist. Several explanations as in [33–36] have been published, but a generally valid picture is still missing. Some aspects and the most recent surface resistance model are discussed below.

### Thermal feedback model

The increase of the inner surface temperature can be compensated as long as the heat can be conducted away through the niobium into the surrounding helium bath (cf. chapter 3). If the amount of generated heat on the inner surface cannot be conducted away, the temperature of the inner cavity surface increases and as a consequence the surface resistance increases which eventually leads to thermal breakdown. This effect is known as thermal feedback. For example a model developed in Wuppertal [37] calculates the inner surface temperature of the niobium numerically. It includes the thermal conductivity within the niobium and the Kapitza resistance [38] at the transition between niobium and liquid helium, a measure for the thermal conductivity between these two materials. As the helium bath temperature at cavity tests is usually actively controlled and kept constant, it is assumed as constant. Numerical calculations of this effect have been carried out in e.g. [39], and as has been shown in [36], this model usually strongly underestimates the reduction of the  $Q_0$  at higher fields, the so-called Q-drop. In addition the rise of the quality factor at lowest fields cannot be explained with this model. Comparison of the model and an actual data sample of a very good cavity is shown in Fig. 1.8.

### Nonlinear BCS resistance

Another possibility to estimate the Q-drop at high fields is the non-linear BCS resistance model given in [36]. It includes the pair breaking effect of the superconducting current induced by the magnetic surface field - the power consumption for the breakup of electron pairs. Not included are effects from impurity scattering, and also the low field behaviour of measured quality factor curves are not taken into account.

### Surface resistance model by Weingarten

The most recent and also most complete model was published in 2011 by Weingarten [40], which gives a description of the overall behaviour of the surface resistance and thus the quality factor. A brief summary of this model is given here:

By analysing about 1300 datasets, it is stated that there are five contributions to the surface resistance  $R_s$ , with surface temperature  $T$ , frequency  $\omega$  and surface magnetic field  $H$  as measured parameters.

$$R_s(\omega, T, H) = R_{\text{res}2} + R_{\text{res}}(\omega) + R_{\text{s,BCS}}(\omega, T) + R_{\text{s,Q-inc}}(\omega, B) + R_{\text{s,fd}}(\omega, T, B) \quad (1.8)$$

The resistance  $R_{\text{res}2}$  includes surface defects which are normal conducting at any magnetic surface field and contribute to ohmic losses. The value obtained by the cumulated data yields  $R_{\text{res}2} = 3 \text{ n}\Omega$ .

The frequency dependent  $R_{\text{res}}(\omega)$  represents the contribution of additional normal conducting electrons due to normal conducting defects located within the rf penetration depth.

$R_{\text{s,BCS}}(\omega, T)$  is the BCS resistance as introduced in (1.5).

A description for the decrease of the surface resistance at low magnetic fields of some mT is given by:

$$R_{\text{s,Q-inc}}(\omega, B) \approx \frac{2\omega L \mu_0^2}{\pi B^2} \quad (1.9)$$

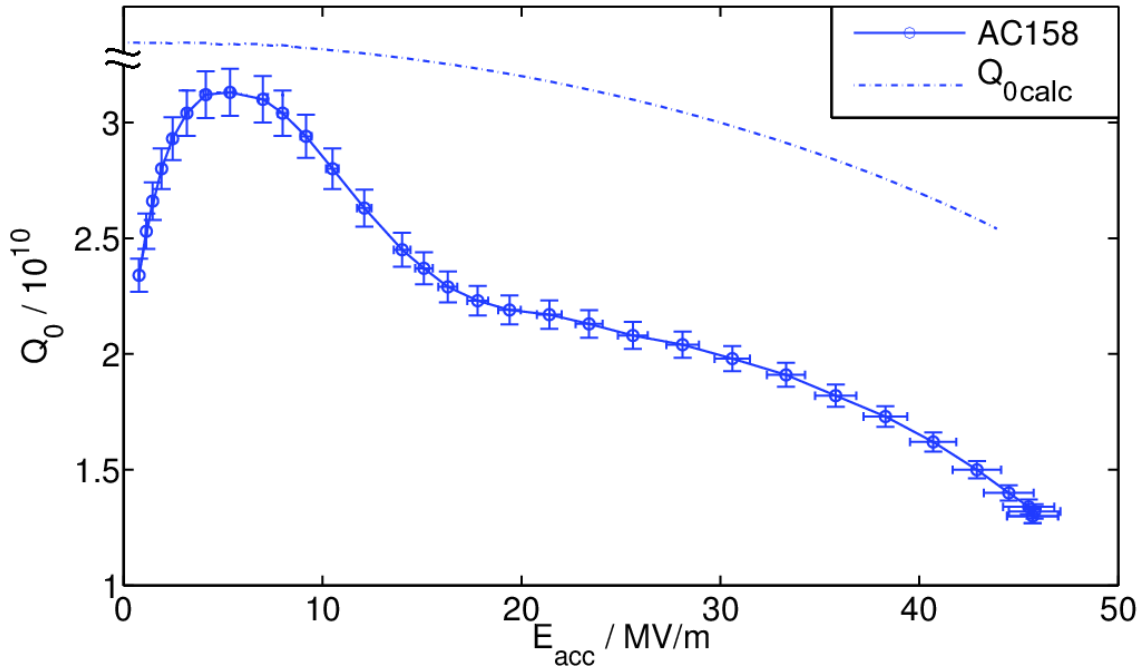


**Figure 1.8:** Measurement of the quality factor  $Q_0$  as a function of the accelerating field  $E_{\text{acc}}$  for cavity AC158. The cavity has an EP surface and reaches a maximum field of  $E_{\text{acc}} = 45 \text{ MV/m}$  with electropolished surface. The dashed line indicates the evolution of  $Q_0$  using a thermal feedback model calculation for the BCS resistance.

While  $\mu_0$  is the vacuum permeability,  $L$  is the latent heat per square meter independent on the magnetic field amplitude. The latent heat is dissipated twice per rf cycle due to a phase transition of first order in the NbO/Nb composite layer on top of the niobium bulk. Using the full dataset,  $L = 1.6 \text{ pJ/m}^2$ .

The explanation for the high field behaviour is given with the resistance contribution

$$R_{s,\text{fd}}(\omega, T, B) \approx [R_{\text{res1}} + R_{s,\text{fdt}}(\omega, T)] R_{s,\text{fdb}}(B, T) \quad (1.10)$$

with  $m$  including material parameters (penetration depth of current flow and the normal state conductivity at  $T = 4.5 \text{ K}$ )

$$R_{s,\text{fdt}}(\omega, T) = m\omega^2\Theta(T - T^*) \left( \frac{T - T^*}{T_c - T^*} \right)^\beta \quad (1.11)$$

and

$$R_{s,\text{fdb}}(B, T) = \frac{1}{\kappa^2} \left( \frac{(\frac{\kappa B}{B_c(T)})^2}{2} + \frac{(\frac{\kappa B}{B_c(T)})^4}{3} + \dots \right). \quad (1.12)$$

Niobium oxide (NbO) is a superconductor with  $T_c = 1.38 \text{ K}$  as transition temperature [41]. The proximity of bulk niobium keeps the NbO superconducting even above  $T_c(\text{NbO})$ . This effect is known as proximity effect [42]. A NbO/Nb composite within the penetration depth of the rf field does not allow the entry of magnetic flux at small rf fields, but also contributes to the surface resistance. As the field and the inner surface temperature rises, the NbO will form normal conducting regions of small size above a certain temperature  $T^*$ , the so-called percolation temperature, if the niobium allows a continuous superconducting path. Then these regions allow magnetic flux at already low fields, and the surface resistance increases.

$R_{\text{res1}}$  accounts for a field independent ohmic contribution by normal-conducting defects small enough to be penetrated by the superconducting current like grain boundaries, for example.

The parameters  $R_{s,\text{fdt}}(\omega, T)$  and  $R_{s,\text{fdb}}(B, T)$  are the result of a factorisation of  $R_{s,\text{fd}}$  into a field dependent (and slightly temperature dependent) factor, and a temperature dependent factor.

$R_{s,\text{fdb}}(B, T)$  describes the heat loss induced by the voltage induced by the superconducting current acting on the normal conducting NbO islands and explains the Q slope at medium accelerating fields.

The resistance  $R_{s,\text{fdt}}(\omega, T)$  models the contribution from the temperature increase of the inner cavity surface ('percolation term').

Note that the previously described model only takes variable losses induced by the magnetic surface field and the change of surface temperature into account besides the fixed contributions due to material parameters. Still, it is the most complete model describing the surface resistance at all surface magnetic fields up to the critical surface field. Recent cavity data acquired at DESY are analysed and compared to the previously described model in chapter 5.

### Interface tunnel exchange

The rf exposed surface is always covered with a thin layer of Nb<sub>2</sub>O<sub>5</sub> and NbO, and the oxidation preferentially takes place along the grain boundaries [43]. As explained earlier, NbO remains superconducting in proximity to bulk niobium. At low rf fields, the surface electric field penetrates the insulating and hence dielectric Nb<sub>2</sub>O<sub>5</sub> grain boundaries. If the electric field component increases, the rf field is raised, the electrons in the insulator may tunnel to the superconductor (and back) if it is energetically favourable to change from a localised state in the oxide to a state in the superconductor. As this occurs within an rf period, the magnitude of this loss is depending linearly on the rf frequency  $f$ . The exchange occurs in a superconductor, if the energy gain between the two states is larger than the energy gap  $\Delta$ . Thus the effect only occurs above a threshold field  $E^0$  and saturates at higher fields. This effect is known as the interface tunnel exchange (ITE) [44] and the loss can be calculated with [45]

$$R_s^E(E_{\text{acc}}) = R_{\text{sat}}^E \frac{f}{400 \text{ MHz}} \left( e^{-k/(2E_{\text{acc}})} - e^{k/E^0} \right), E_{\text{peak}} \geq E^0. \quad (1.13)$$

The parameter  $k$  contains material parameters,  $R_{\text{sat}}^E$  is the electric surface at saturation, so all states participate in the exchange, the peak electric field  $E_{\text{peak}} = 2E_{\text{acc}}$ . More details about the ITE can be found in [45], which also contains a detailed analysis of SRF data at different frequencies, temperatures and ratios between peak electric and magnetic field. To allow comparison of results, the normalisation to 400 MHz of [45] has also been used. It is important to mention that this particular model describes a fraction of the entire resistance losses, as this is only one mechanism which might be at work. As will be also shown in chapter 5, the ITE is of relevance in the medium accelerating field range and saturates at higher fields.

#### 1.3.4 Power dissipation in an rf cavity

As mentioned earlier, the rf duty cycle for European XFEL and ILC is in the order of 1%, thus only 1% of the power calculated for continuous wave operation is dissipated during regular operation. This is of importance for following comparison of heat dissipation at normal and superconducting cavities and the discussion of the quality factor results in chapter 5.

In the following cavities made of copper and superconducting cavities made of niobium are discussed. Assume that both have the shape of a TESLA 1.3 GHz 9-cell cavity and continuous wave operation.

#### Normal Conductor

The application of a rf electromagnetic field induces an alternating current (ac) in a thin layer on the conducting surface. To describe the thickness of this layer, the

skin depth  $\delta$  [46], including the rf frequency  $f$ , the permeability constant  $\mu_0$  and the conductivity  $\sigma$ , is used:

$$\delta = \frac{1}{\sqrt{\pi f \mu_0 \sigma}} \quad (1.14)$$

For copper ( $\sigma = 59.1 \times 10^6 \frac{\text{A}}{\text{Vm}}$ ) [46] exposed to an rf field with  $f = 1.3 \text{ GHz}$ , the skin depth is  $\delta = 1.8 \mu\text{m}$ .

The surface resistance giving evidence for the dissipated heat is calculated as follows:

$$R_{s(\text{n.c.})} = \frac{1}{\sigma \delta} = 9.3 \text{ m}\Omega \quad (\text{Cu}) \quad (1.15)$$

The geometric shunt impedance of a TESLA cavity is  $\frac{R}{Q} = 1030 \Omega$  [47]. It is another size independent parameter of importance and is proportional to the number of cavity cells and depends on the mode of the electromagnetic wave (see section 1.3.1). Taking the shunt impedance, the geometric constant  $G = 271.5 \Omega$  and an active acceleration length of  $l = 1.038 \text{ m}$  at a field  $E_{\text{acc}}$  of only  $1 \text{ MV/m}$  leads to a heat dissipation of

$$P_{\text{diss}} = \frac{E_{\text{acc}}^2 l^2}{\frac{R}{Q} \frac{G}{R_s}} = 35.8 \text{ kW} \quad (1.16)$$

for a 9-cell cavity made of copper. Not only the generated heat has to be dissipated, but the 35.8 kW of power are not available to accelerate the particles.

## Superconductor

For dc, superconductors have no measurable electrical resistance. Nevertheless, for rf cavities the niobium is exposed to an rf field inducing alternating currents in the upper layer of the superconductor. As stated in section 1.3.2, the paired electrons do not scatter with the niobium lattice, but as they have a momentum, the oscillation due to the rf current generates energy loss. From the dissipated power the BCS resistance can be calculated, e.g. for TESLA shape cavities in the order of  $R_{\text{BCS}} \approx 10 \text{ n}\Omega$ , being explained in the previous section. In addition, there are other contributions to the surface resistance  $R_s$  like a residual resistance part  $R_{\text{res}}$  which takes impurities into account, and several field-dependent mechanisms which have been explained in section 1.3.3.

Compared with the normal conducting cavity of the previous section, a superconducting TESLA cavity made of niobium with a surface resistance of  $R_s = 15 \text{ n}\Omega$  only creates a heat load of  $P_{\text{diss}} = 57.8 \text{ mW}$  at a temperature  $T = 2 \text{ K}$ . Although a cryogenic environment has to be provided, the overall power required is smaller compared to the copper cavity. The efficiency of the helium liquefier at  $T = 2 \text{ K}$  reads

$$\eta = \eta_c(2 \text{ K}) \eta_t = 6.7 \times 10^{-3} \times 0.3 \approx 2 \times 10^{-3} \quad (1.17)$$

with  $\eta_c$  as Carnot efficiency and  $\eta_t \approx 0.3$  as technical efficiency [22] of the system. This results in a wall plug power requirement for cooling of the ohmic losses of

$$P_{\text{cool}} = \frac{P_{\text{diss}}}{\eta} \approx 29 \text{ W}, \quad (1.18)$$

which is three orders of magnitude less than the power required to compensate the heat loss in the copper cavity. Note that other heat loads like thermal radiation from the environment have not been taken into account for this calculation.

## 1.4 Performance limitations

For reaching the accelerating fields and the quality factors mentioned before, several performance-limiting mechanisms have been found (an overview is given in Fig. 1.9), which will be explained briefly on the following pages. Most of them were overcome nowadays. More details and further references can be found in [22, 32].

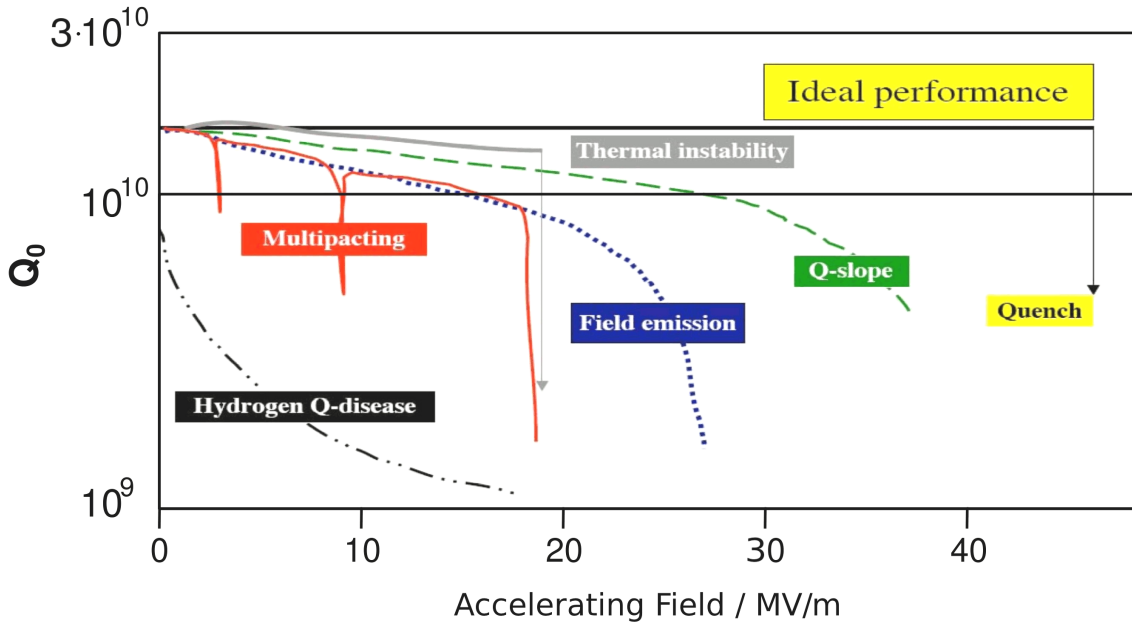


**Figure 1.9:** Signatures of performance limitations regarding the quality factor  $Q$  or the accelerating electric field  $E$  in the  $Q(E)$  curve [48].

### 1.4.1 Hydrogen Q-Disease

The degradation of the quality factor starting from  $E_{\text{acc}} \approx 0$  is due to hydrogen contamination of the niobium surface exposed to the rf field. Almost all production and treatment steps of niobium cavities (forming and welding, chemical treatments,

etc.) can cause contamination since the niobium lattice has a large affinity for hydrogen [49]. The creation of Nb-H leads to low quality factors  $Q_0 \approx 10^8$  already at very low fields for cavities with high RRR and high frequencies  $> 350$  MHz. Resistance losses induced by Nb-H are roughly scaling with the frequency  $f$  via  $f^2$  [49]. The losses induced by the contamination have to be attributed to the formation of niobium hydrides in the rf surface during cooldown at a temperature between 150-60 K. Above this temperature range, the concentration of hydrogen required in the surrounding gas is too high to create a critical amount of Nb-H (higher than 2 wt ppm), while below 60 K the diffusion of hydrogen is too slow to accumulate at hydride centres [22, 50].

Reducing the hydrogen pollution is possible by baking the cavities at 700-900 °C in a good vacuum  $p < 10^{-6}$  mbar to degas the bulk material.

Also, a rapid cool-down along the critical temperature range mentioned above reduces the probability to create hydrides. Unfortunately this is not possible for larger accelerators due to cryogenic power limitation. A cold cavity rf test as described in section 3.2 also includes the so-called Q-disease test: The cavity is kept for about 10 hrs in the critical temperature range of 80-120 K to 'trigger' possible contamination and to avoid Q-disease in a fully assembled accelerator module and eventually the accelerator.

## 1.4.2 Multipacting

Multipacting is another effect which can be observed in the Q vs. E curve in Fig. 1.9. It starts by one electron being emitted by a cosmic ray, photo emission or impacting field emission electron. The rf field induced in the cavity accelerates and deflects

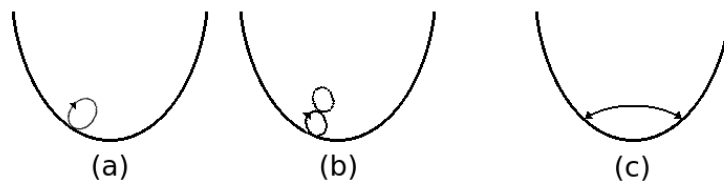


**Figure 1.10:** Schematic examples for multipacting (mp): (a) 1<sup>st</sup> order mp, (b) 2<sup>nd</sup> order mp, (c) two point mp.

the electron in a way that it may hit the cavity wall again as it can be seen in Fig. 1.10. If the secondary electron emission coefficient, an energy dependent value representing the chance of liberating other electrons, is large enough, an avalanche of electrons is liberated due to the impingement of the 'returning' electrons. The order of multipacting is the number of rf cycles until the liberated electrons hit the surface again. These free electrons absorb rf power as can be seen in the reduced quality factor and the field cannot be increased until this so-called multipacting

barrier is 'processed': The rf power is increased slightly, by allowing multipacting. After some time (usually in the order of minutes), the multipacting vanishes: no further electrons are emitted by impacts of others, and the quality factor switches back to the previous value before the onset of multipacting and the accelerating field increases as well.

For recent elliptical shaped cavities multipacting is no significant problem since the design of the shapes lead emitted electrons to the equator region where no acceleration takes place [51, 52].

### 1.4.3 Field emission

The main performance limiting process related to the high surface electric fields is field emission, which means the liberation of electrons from the metal surface by the electric field itself.

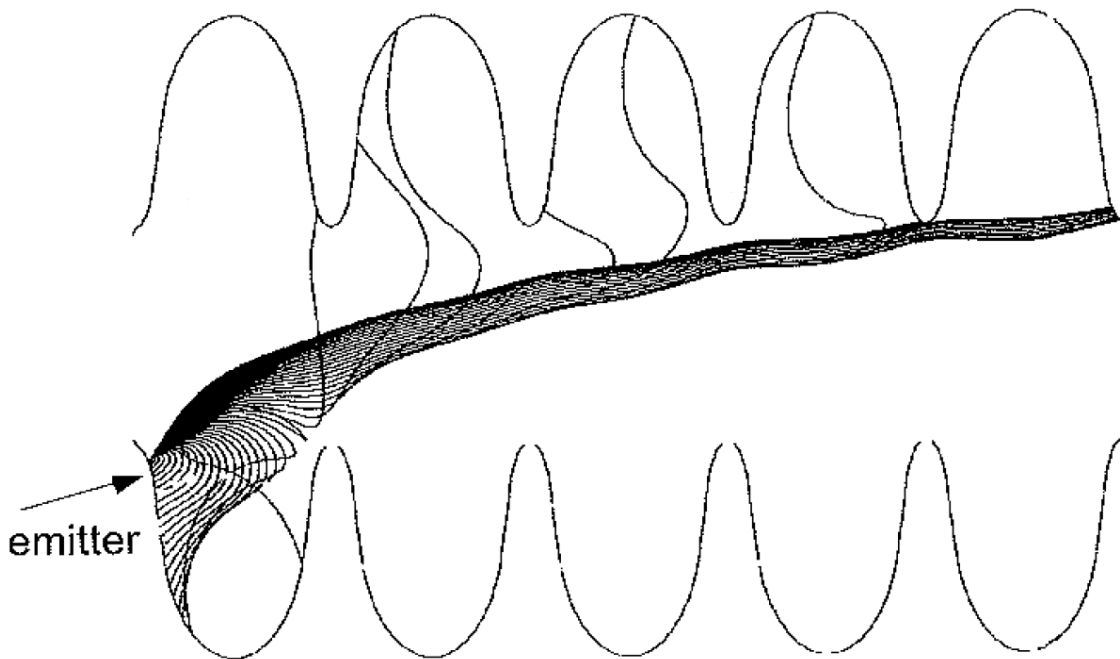


**Figure 1.11:** Example for calculated trajectories of electrons starting from a field emitter [22].

In general, the electrons are trapped in the metal. Application of a sufficiently high electric field leads to a decrease of the potential barrier inhibiting the release of electrons. Electrons can escape the material via tunnelling through the potential barrier and induce a dark current. The reduction of the quality factor due to energy gain of the electrons starting from about 20 MV/m in the example at Fig. 1.9 can be measured. The electrons may either hit the cavity or material like flanges or couplers causing radiation, which can be detected using x-ray sensors, and eventually



thermal breakdown (see next section) if the energy deposition of the electrons in the superconducting material is too high. Dark currents along the beam axis can cause problems in the accelerator itself. The highest electric surface fields in an elliptical cavity are close to the iris region like in Fig. 1.11 which shows an example for a simulated field emission process.

The onset of field emission varies on almost the full accelerating field range of cavities. In the early stages of TESLA shaped cavities, field emission was observed already below  $E_{\text{acc}} = 10 \text{ MV/m}$  because of dust or remnants from the surface treatment. Nowadays, field emission can be avoided most of the time due to better treatment and high pressure rinsing of the cavity surface [53] (see chapter 2) at least for fields up to about  $25 \text{ MV/m}$ . [25].

Other reasons for field emission, especially for high accelerating fields, can be surface irregularities leading to field enhancement and to the liberation of electrons. Those are still an important limitation [54].

#### 1.4.4 Thermal instabilities and thermal breakdown (Quench)

Assuming a 'defect' on the surface which may be an impurity in the niobium like an arbitrary particle or a flatness imperfection, mostly in the region of the equator where the magnetic surface field is at the maximum amplitude. Then it depends on the thermal conductivity between defect and bulk niobium, if a thermal instability or a thermal breakdown of superconductivity occurs.

A sharp drop of  $Q_0$  in a  $Q$  vs.  $E$  measurement may give evidence of a thermal instability, since the surface resistance and thus ohmic losses rise abruptly without quench. This effect occurs if the 'defect' is a particle or a niobium droplet created during the welding process, for example: thermally loosely connected to the niobium surface it causes ohmic losses without affecting the niobium surface temperature so that  $T_{\text{Nbsurf}} > T_c(H)$  resulting in thermal breakdown.

The breakdown of superconductivity is either a field induced quench by exceeding the critical surface magnetic field or due to joule heating which is related to the magnetic field  $\propto H^2$  [55]. So the accelerating field cannot be further increased.

If the thermal conductivity between defect and bulk niobium is very good, the surrounding niobium dissipates the generated heat of the defect, but its temperature increases. As long as  $T_{\text{Nb}} < T_c$ , the heat dissipation preserves the cavity from quench. If the temperature in the bulk niobium enclosing the defect exceeds  $T_c$ , superconductivity is lost, as a consequence the normal conducting niobium dissipates several joules of energy stored in the cavity and the cavity suffers thermal breakdown. Since the electromagnetic field stored in the cavity is dissipated as joule heating, the quench location cools down rapidly and enters superconductivity again. Thus the field may be established again in the cavity and the quench process starts again. A schematic of the heating by a defect is given in Fig. 1.12.

Although the origin of the quench is not fully understood, the accelerating field (the

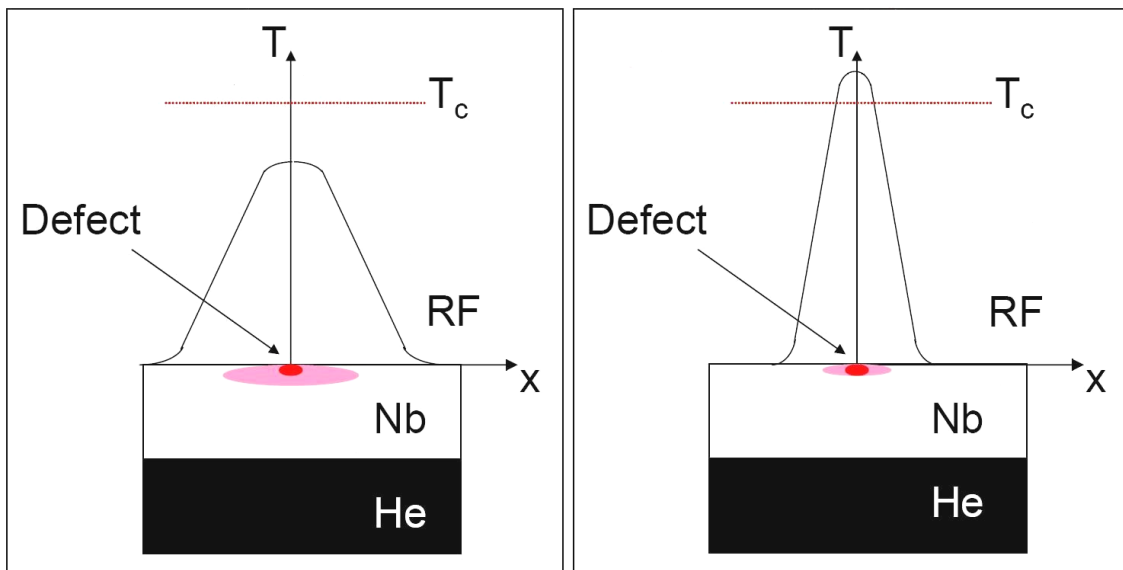


**Figure 1.12:** left: a defect generating joule heating of the surrounding niobium, but not exceeding  $T_c$ ; right: niobium exceeds  $T_c$  resulting in thermal breakdown [22].

quench level) of 1.3 GHz cavities exceeds  $E_{acc} = 30 \text{ MV/m}$  on a regular basis for electropolished surface treatment [26] (explanation of cavity production and surface treatments is given in the following chapter). Further examples and evaluation of quench locations in measurements done at DESY are given in chapter 4.

## CHAPTER 2

# Cavity Production and Preparation

---



**Figure 2.1:** Superconducting 9-cell 1.3 GHz XFEL-type cavity.

The 1.3 GHz 9-cell SRF cavities developed for TESLA are, with small changes due to different assembly preconditions, the accelerating structures for FLASH, the European XFEL and the International Linear Collider to accelerate electrons or their antiparticles, the positrons. In Fig. 2.1 a picture of the 1.3 GHz cavity is shown and the main cavity parameters are given in Table 2.1.

**Table 2.1:** Design parameters of the 1.3 GHz 9-cell cavities for the European XFEL [18]

fundamental frequency $f$	1300 MHz
nominal accelerating field $E_{\text{acc}}$	23.6 MV/m
Quality factor $Q_0$	$> 10^{10}$
active length $l$	1.038 m
iris diameter	70 mm
equator diameter	206.6 mm
$R/Q$	1030 $\Omega$
$E_{\text{peak}}/E_{\text{acc}}$	2.0
$B_{\text{peak}}/E_{\text{acc}}$	4.26 mT/MV/m

Focused on the production scheme for the cavities for the European XFEL, the steps of the production process for superconducting cavities of elliptical shape will be briefly discussed in section 2.1. More information about the manufacturing and

treatment of cavities in general can be found in [22, 32] or in particular for the 1.3 GHz 9-cell TESLA respectively XFEL cavities in [13, 18, 47, 56].

The preparation of the niobium sheets is followed by the deep-drawing of the half-cells and the cavity assembly and welding, as described in section 2.1. Thereafter the removal of the topmost surface layer damaged due to mechanical stress or the electron beam welding takes place by chemically polishing. This process is described in section 2.2.

The cavities have to be prepared for cold rf tests to figure out the success of the aforementioned steps by measuring the accelerating field, which is explained in the last section of this chapter, while the procedure of testing is described in detail in chapter 3.

## 2.1 Cavity Fabrication

### 2.1.1 Niobium

For the fabrication of superconducting cavities with lowest possible heat losses, it is important to use niobium of highest purity. This helps to avoid impurities which strongly increase the surface resistance and generate additional power dissipation. Best results are achieved by electron beam melting of the niobium ingot under vacuum. Impurities like gases are evaporated and can be eliminated by pumping [22], and the most important impurities including the technical specification [18] are given in the following:

While tantalum is usually the impurity with the highest concentration [22, 57] ( $\leq 500$  ppm (wt)), it does not substantially change the electronic properties. Gases like hydrogen ( $\leq 2$  ppm (wt), see section 1.4.1 and [50]), oxygen ( $\leq 10$  ppm (wt)) and nitrogen ( $\leq 10$  ppm (wt)) affect the niobium surface resistance and in the end the cryogenic losses.

The niobium is moulded into an ingot, a 'block' of purified niobium. With the measures mentioned it is possible to achieve  $RRR > 300$  as specified for the European XFEL [18]. Crystals form randomly within the niobium ingot, which are the basis for fine grain cavities. Niobium sheets are cut from the ingot, followed by a sequence of forging, rolling, polishing and annealing. The finished sheets are then delivered to DESY. Besides inspection of mechanical parameters, the quality control of the manufactured sheets regarding purity and RRR is done by creating an eddy-current in the niobium sheet. The signal radiated by the niobium sheet gives evidence for impurities [58]. To process the large amount of sheets required for 800 cavities for the European XFEL, the scanning device has been improved [59]. If the specifications are met [18] - for the European XFEL case - the niobium sheets are shipped to the cavity manufacturers.

The next steps are mechanical forming of the half-cells by deep-drawing the sheets with a set of dies, followed by machining the edges at the equator and iris side. The cleaning of the cavity parts starts with ultrasonic degreasing, followed by chemical

etching to remove the surface being in contact with the dies, and finished by ultra-pure water rinsing [56].

### 2.1.2 Assembly and Welding Procedure

The niobium cavities are assembled by electron beam welding (EBW) in vacuum. Two half-cells are connected at their iris with the first electron beam weld to dumbbells, followed by the attachment of the stiffening ring. Due to the heating during the welding process, the dumbbells may deform and consequently have to be brought to shape again. To determine the required amount of trimming on the equators and to ensure proper production of the half-cells and the dumbbells, the frequency of the pre-products is measured [60]. Therefore the parts are clamped between two contact plates equipped with a rf antenna each and the frequency is determined with a network analyser. After cleaning of all components, the end-cells with the cut-off tube, HOM couplers, power coupler and pickup feed-through and 8 dumbbells are aligned in the vacuum EBW machine to be joined to a full 9-cell cavity (see Fig. 1.4). There are two common techniques to obtain a fully penetrating and smooth welding seam on the inner surface by cycling a slightly defocused electron beam: A two pass weld with at 50 % beam power in the first and 100 % in the second pass, or immediately weld with 100 % beam power. A weld overlap of approximately  $30^\circ$  is obtained due to the rise and fade out of the welding beam, which will also be examined in chapter 4 as a possible source for thermal breakdown.

### 2.1.3 Cavities made of Large Grain Niobium

Almost all superconducting cavities at existing particle accelerators are made of fine grain niobium sheets, while the use of cavities made of large crystal (grain) niobium is still in the research phase. Some advantages are apparent: The fabrication of the niobium sheets is much simpler, as forging and rolling of the sheets is not necessary. For example, the DESY large grain cavities [24] 2.8 mm thick niobium sheets are directly cut from a niobium ingot with a large niobium grain in the center, intentionally produced for this purpose. Grain boundaries are suspected to be 'weak links' for the superconducting current - normal conducting spots causing additional resistance. The expectation on large grain cavities is a reduced residual resistance as the overall length of grain boundaries is much smaller than for fine grain material. A rough estimate is an assumption of a grain size of about 5 cm in diameter for large grain cavities. Fine grain material usually is fabricated with niobium grains with a diameter in the order of  $50 \mu\text{m}$  [18]. So the overall length of grain boundaries is about three orders of magnitude lower for large grain material. Evidence for this expectation has been found in the evaluation of the eleven large grain cavities tested at DESY by comparing the quality factor measurements at a helium bath temperature of 1.8 K, which accentuates  $R_{\text{res}}$ : The quality factor of large grain cavities is higher than for cavities made of fine grain material [61]. A detailed evaluation and

comparison of large grain test results regarding the quality factor is also done in chapter 5. Results in [62] also show that large grain material leaves much smoother surfaces with buffered chemical polishing (see next section), and electropolishing can be avoided.

Disadvantages of large grain material are, that industry is not yet capable to produce large grain niobium ingots on a large scale. In addition, the assembly of the cavity is more difficult: The shape deviations after deep drawing are strongly dependent on the orientation of the large niobium crystal [61], and the grain boundaries are pronounced with steps up to 0.5 mm in the large grain cavities at DESY [63].

## 2.2 Surface Treatments

Two ways of surface finishing are established for superconducting cavities provided for the European XFEL: electropolishing (EP) and buffered chemical polishing (BCP). Details of these treatments and of other treatments available are given in the following sections. In both EP and BCP 'XFEL'-processes flouric acid (HF) is required to remove the some nanometers thick  $\text{Nb}_2\text{O}_5$  surface. This layer is naturally present on the surface and created during the polishing process by reoxidation of the blank niobium surface with another acid. In a first step, the so-called bulk removal, a layer of more than 100  $\mu\text{m}$  is removed. As final treatment after further preparation steps (see section 2.3), a second chemical polishing takes place.

### 2.2.1 Buffered Chemical Polishing

BCP of niobium cavities at DESY is done with a mixture of three acids:

- flouric acid: HF (40%, 1 part in volume)
- nitric acid:  $\text{HNO}_3$  (65%, 1 part in volume)
- phosphoric acid:  $\text{H}_3\text{PO}_4$  (85%, 2 parts in volume)

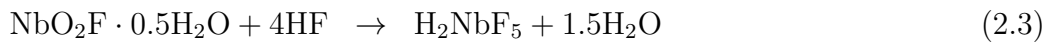
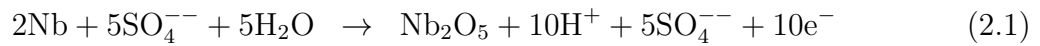
While HF removes the  $\text{Nb}_2\text{O}_5$  surface layer,  $\text{HNO}_3$  oxidises the Nb-surface again. Phosphoric acid is added as buffer acid, since the removal rate of a mixture of HF and  $\text{HNO}_3$  is about 30  $\mu\text{m}/\text{min}$  and the process behaves strongly exothermic [64]. With  $\text{H}_3\text{PO}_4$  and the cooling of the mixture below 15°C, the removal rate is about 1  $\mu\text{m}/\text{min}$ . The possible thermal runaway of the etching process and the insertion of hydrogen in the niobium are disadvantages of the BCP treatment. In addition it has been reported, that BCP surface cavities at DESY do not overcome a threshold of  $E_{\text{acc}} \approx 30\text{MV}/\text{m}$  [64, 65]. Nevertheless, there are few examples of BCP treated cavities in other laboratories exceeding this threshold (cf. [66]).

### 2.2.2 Electropolishing

The process of electropolishing [67, 68] has long been used for smoothing metal surfaces. It is also available for niobium cavities with the following acid mixture in use at DESY:

- flouric acid: HF (48%, 1 part in volume)
- sulphuric acid: H<sub>2</sub>SO<sub>4</sub> (96-98%, 9 parts in volume)

An applied voltage is required to run the (electro-)chemical processes, which proceed as follows [69, 70]:



A horizontal electropolishing apparatus for elliptical cavities with pulsed current has been first reported in [71]. The first continuous current machine was developed later [72], and became available at DESY in 2003 [73]. A schematic drawing of a horizontal EP apparatus is shown in Fig. 2.2.

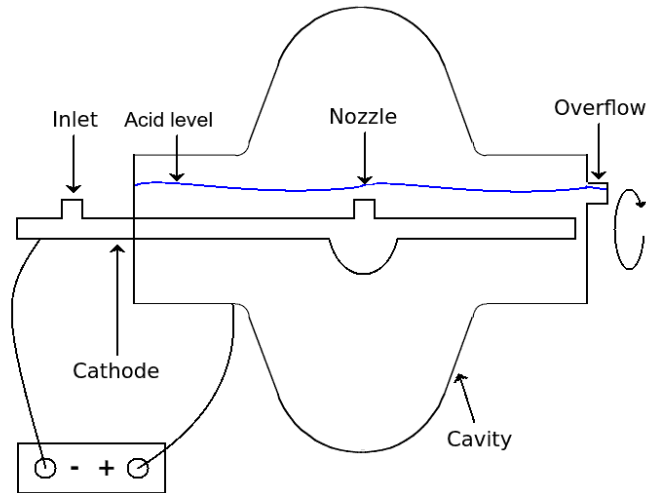


**Figure 2.2:** Schematic drawing of a horizontal electropolishing device with a single cell cavity. The cavity is in rotation to allow uniform surface removal.

The applied voltage gives control of the chemical reaction, so problems like the thermal runaway during BCP are avoided. In addition, the electric field concentrates on protrusions, and so these locations are flattened faster than the average removal rate, giving a smoother overall surface. As sulphuric acid is used in this process, some sulphur remnants stay on the cavity surface which have to be removed using ethanol rinsing (see section 2.3).

The general process of electropolishing is used in all labs working on 9-cell TESLA type cavities, with small variations. At Jefferson Lab a slightly different acid mixture is used for processing the ILC R&D cavities (HF:H<sub>2</sub>SO<sub>4</sub> 1:10) [74]. In addition, vertical electropolishing is another setup to electropolish cavities [75], which has several advantages like no sliding seals and electrical contacts, for example.

### 2.2.3 Centrifugal barrel polishing

The chemical treatments introduced before require the hazardous hydrofluoric acid and the smoothness of the surface after polishing depends slightly on the initial roughness. So a demand for treatments using less HF exists, but the procedure mentioned below is still in the development and improvement phase and therefore not in use for the series cavity production of the European XFEL. A replacement for the first heavy chemical treatment (cf. Fig. 2.3) is centrifugal barrel polishing (CBP). The cavity is filled with abrasive material and is rotated at high speeds. This procedure creates a smooth overall surface, because the whole surface is affected uniformly, while the chemical treatments introduced before show a non-uniform removal, depending on the surface structure. The CBP is followed by a short EP to remove remainders of the grinding material and an 800°C bake [76].

## 2.3 Cavity preparation

After assembly and welding of the cavity, the further treatments are (electro-) chemical polishing as described in section 2.2. The exterior of the cavity is also treated with a 20 µm BCP to remove the remainders from fabrication for best thermal conductivity between cavity and liquid helium. To clean the inner surface from particles and thereby suppress field emission, high pressure rinsing (HPR) with ultra pure water is performed additionally [32, 77]. Sulphur debris introduced by EP is non-removable by HPR and a source for field emission, so an additional ethanol rinsing is the treatment of choice [73]. Firing the cavity in a vacuum furnace at 800 °C removes hydrogen causing Q-disease as explained before in section 1.4.1 and also reduces mechanical stress on the material from mechanical treatment.

Hereafter the cavity is tuned to the frequency required by squeezing or stretching each cell, which will be done for the European XFEL cavities with automated tuning machines at the cavity manufacturers [78, 79]. The cavity usually is not perfectly tuned, a small frequency shift between the cells remains and the measurement of the accelerating field is misleading, since the real field in each cell is different from the measured cavity field. In addition, the accelerating  $\pi$ -mode is most sensitive on frequency errors in the end cells - an error in the order of 30 kHz already results in a field error of about 1% [80]. The lower the measured mode, the smaller the effect of frequency errors in the end-cells. Usually the field in the cavity is 'tilted' - the frequency error increases from one end of the cavity to the other because of



the measurement and tuning procedure. This results in a difference in field between both end-cells of about 10 %. Averaging yields an overall error of 5 % in accelerating field for a whole cavity [81]. The final electropolishing process changes the resonance frequency again: the material removal has to be considered in the tuning process by choosing the corresponding frequency.

After the final (electro-)chemical process, including additional HPR and ethanol rinsing if applicable, the helium vessel is welded on the cavity and all other parts for preparation of a performance test or module are assembled in a clean-room. Subsequently another 120 °C baking for 48 hrs has been proven to avoid Q-slope (see Fig. 1.9) [82]. An overview of the sequence of treatment steps applied for the European XFEL cavities is given in Fig. 2.3.

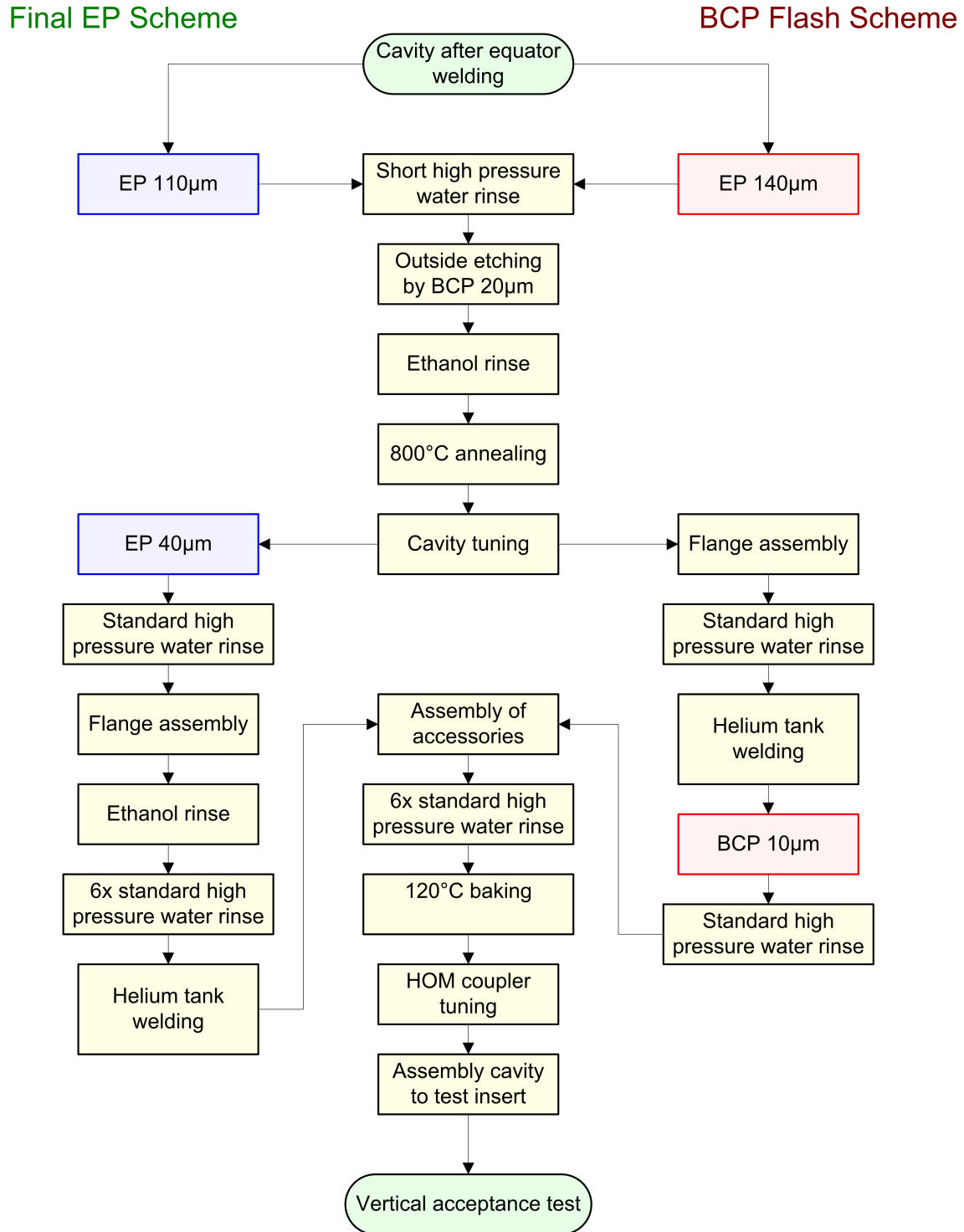


Figure 2.3: Cavity preparation schemes for the European XFEL cavities [83].

## CHAPTER 3

# Cavity performance test

---

After the assembly and preparation of the cavity, the next step is a performance test in a vertical helium bath cryostat to check for the maximum accelerating field, quality factor and possibly field emission. In addition, diagnostic tools to check for hot spots on the cavity surface due to ohmic heating or to find the location of thermal breakdown for example, can be applied. After a description of the test setup in section 3.1, the measurement procedure for accelerating field and quality factor is explained in section 3.2, followed by a description of the diagnostic tools applied at DESY in the subsequent section.

### 3.1 Vertical rf measurement setup

After preparation and assembly of all parts like HOM feedthroughs and coupler antenna in an ISO 4 cleanroom environment, the cavity is evacuated, leak checked and brought out of the cleanroom. To install the cavity into one of the vertical cryostats in the test area [84], the cavity itself has to be mounted into a special supporting frame, a so-called test insert. An overview of the cavity insert in the cryostat is shown schematically in Fig. 3.1. The insert provides a vacuum connection to keep the cavity pumped and the required rf cables and feedthroughs at the lid. Cryogenic diagnosis like temperature sensors and helium level sensor are also attached. If required, cavity diagnostic tools, described in detail in section 3.3 are mounted either at the cavity or the cavity insert. If all connections required for the cavity (rf cables, vacuum and diagnostics if applicable) are established, a final leak check is done before placing the insert into the vertical cryostat. After sealing the cryostat with the lid of the insert and mounting connections to the vacuum system at the cryostat, the cryostat is evacuated to test the leak-tightness of the cryostat to avoid the freeze out of foreign gases when the system is cooled down with liquid helium to 2 K. Subsequently, the cavity is cooled down to either 80-120 K and kept there for about 10 hrs to test for Q-disease after surface treatment (cf. section 1.4.1), or directly to 2 K.

### 3 Cavity performance test

---

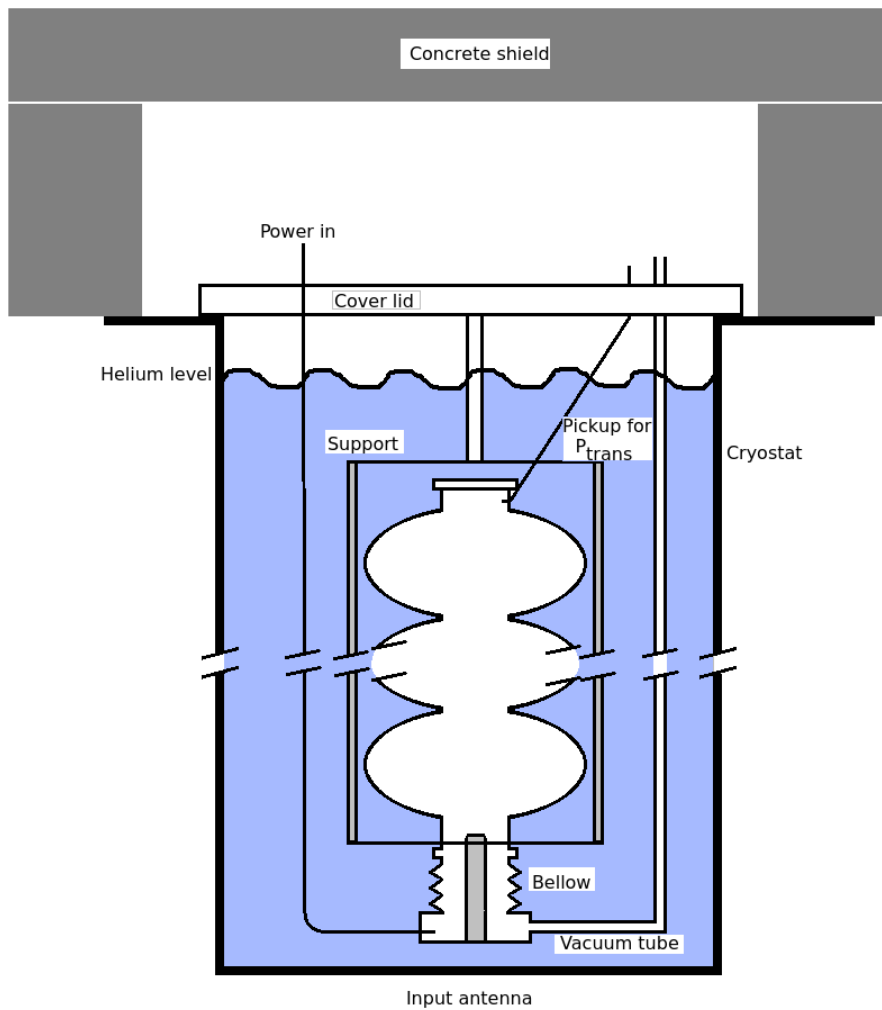


**Figure 3.1:** Schematic drawing of a vertical cryostat with required parts. The cavity itself is assembled in a supporting frame which is mounted at the cover lid which is inserted into the vertical cryostat. Power and vacuum connections are also provided as feedthroughs in the lid. Parts kept under vacuum in the cryostat are the cavity itself and the vacuum line. The cryostat is filled with liquid helium. The length of the cryostat including insert and the center cells of the cavity is cut for clarity.

The cryostat itself is shielded with two magnetic shields to avoid the freeze-out of the earth's magnetic field in the cavity (see also section 1.3.3): mu metal<sup>®</sup> at the outer wall of the cryostat, and cryoperm<sup>®</sup> at the inner part [85].

After filling the cryostat with LHe, the rf cabling including calibration of the rf equipment explained in the next section, radiation sensor and diagnostic equipment are established.

## 3.2 Vertical test

The parameters of interest for the cold cavity test are the quality factor  $Q_0$  and the accelerating field  $E_{acc}$ . For the vertical test, the maximum accelerating field and the related quality factor are of importance. These values determine if the cavity is accepted (acceptance test) for further assembly into an accelerator module and eventually installation into an accelerator. Limitations for the acceptable field are thermal breakdown, a radiation level that indicates too much field emission, or reaching the quality factor threshold. The increase of the accelerating field is done step by step, and additional data is taken to obtain the trend of the quality factor - the Q vs. E curve, as has been introduced earlier.

As there is no possibility to measure  $Q_0$  and  $E_{acc}$  directly, they have to be determined by recording the measurable powers in the rf circuit and the decay time of the cavity rf amplitude. These values allow to determine the power dissipation in the cavity wall resulting in the quality factor. The rf power available in the resonator gives evidence of the accelerating field. A simplified overview of the rf measurement setup is shown in Fig. 3.2.

A generator for the rf signal feeds a small amount of power into the continuous wave (cw) amplifier. As the resonance width of the passband frequencies of a superconducting cavity is very sharp, small changes in helium pressure already change the resonance frequency. So the reference generator has to be adjusted dynamically to the resonance frequency by a phase locked loop (PLL), as the cavity only allows power input at the passband frequencies. A fraction of power will be reflected at the cavity input  $P_{ref}$ , and another small amount of power  $P_{trans}$  has to be extracted for the PLL regulation. The PIN diode next to the rf generator toggles the rf power, which is required to determine the rf field decay time  $\tau_l$ . Together with the determination of the aforementioned powers, the quality factor can be calculated. Since a detailed reference is available in e.g. [22], only the most important steps for the calculation of  $Q_0$  and  $E_{acc}$  will be discussed here.

Using the measured powers, it is possible to calculate the ohmic losses, thus the power dissipated into the helium bath:

$$P_{diss} = P_{for} - P_{ref} - P_{trans} \quad (3.1)$$

If the rf power is switched off, the energy stored in the cavity reduces exponentially. Therefore the power loss at the power coupler  $P_{ref}$  decays with a decay time  $\tau_l$ ,

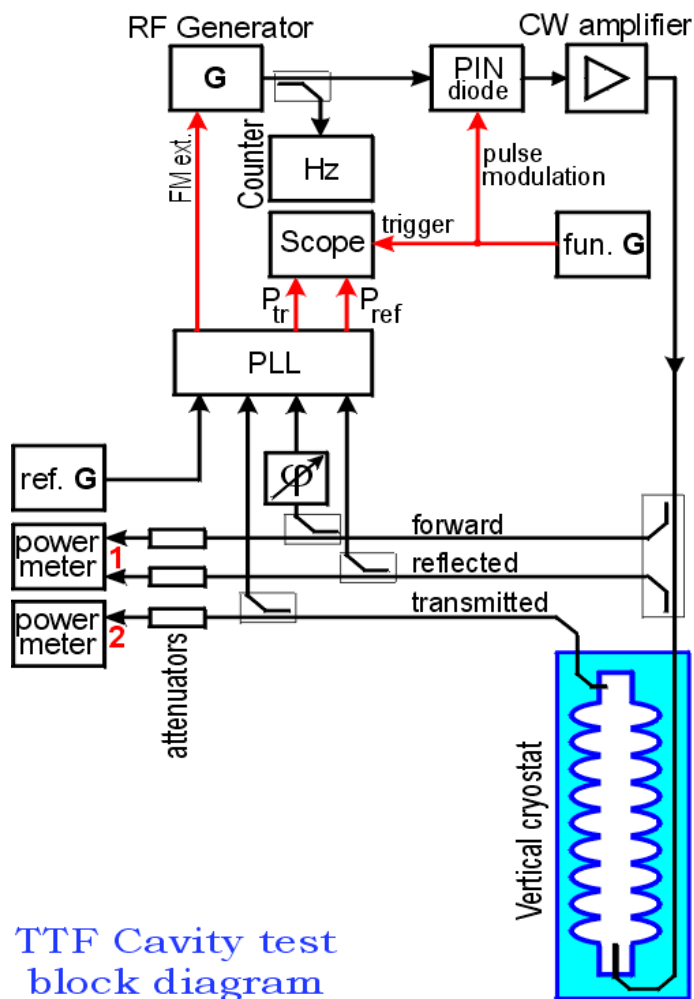


**Figure 3.2:** Simplified overview of the rf circuit required for vertical test: The amplified and modulated signal by the rf generator is fed into the cavity and the available powers are recorded [86].

which can be determined by fitting an exponential function to the reflected signal (see Fig. 3.3). This allows to determine the quality factor of the cavity, including the power losses in the power coupler, pickup and HOM antennas, the loaded quality factor  $Q_l$ :

$$\tau_l = \frac{Q_l}{\omega} \mapsto Q_l = \tau_l \omega \quad (3.2)$$

In Fig. 3.3, the reflected power signals - the 'reaction' of the cavity on a rectangular rf pulse is shown, depending on the matching of power coupler antenna and cavity. Right at rf power on, the cavity does not 'accept' any rf power, all power is reflected. The transient of the cavity starts, rf power is accepted and the reflected power reduces until it saturates. At rf power off, another peak  $P_e$  in the reflected power signal occurs, which accounts for the power returned from the cavity into the coupler antenna.

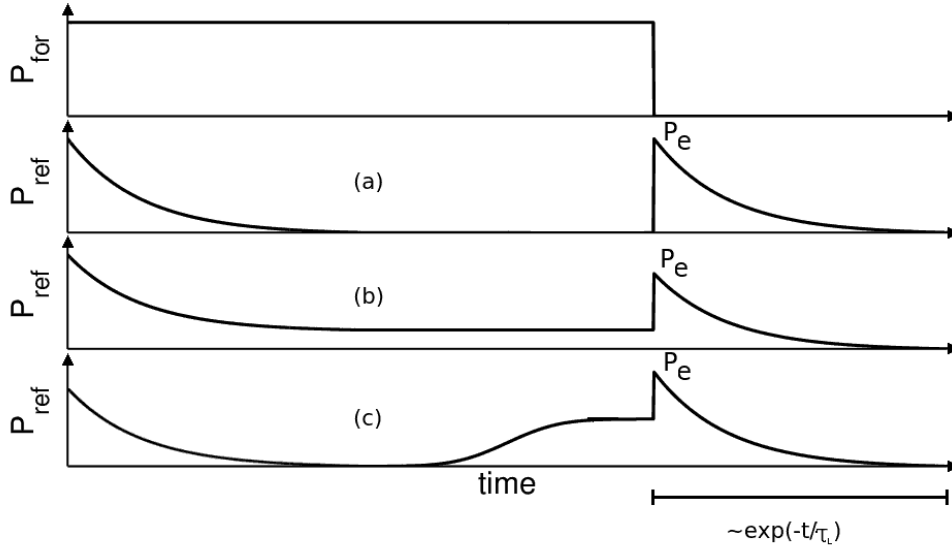


**Figure 3.3:** Power signals on the scope:  $P_{\text{for}}$  indicates the power of rectangular rf pulse applied on the cavity.  $\beta$  is the coupling factor. (a) is the reflected power for the coupling factor  $\beta = 1$  - the peaks at power on and off are equal in amplitude, (b) for  $\beta < 1$  - the switch off peak is lower than at power on, (c) for  $\beta > 1$  - switch off peak is higher than switch on.

The signals in Fig. 3.3 are of importance to obtain the unloaded  $Q_0$ , as the matching of power coupler antenna and cavity, the so-called coupling factor  $\beta$ , can be determined with the measured quantities introduced before:

$$\beta = \frac{1}{2\sqrt{\frac{P_{\text{for}}}{P_e} - 1}} \quad (3.3)$$

**Table 3.1:** Parameters and uncertainties for calculation of  $Q_0$  and  $E_{\text{acc}}$ , the power errors are 0.2 dB

parameter	sign	unit	relative uncertainty
frequency	$f_0$	Hz	<0.01%
decay time	$\tau$	s	3%
transmitted power	$P_{\text{trans}}$	W	4.6%
dissipated power	$P_{\text{diss}}$	W	8%
reflected power	$P_{\text{refl}}$	W	4.6%
forward power	$P_{\text{forw}}$	W	4.6%
active length	$l$	m	<0.01%
geom. factor	$R/Q$	$\Omega$	1%

With  $Q_l$  calculated with eqn. 3.2 and  $\beta$  determined in eqn. 3.3, the unloaded quality factor  $Q_0$  is calculated as:

$$Q_0 = Q_l(1 + \beta) \quad (3.4)$$

For example,  $Q_0$  for the TESLA-style cavities is in the order of some  $10^{10}$  at  $T = 2$  K and assuming  $\beta = 1$ , the decay time  $\tau_l$  is longer than 1 s.

With the knowledge of the dissipated power  $P_{\text{diss}}$ , eqn. 1.16 leads to the accelerating field, including the active length  $l$  of the cavity and the number of cells  $n$ :

$$E_{\text{acc}} = \frac{\sqrt{P_{\text{diss}} \frac{R}{Q} Q_0}}{n l} \quad (3.5)$$

The measurement errors are summed up in Table 3.1. The attenuation of the cabling, the directional coupler and other rf components are measured in advance of the test, but the measurement uncertainties with the power meters itself, in particular the power gauge heads have to be considered [87]. Another source of uncertainty is the determination of the decay time  $\tau$ , as already a small uncertainty in the determination of the start of the decay causes substantial variations in  $\tau$ . The errors in  $\tau$ ,  $l$ ,  $f_0$  and  $R/Q$  are estimated.

There are other measurement procedures to test the cavities with equipped helium vessel in a horizontal cryostat [88], or test a whole module in the cryomodule test bench (CMTB) facility [89] at DESY.

### 3.3 Diagnostic tools

For understanding cavity behaviour, especially the thermal breakdown, several diagnostic tools are in use at DESY. Temperature mapping (T-map) and quench localisation using second sound determine the quench location during the vertical rf test. The thermal breakdown creates a local hotspot on the inner cavity surface, and the heat propagates to the exterior of the cavity and the temperature change or the



heat pulse can be measured. Optical surface inspection gives evidence for surface irregularities and can be used to match these irregularities with quench locations.

### 3.3.1 Temperature mapping

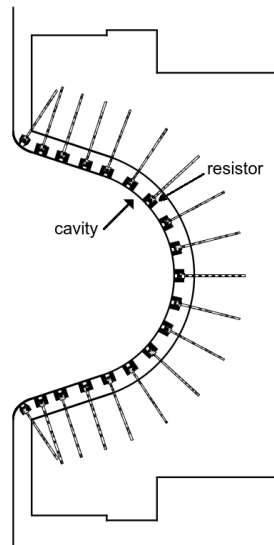


**Figure 3.4:** Temperature mapping resistor card for a single cell cavity [23]: The resistors are mounted along the cavity and are placed on the cavity surface to measure temperature changes during rf exposure.

Thermal breakdown of superconducting cavities is accompanied by the development of a local hotspot. So an obvious method to determine the location of the quench is to measure the temperature distribution on the whole cavity surface. Therefore temperature dependent resistors or diodes with good sensitivity at very low temperatures (up to 10 K) are attached in an array on the cavity surface. Details about the development of a T-map system for a single-cell 1.3 GHz cavity at DESY are given in [23]. An example for a resistor card which is attached on the cavity surface is shown in Fig. 3.4.

At DESY there are three temperature mapping systems available [90]. A nine-cell rotating T-map (see Fig. 3.5) [91], the single-cell T-map mentioned before and a quick T-map consisting of 72 resistors monitoring the heat distribution at one single equator. The resolution of the temperature mapping systems is in the order of 1 cm. An example for a 9-cell temperature map is given in Fig. 3.5.

The assembly of the temperature mapping systems mentioned before is time-consuming. In the case of the rotating T-map system, the measurement itself takes about one hour for a full temperature map, a new detection method using the second sound [92,93] in superfluid helium has been developed at Cornell University [94] and is also applied at DESY, as described in the following.

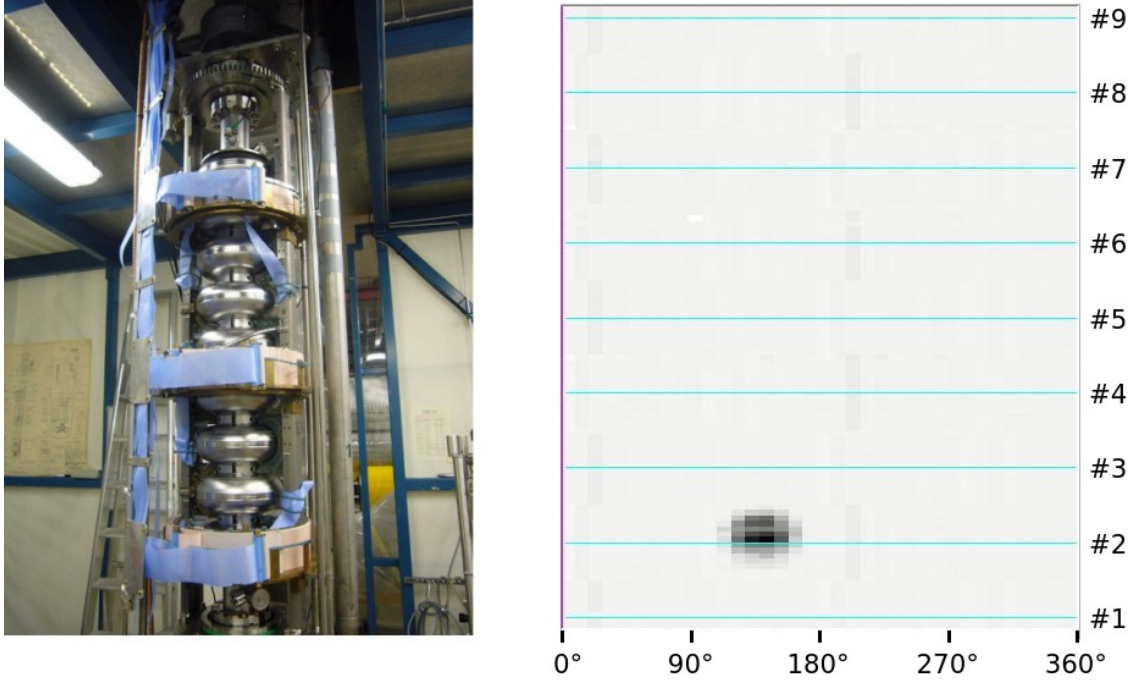


**Figure 3.5:** Left: Picture of the mounted 9-cell rotating temperature mapping system at DESY [90]. Right: example for a temperature map with angular position and equator number, the darker the greyscale, the higher the surface temperature.

### 3.3.2 Quench localisation using second sound

About 60 of the second sound detectors have been manufactured; four vertical inserts have been equipped with eight sensors each to apply the second sound method for the cavity tests at DESY in the course of this work. The system is in regular use since beginning of 2011 [95].

#### Second sound in superfluid helium

If liquid helium is cooled below a temperature of  $T = 2.17\text{ K}$ , it becomes a superfluid (He II). As the cavities are tested and operated at  $T = 2\text{ K}$  and  $T = 1.8\text{ K}$  respectively, according to [92] liquid helium can be described as a mixture of He II and liquid helium (He I). The overall helium density is  $\rho$ , which can be calculated with

$$\rho = \rho_n + \rho_s \quad (3.6)$$

with  $\rho_n$  being the density of the normal liquid helium and  $\rho_s$  of the superfluid helium. For the subsequent explanation of the detection method for second sound it should be noted that the viscosity of the superconducting phase  $\eta_s = 0$ . For  $T = 0\text{ K}$  the density  $\rho = \rho_s$  and for  $T \geq 2.17\text{ K}$  it is  $\rho = \rho_n$ , as  $2.17\text{ K}$  is the lambda point temperature for  $^4\text{He}$ . The total mass current density with the related flow velocities

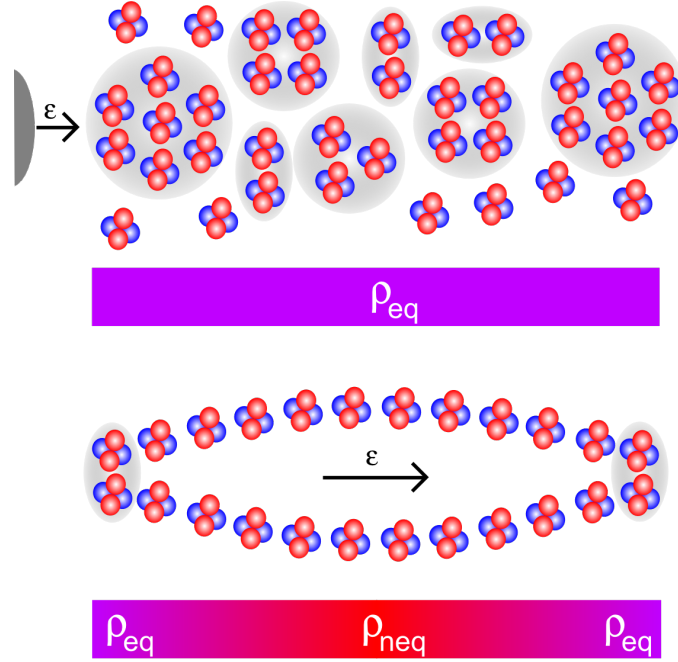


**Figure 3.6:** The propagation of second sound. Top: An energy pulse  $\epsilon$  breaks up helium II (grey spheres with helium nuclides) locally. Bottom: This results in a disequilibrium, which is compensated by counterflow of helium I.

$\vec{v}_n$  and  $\vec{v}_s$  reads:

$$\vec{j} = \rho_n \vec{v}_n + \rho_s \vec{v}_s. \quad (3.7)$$

By describing the fluids with hydrodynamics [92], the mass flow and propagation of each helium phase can be characterised with the continuity equations:

$$\begin{aligned} \frac{\partial \rho_n}{\partial t} + \vec{\nabla} \cdot (\rho_n \vec{v}_n) &= 0 \\ \frac{\partial \rho_s}{\partial t} + \vec{\nabla} \cdot (\rho_s \vec{v}_s) &= 0 \end{aligned} \quad (3.8)$$

The cryostat provides a stable temperature by keeping the pressure constant via pumping, so the overall flow  $\vec{j}$  in (3.7) yields

$$\vec{j} = \rho_n \vec{v}_n + \rho_s \vec{v}_s = 0 \quad (3.9)$$

as an 'infinite' cooling reservoir is provided. Thermal breakdown creates a heat pulse, and the corresponding energy is deposited into the helium bath and breaking up the superfluid phase locally, as shown in Fig. 3.6. This results in a local disequilibrium of the overall density  $\rho$ . The energy travels according to (3.8) in one direction. To restore equilibrium, the superfluid phase mixes with the normal fluid phase by flowing in the opposite direction, which is indicated in (3.9).

### Detection method

The detection of the second sound wave can be done by using thermometers for measuring the small temperature change [96]. Another method is to detect the propagating wave of the phase transition directly with capacitor microphone-like oscillating superleak transducers (OST) (see Fig. 3.7) [97]. These devices consist of a body made of aluminium, a centered brass electrode electrically insulated from the body and a thin porous diaphragm sputtered with a thin gold layer at the outside (see appendix A.3). A voltage is applied between the brass electrode and the body/diaphragm, and the voltage changes due to the excitation of the diaphragm by the pressure induced by helium I and counterflow of helium II are amplified and measured. A descriptive drawing of the detection method is shown in Fig. 3.7, for the amplifier setup see appendix A.4. The second sound wave propagates as spherical wave from the exterior of the quench location, so the detection is also possible if the detectors are not in line-of-sight. But this is not necessary if a set of eight OSTs is used in a special arrangement described in the next section, as four OSTs are always in line of sight of the quench location. If the quench does not occur too close to a cavity iris, the uncertainty introduced assuming a straight line between OST and quench location is in the order of a few millimeters.

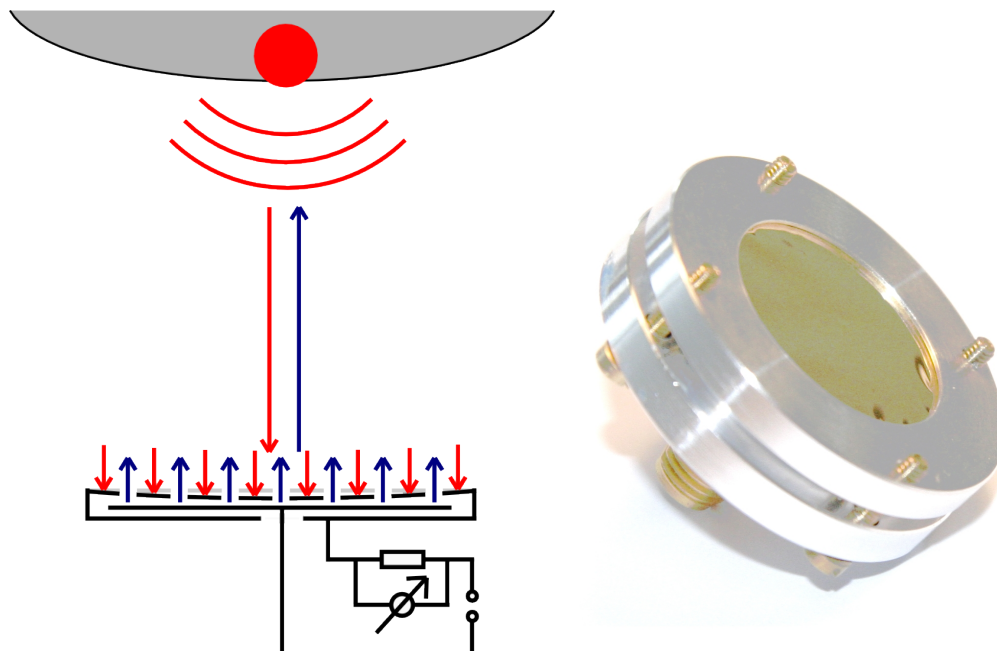


**Figure 3.7:** Left: Functionality of an OST [95] - helium I (red) is not able to pass the thin diaphragm, while helium II (blue) flows through the small capillaries to compensate the disequilibrium in density in front of the diaphragm. The voltage change induced by the movement of the diaphragm can be measured. Right: Picture of an OST [95].

### Measurement setup

In the vertical cold tests at DESY, a set of eight OSTs per insert is in regular use since 2011 [95, 98]. Two OSTs each are placed at equator level of cells 2, 4, 6 and 8 with a rotation of about  $90^\circ$  to  $120^\circ$  between each set, depending on the fixture at the insert. The readout of a multiplexed USB-ADC with a sampling rate of 10 kHz per channel acquiring the second sound signals and the reflected power is done with a MATLAB<sup>®</sup> program. If the quench limit of the cavity is reached, the reflected power rises abruptly, which is an indication for a quench. The time difference between this rise and the oscillation onset on the OSTs is the measured propagation time of the second sound, which determines the distance between OST and quench location with the known values for the velocity [99]. An example of an acquired dataset is given in Fig. 3.8.

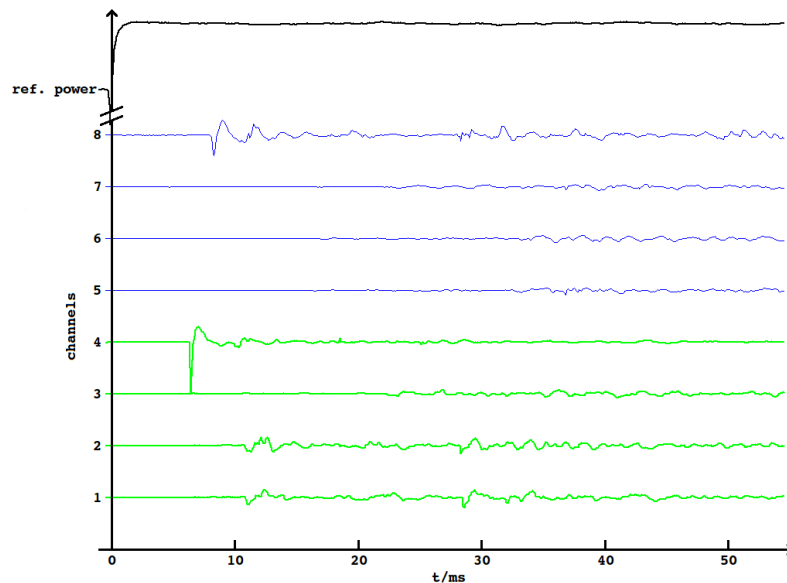


**Figure 3.8:** Second sound dataset from cold rf test of cavity AC156, test 3 in  $\pi$ -mode. On top, the reflected rf power is shown and the thermal breakdown event has been set to  $t = 0$  intentionally. Below, the eight OST signals are displayed, green indicates the use of the signals 1-4 for quench localisation. Signal 8 was not in line of sight and not chosen [95].

To optimise the second sound signal and to reduce velocity uncertainties due to small temperature changes (for detailed information about velocity vs. temperature see [99]), the second sound measurements are carried out at a helium bath temperature of 1.8 K, which corresponds to a propagation velocity of  $v = 19.9$  m/s. A schematic drawing of the OST setup including a localisation example from the previously shown data in Fig. 3.8 is shown in Fig. 3.9.

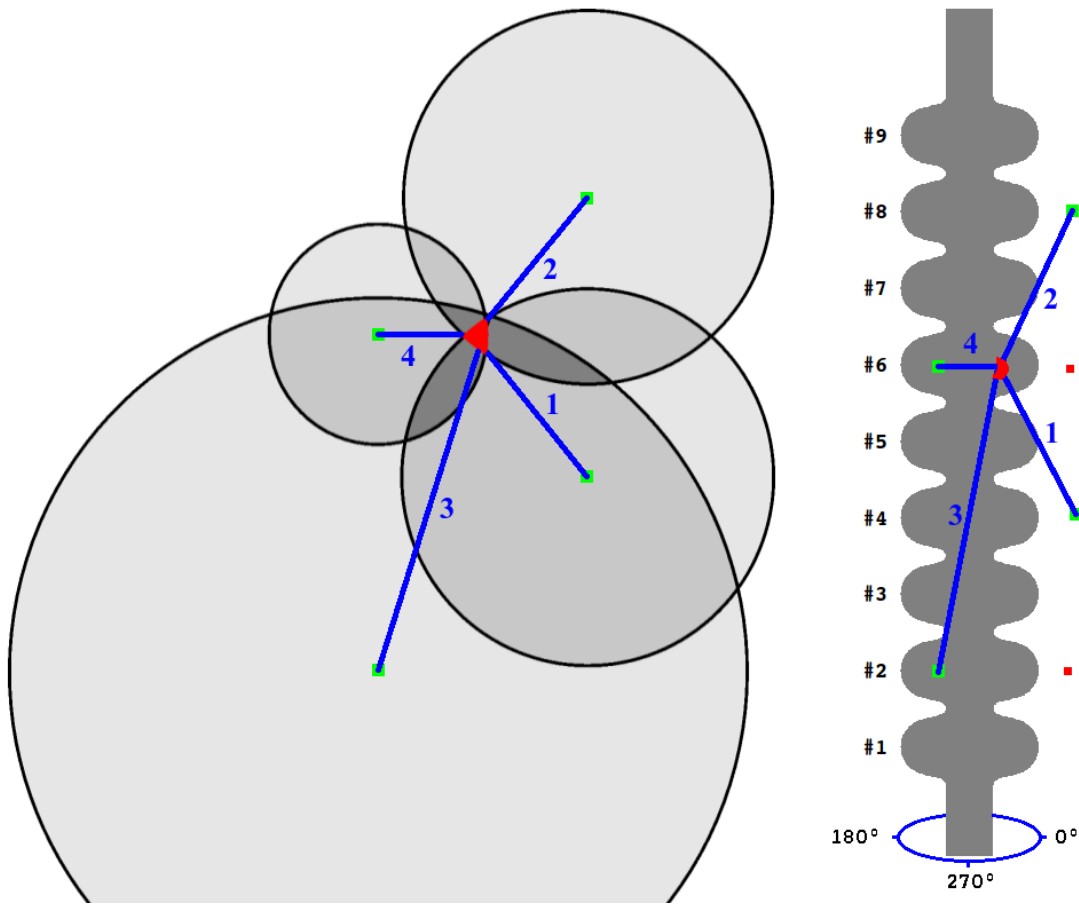


**Figure 3.9:** Example for quench localisation using second sound [95]. The OSTs 1-4 (green) have been used to determine the quench location (red area) by measuring the propagation time of the second sound, as indicated in Fig. 3.8, OSTs 5-8 are in the back of the cavity (red squares or hidden).

### Quench localisation and uncertainties

The localisation of the quench spot requires at least three detected signals from close detectors. As discussed in [100] and in the analysis in chapter 4, the measured propagation times are shorter than expected, usually in the order of 1 – 1.5 ms resulting in missing 2 – 3 cm of propagation path. A possible explanation is the heat propagation [101]: The energy spreads faster in the niobium compared to the propagation of second sound, and the position determined by the OSTs is not necessarily the quench spot, but a location at the boundary of the heated niobium area. With the assumption of a uniform distribution of the heat around the quench location, a measurement with three or four detectors allow the determination of the quench location in a similar resolution than temperature mapping.

The determination method of choice has been described in detail in [102], only the key features will be given here.

As simple triangulation does not result in a quench position on the cavity surface

for reasons mentioned before, a constrained nonlinear optimisation with geometrical constraints is done. The minimisation function reads

$$f(\vec{x}) = \sum_{i=1}^n \left( \frac{|\vec{x} - \vec{p}_i| - r_i}{\sigma} \right)^2 \quad (3.10)$$

with  $\vec{x}$  as position of the quench location,  $\vec{p}_i$  the position of the  $i$ -th OST,  $r_i$  the calculated propagation distance, which forms a spherical surface with radius  $r_i$  and  $\vec{p}_i$  as center. In addition, the mandatory geometrical constraint is the cavity surface, which has been implemented in the program and can be adapted easily to other cavity shapes. The function  $f(\vec{x})$  is minimised with regard to the constraint, and as the OSTs are placed in at least three different directions, the algorithm minimises towards the center of the heated area, as the 'missing' propagation time is identical within the measurement uncertainties for each signal [101].

Two measurement uncertainties in the method itself have to be considered: The precise determination of the quench time and the measurement of the propagation time. While the determination of the quench time is possible within a precision of  $\Delta t_{\text{qt}} = 0.2 \text{ ms}$  because of the uncertainty in hitting the rising edge of the reflected power signal, the larger uncertainty arises from the dimensions of the OST. The exposed diameter of the diaphragm is about 18 mm and the upper limit for the uncertainty is  $\Delta t_{\text{OST(max)}} = 0.9 \text{ ms}$ , which results in an overall error of  $\Delta t \approx 1 \text{ ms}$  and (using  $v \approx 20 \text{ m/s}$ ) 2 cm or  $\approx 10^\circ$  at the equator in displacement. The use of smaller OSTs might increase the accuracy as the surface of the diaphragm is smaller, but the tradeoff is a lower sensitivity for the same reason. An additional uncertainty occurs due to the length of the cells and the cavity. It depends on the tuning process and the uncertainty in cavity length is in the order of millimeters. But this is negligible compared to the measurement uncertainty of each OST.

A simple estimation of the measurement uncertainties with 4 detector signals yields  $\frac{\sigma}{\sqrt{n}} = \frac{2 \text{ cm}}{\sqrt{4}} \approx 1 \text{ cm}$ , which seems reasonable in comparison to temperature mapping data. The use of a larger number of OSTs can reduce the uncertainties given by the OSTs explained before, but the best accuracy possible could be achieved if the local thermal conductivity properties of the niobium are known in detail. This allows a calculation of the heat spread in the niobium and this can be compared with the second sound propagation to find the minimum of the propagation time between quench position and the OSTs.

### 3.3.3 Optical surface inspection

One step to understand the origin of thermal breakdown is the inspection of the inner surface of the cavity, especially at the equator welding seams and the surrounding area. For the 1.3 GHz 9-cell cavities of the TESLA-type a camera system has been developed in a collaboration of KEK and University of Kyoto [103], a schematic overview of the camera is given in Fig. 3.10. The camera provides pictures with a

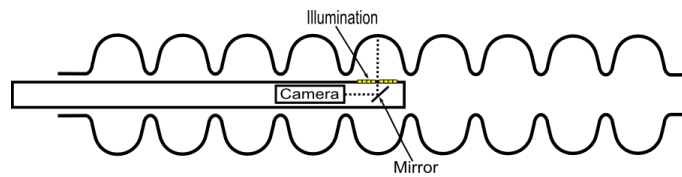


**Figure 3.10:** Schematic drawing of the Kyoto Camera System in use at DESY. The illumination of the surface is done with illumination stripes attached on the camera tube left and right of the camera opening [104].

size of 3488x2616 pixels and a resolution of 3.5  $\mu\text{m}$  per pixel [105]. An example for a picture taken with the camera system at DESY is shown in Fig. 3.11.

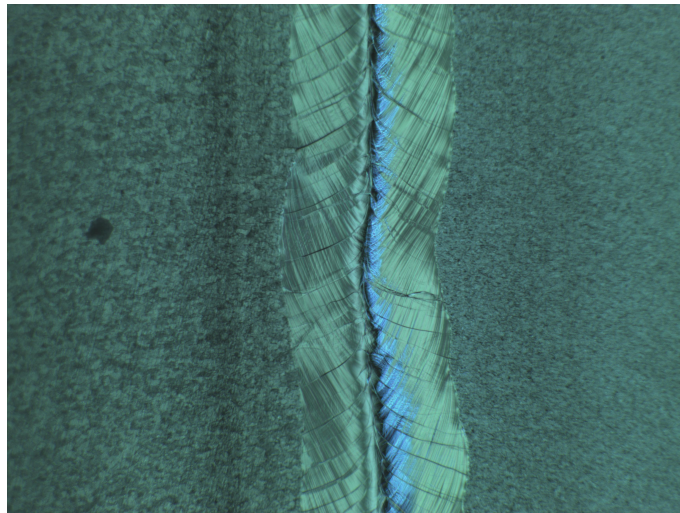


**Figure 3.11:** Picture of the inner surface of a cavity at the equator weld (center). On both sides of the welding seam the bulk niobium with its fine grain structure can be seen [26].

The fine structure of the bulk niobium shows the importance of a camera system with a high resolution as it is provided by the camera system. As mentioned earlier fine niobium grains have a diameter in the order of 50  $\mu\text{m}$ . The structure of the surface can be analysed and correlations between surface irregularities and quench locations determined during a rf test can be found.

A large number of cavity inspections have been done manually at DESY since 2008 [106] with an improvement of the camera system in 2009: A new illumination system and a camera sensor with higher resolution has been commissioned [107]. For the automation of the surface inspection recently the Optical Bench for Automated Cavity Inspection with High Resolution on Short Time Scales (OBACHT) [26] (Fig. 3.12), an automated cavity inspection system has been brought into service. The main control for steering of OBACHT has been created for initial commissioning. It communicates with the programmable logic controller (PLC) to steer the



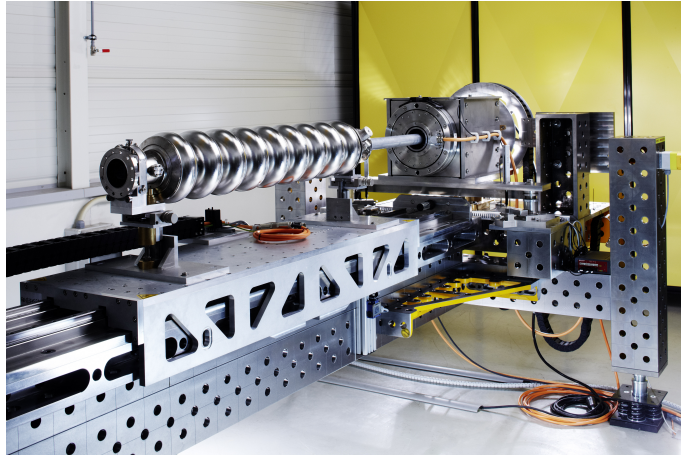


**Figure 3.12:** The OBACHT cavity surface inspection system: The cavity to be inspected is mounted on a linear movable sled, and the camera tube is fixed in a torque motor and rotates in the cavity.

motor system. As the measurement should run autonomously, different calibration and safety measures, in particular a collision free movement, have to be included. The length of the cavities varies in the order of 1 mm, which requires a calibration of the equator position for every single cavity. In addition the position of the main coupler port, which is taken as  $0^\circ$  in the cavity coordinate system, has to be determined. After these calibrations are done, the cavity and the camera are moved according to a table with the cavity positions to be inspected. The illumination and the picture taking process is done with an image acquisition software [108]. Currently the implementation of an automated evaluation of the cavity pictures is in progress [109], since 2790 pictures are taken during a full inspection cycle and a manual evaluation is cumbersome and time-consuming.

### 3.3.4 Defect Treatment

It has been found that in several cases the quench location corresponds to a defect found on the cavity surface and thus limit the accelerating field. These defects appear due to welding irregularities or treatment nonconformities (e.g. [65,98,106]). In order to minimise the effects of defects as quench trigger, a worldwide effort is ongoing to find repair methods for such spots. As these methods are still in the research phase, they are not foreseen for the European XFEL series.

One approach is repairing only the defect area by smoothing the defective area. One possibility for such a process, introduced in [110], is grinding the surface locally at the suspicious position followed by EP. As the size of the defects observed are usually in the order of some ten to hundreds of microns, another way of smoothing the surface is re-melting the location using a laser beam again followed by light EP [111,112]. These two different ideas are subject of research and yield improvements

### 3 Cavity performance test

---

of the limiting accelerating gradient as reported in the mentioned references. The installation of a local grinding system at DESY is under discussion.

## CHAPTER 4

# Results of quench localisation

---

To figure out the reasons for the thermal breakdown is still the most sophisticated task in order to produce cavities reliably with high accelerating fields. Only for few quench locations it is possible to correlate a surface irregularity found with optical inspection, which have been reported elsewhere (cf. [26, 65, 106] and section 4.4). The following sections show a different approach to the quench localisation data. It was possible to measure a large sample of about 30 recent cavities including determination of the quench location, since the second sound method is about 10 times faster than temperature mapping and does not require difficult assembly (see section 3.3.2). This dataset is introduced in the next section and statistical features are worked out in the following [113].

### 4.1 Data sample

The analysis of quenches located by second sound [95] is based on a sample of 31 cavity tests carried out from April 2010 to May 2012, including cavities from several production series [114] and the reference cavities produced for the European XFEL. A detailed overview of the data examined is given in appendix B.1. In most cases all passband modes of the cavities were excited so that up to nine different quench locations per cavity could be measured. Typically four to five spots were found. Depending on the passband mode the configuration of cells exposed to the peak field varies, as has been shown in Fig. 1.6. These cells are more likely to quench. The resulting bias in the distribution has to be corrected for. Some cavities are not quench-limited in all modes (or the quench location could not be reconstructed). The standard  $\pi$ -mode exposes all cells to the same field; 26 quench locations were so identified. For all other modes ( $8/9\pi$  to  $1/9\pi$ -mode) 18-22 quench locations have been measured. The analysis takes into account the cells exposed to the highest field (up to 4 maximum) and otherwise assumes an equal probability for quench in each of these cells. Fig. 4.1 shows the coordinate system [115] used for the cavities of the European XFEL, which is also used in this analysis.

## 4 Results of quench localisation

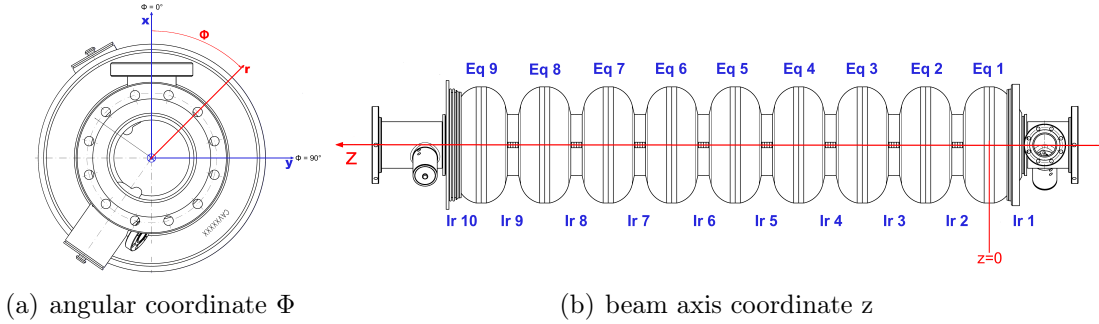


**Figure 4.1:** The coordinate system of the 1.3 GHz cavities, which is used for the following discussion.

The data sample includes all quenches from pure thermal breakdown (BD) and those quenches that occur in conjunction with radiation induced by field emission, where the threshold has been placed at  $10^{-2}$  mGy/min. The latter quenches are referred to as BD\_FE. An overview of all different quench locations found is given in Fig. 4.2. For ease of reading, the  $z$ -coordinate has been replaced by cell numbers and the horizontal grid marks the equator positions. The coordinates are transformed as  $z = 115.4 \times (x - 1)$  mm, where  $x$  is the cell number.

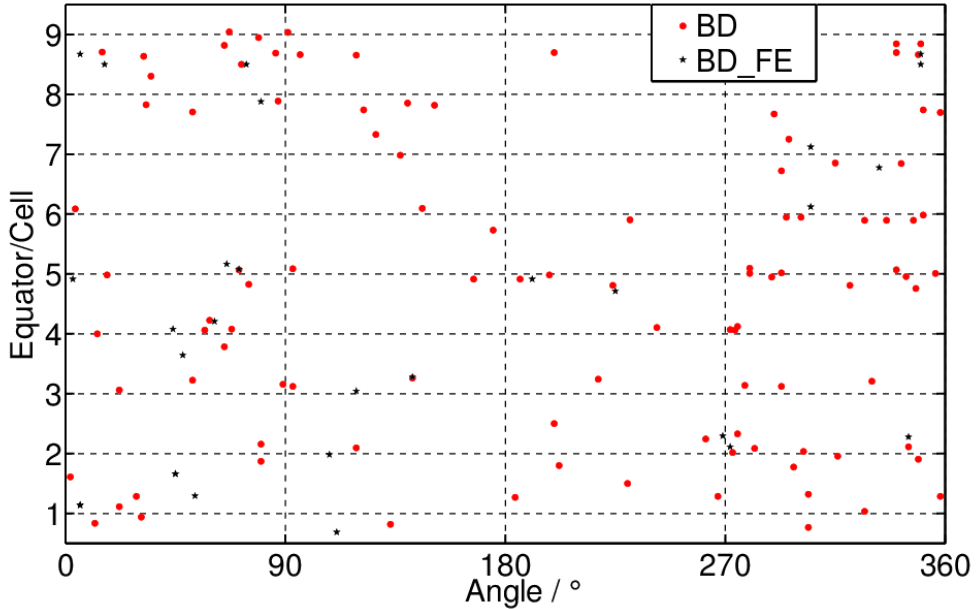


**Figure 4.2:** Scatter plot of all 189 quench locations determined by second sound at DESY. The angle is given as described in Fig. 4.1. The two breakdown situations are distinguished: BD without and BD\_FE with significant field emission.

The observed distribution is not uniform. The region between  $270^\circ$  and  $90^\circ$  registers

more quenches than the center of the plot. In addition the outer cells (1-2 and 8-9) also suffer more often from quenches than the inner cells. The large number of quenches along cell 5 is expected, since this cell is exposed to the highest fields in five of the nine passband modes.

In the following sections the distribution of the quench locations along the cavity (and cell) z-axis (section 4.2) are discussed. Followed by investigation of the angular distribution (section 4.3) and conclude with some correlations found between quench locations and defects found by optical inspection in section 4.4.

## 4.2 Quench distribution along the cavity axis

The total number  $N$  of quenches sums up to 189 and contains all events of thermal breakdown including the cases with excessive field emission. With the origin of these quenches largely unknown a random source has been assumed as a cause. Hence, assuming naively a uniform distribution of these  $N$  events leaves 21 quenches on average for each cell. Simplifying this number is taken as the expectation for the number of quenches in each cell. The thermal breakdown will occur preferentially in one of the cells containing the maximum rf field as has been confirmed e.g. in [65]. Correspondingly the number of modes generating the maximum field in each cell have to be considered as well: for cells 2 and 8, there are 2 passband modes (cf. Fig. 1.6) where the rf field reaches the maximum amplitude, cell number 5 is exposed to the maximum rf field in all odd  $\frac{n}{9}\pi$  passband modes. All other cells experience 3 modes with peak field. So a total of 27 cells (configurations) with highest fields can be distinguished; on average there are three quench possibilities per cell.

As a consequence the expected number  $E(x)$  of quenches for each cell  $x$  is calculated as follows:

$$E(x) = \frac{\text{modes with maximum field in cell}(x)}{27} \times N. \quad (4.1)$$

Note that no uncertainty is attributed to the number  $E(x)$ , which is simply taken as the expectation value for the number of quenches for this sample. The following study will reveal whether this assumption is supported by the data.

The observed number of quenches per cell is shown in Fig. 4.3, including the expected value  $E(x)$  marked by a dashed line. In the absence of further information on each cavity and cell all measurements are treated independently. The uncertainties given in the plots in this section are the statistical standard deviation of a binomial distribution. It is obvious that there is a large difference between the expected quench number and the measured frequency in cell 2. While there may be a few false attributions to cell 2 due to field emission confused at the irises between cells 1-2 or 2-3 this number is sufficiently small not to affect the basic observation.

First considerations included a surface contamination by dust, humidity or gas residuals, since the flange at this end of the cavity is the last one mounted inside the

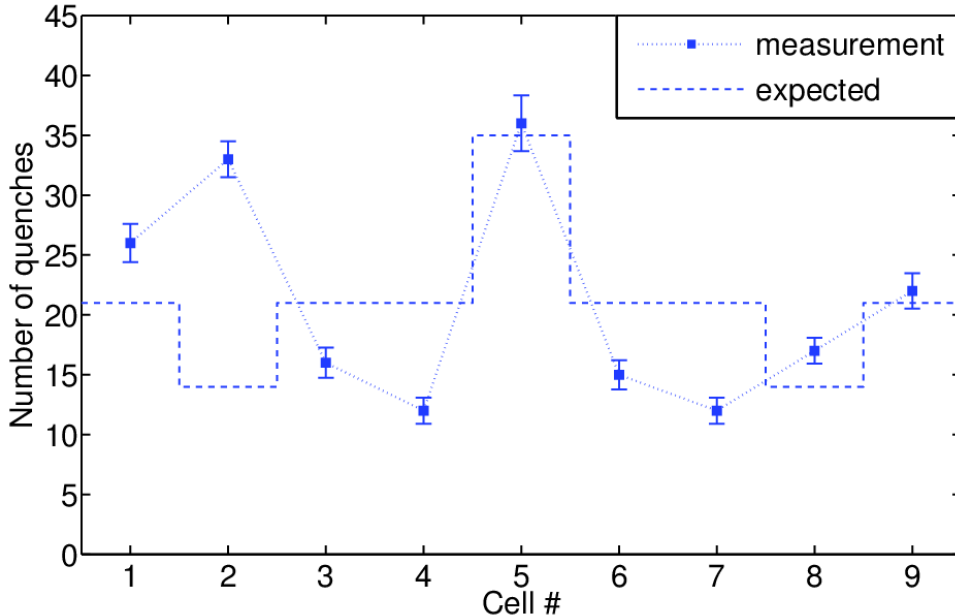


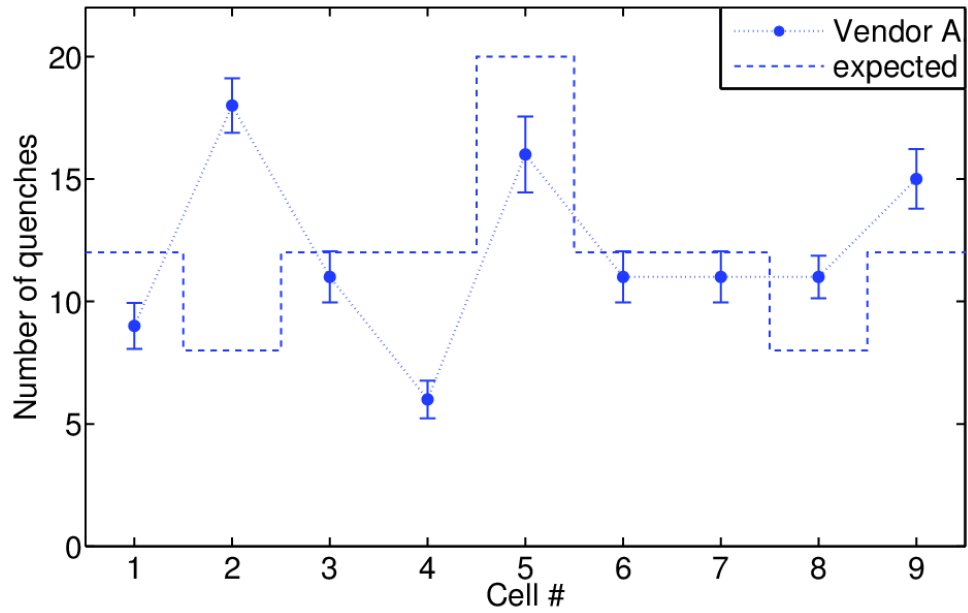
**Figure 4.3:** The total number of quenches observed in each cell. The dashed line shows the expected number of quenches, which accounts for the varying number of cells with maximum rf field in the nine passband modes.

clean-room. The cavity is pumped and vented from this side and the connection to the pumping system is done in a separate clean-room. The chance of such a contamination is low due to the handling experience gained in the cavity treatment and assembly at DESY [116], so further investigation is done by analysing the results of each cavity vendor separately.

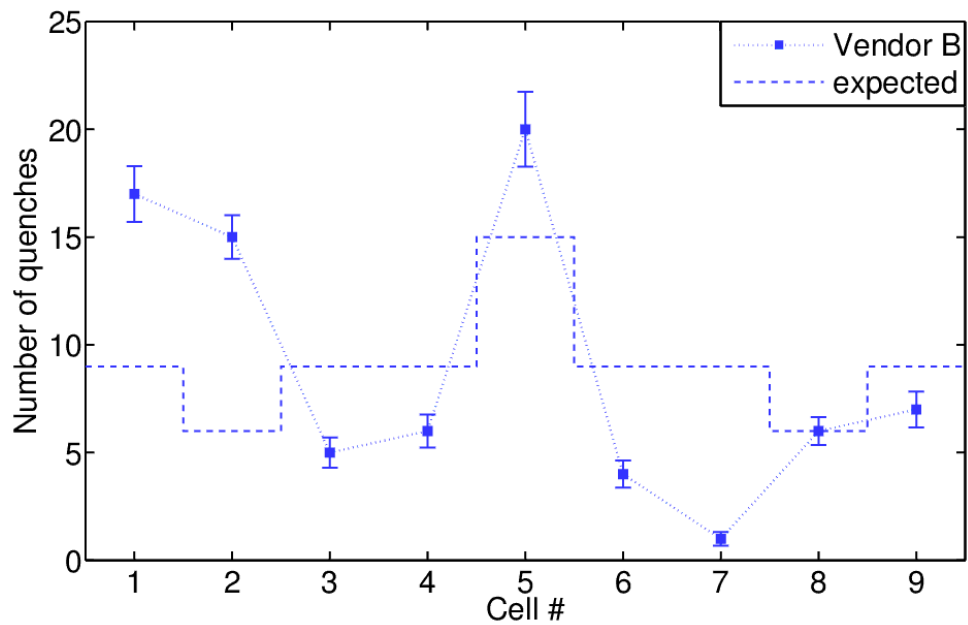
### Vendor dependency

Specific details of the cavity manufacture and in particular the manufacturer can also create the difference between observation and expectation of the number of quenches. This correlation is explored in Fig. 4.4 which differentiates the distribution of Fig. 4.3 by vendor engaged in providing cavities to DESY. While the number of counts for cells 3 to 9 are within the expected range or even less, for cell 2 a large excess is seen at both vendors. Cell 1 shows a distinctly different behaviour: while for vendor A the number of counts are in the expected range vendor B exhibits a number of quenches  $4\sigma$  beyond expectation. Within the limited statistics there are strong indications that different production processes at the vendors cause this difference in the distribution, especially for end-cell 1 [117].

Assuming constant probability  $p(x)$  for a quench to occur in cell  $x$  at a given field, the distribution of Fig. 4.4 can be cast into a probability which are shown in Fig. 4.5. Here the probability  $P(n \geq k)$  that the number  $n$  reaches or exceeds the number



(a) Vendor A



(b) Vendor B

**Figure 4.4:** Observation of quenches per cell, separated for each vendor. The dashed line shows the expected number for each cell.

$k$  of observed quenches in the sample is shown. In analogy to 4.1 the individual probability is defined as

$$p(x) = \frac{\text{modes with maximum field in cell}(x)}{27} \quad (4.2)$$

and

$$P(n \geq k) = \sum_k^n \binom{n}{k} p^k (1-p)^{n-k}. \quad (4.3)$$

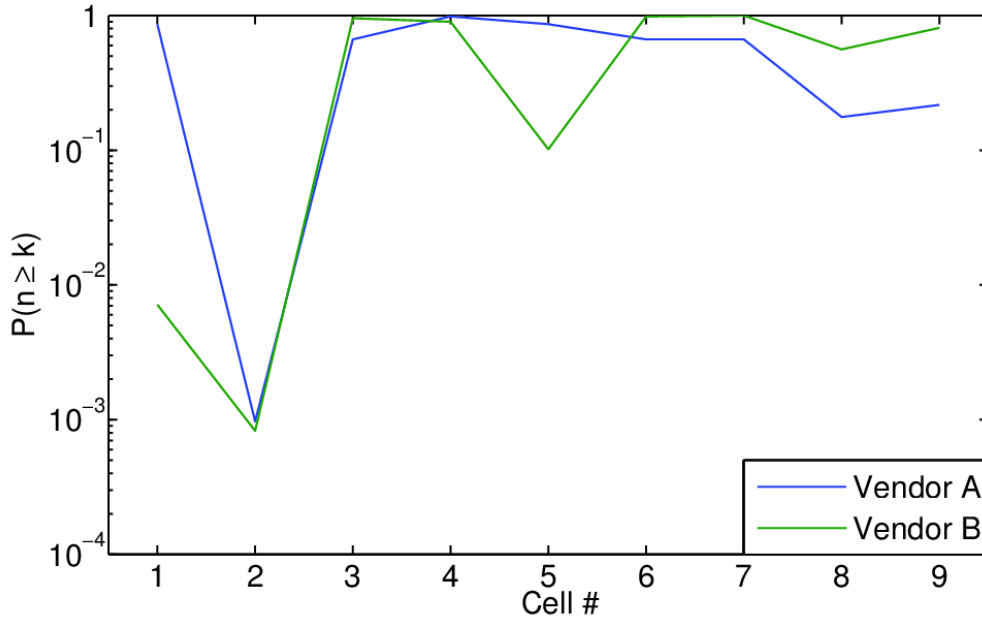


**Figure 4.5:** The probabilities for the quench distribution as shown in 4.4.

The observation in Fig. 4.5 shows that the number of quenches occurring in cell 2 are very unlikely with  $P \approx 10^{-3}$ , while for cell 1 it varies for each vendor: for vendor A the probability is  $p \approx 0.86$ , but for vendor B it is  $p \approx 7 \times 10^{-3}$ , as already has been shown in Fig. 4.4.

### 4.2.1 Distribution within a cell

For the following observations only the thermal breakdowns with no or low field emission are used, since for quenches with high field emission other mechanisms like the deposition of energy by electrons hitting the cavity might be at work. In addition quenches happening in the iris region cannot be associated reliably with a specific adjacent cell.



The allocation of the quench locations in Fig. 4.2 shows a feature which has to be corrected: Most of the locations determined in cell 1 and 9 are far off the equator region. This accounts to the known fact, that the propagation times of the second sound are usually too short using the known velocity [100] and the heat propagates faster along the niobium than the second sound wave in helium [101]. Nevertheless, comparison of second sound data with temperature mapping shows good agreement of the locations in all other cells and only a shift in z-direction in the end cells [65]. For a correction of this shift the data of cells 2-8 have been summed up and result in a Gaussian distribution shown in Fig. 4.6. Assuming the equator of a cell as '1'

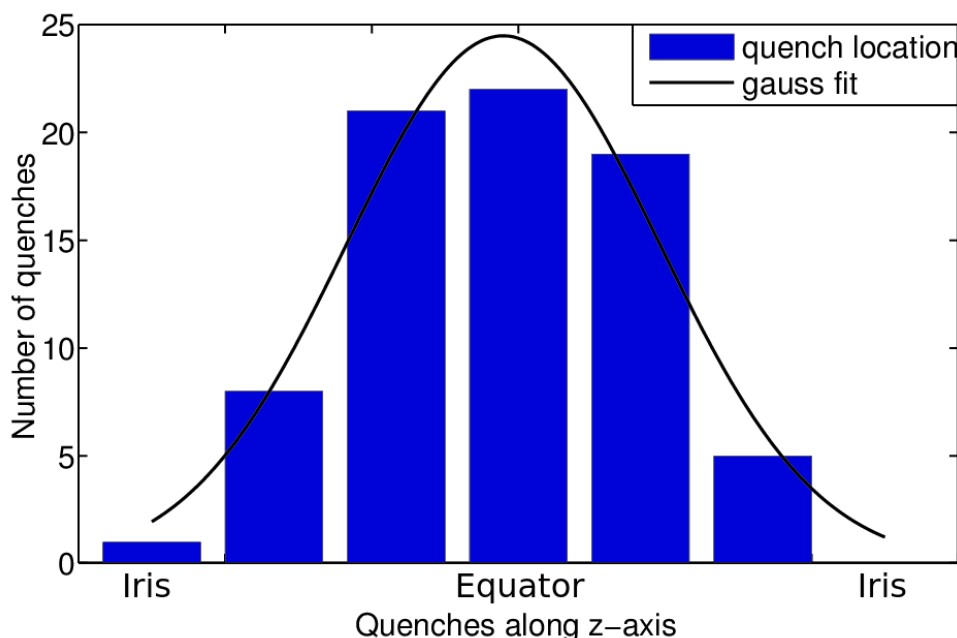


**Figure 4.6:** Distribution of all thermal breakdown locations in cells 2-8 without or low field emission, summed up. In addition, a gaussian fit is shown.

and the irises as '0.5' respective '1.5', a Gaussian fit  $f(x) = a_1 \times \exp\left(-\left(\frac{x-b_1}{c_1}\right)^2\right)$  and  $c_1 = \sqrt{2}\sigma$  yields  $b_1(\text{cell}(2-8)) = 0.98 \pm 0.05$  as mean value, yielding an equal distribution on the left and right half cell. The Gaussian fit for the data of cell 1 yields  $b_1(1) = 1.3 \pm 1.6$  and for cell 9  $b_1(9) = 0.70 \pm 0.08$  respectively. Moving the centres of the data of the end-cells towards  $b_1(\text{cell}(2-8))$ , by setting  $b_1(1) = b_1(9) = b_1(\text{cell}(2-8))$  results in a Gaussian distribution with  $b_1(\text{cell}(1-9)) = 0.99 \pm 0.03$  shown in Fig. 4.7. Some results at the iris region can be neglected: One of the events recorded is in high-field cavity AC155 with 45 MV/m, resulting in difficulties to determine the quench location as the heat load into the helium bath exceeds 100 W and keeps the bath in disequilibrium. Another event in AC158 shows a

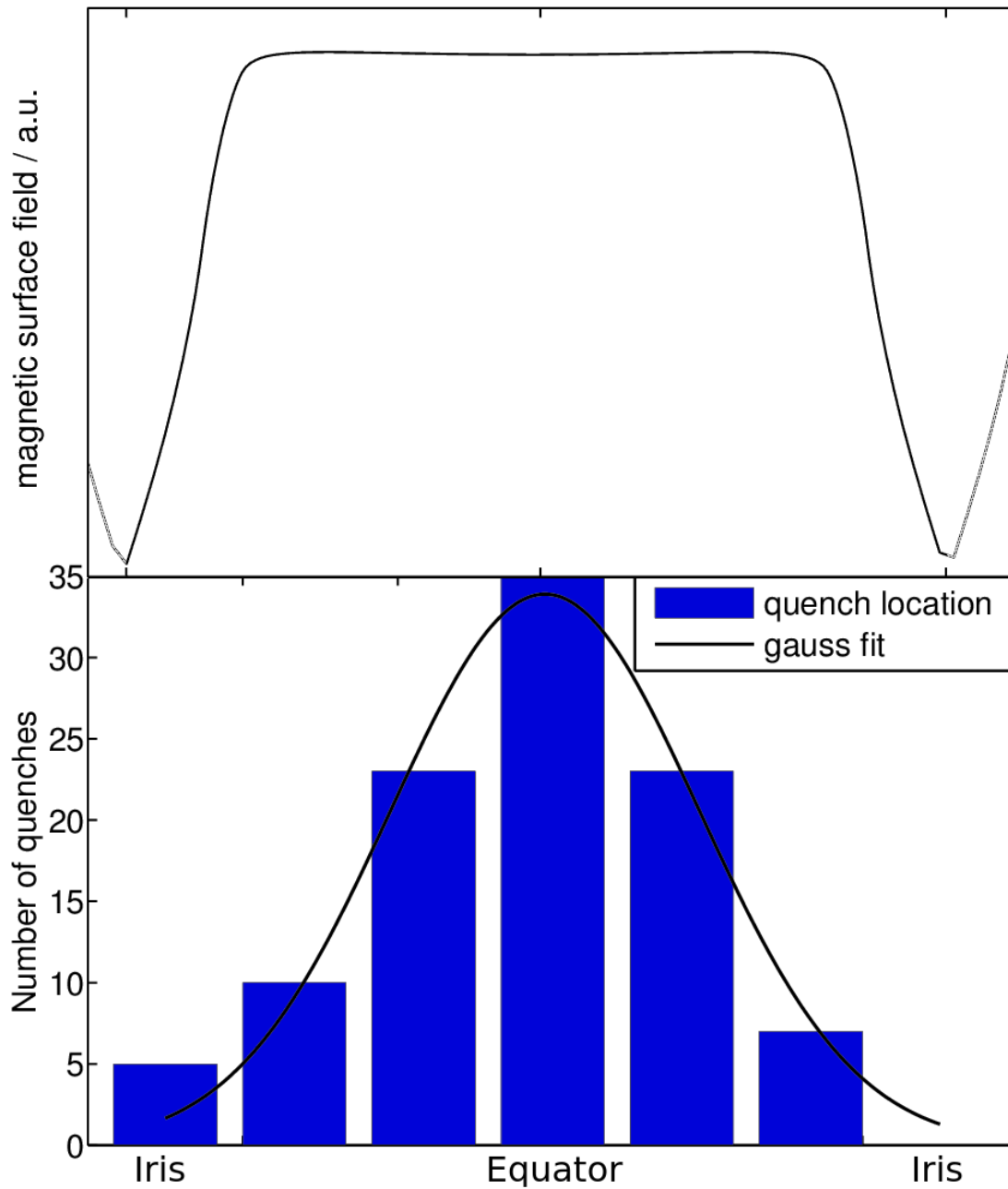


**Figure 4.7:** All quench locations without or only low field emission, more than 80% of the quench locations distributed in the high magnetic surface field region. For comparison, the surface magnetic field along the z-axis is shown above [118].

quench location in cell 1 in  $1/9\pi$  mode which does not make sense after comparison with the mode measurements, as the lowest fields are achieved in cells 1 and 9 in  $1/9\pi$  mode.

The result of this analysis in Fig. 4.7 shows that irregularities at the equator weld

are not inevitably the cause for thermal breakdown. Also the zones next to the equator weld, which have been exposed to heat during the welding procedure, show a large number of quenches. As the magnetic field during rf exposure reaches highest values in this region (Fig. 4.7 top), already small irregularities may cause a quench.

### 4.2.2 Fields at thermal breakdown

Besides the quench location the achieved quench field is the most important parameter for this study, because it gives evidence of the accelerating field possible of each cavity. Quenches with excessive field emission (BD\_FE) are not taken into account. To achieve unbiased statistics, from now on quench locations occurring in multiple modes have been filtered out by allowing no additional quenches within a limit of  $\Delta z = \pm 20$  mm and  $\Delta\Phi = \pm 10^\circ$  around a previous quench location. This results in 103 events to be included in this analysis.

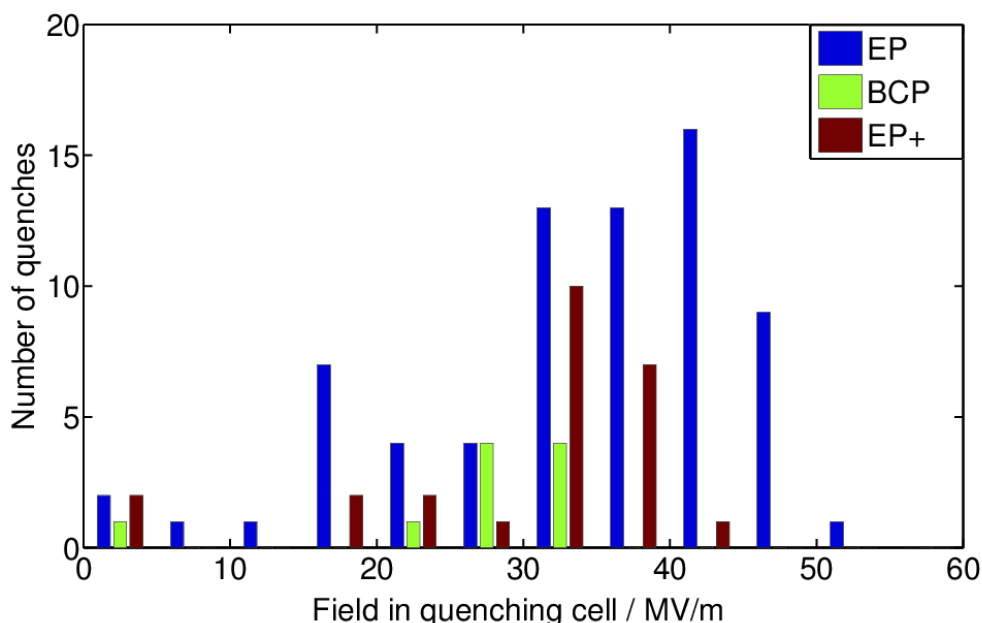


**Figure 4.8:** The number of quenches related to the field achieved in the quenching cell with 5 MV/m binning.

It has been reported elsewhere [64, 65] that cavities and hence the cells undergoing BCP treatment usually do not exceed values of about 30 MV/m, which also can be seen in Fig. 4.8, although the binning yields several quenches above 30 MV/m. The quenches with maximum field and BCP treatment reach 33 MV/m and 34 MV/m while the rest of the BCP sample of nine quench locations quenched already below 32 MV/m. The BCP Flash (additional 20  $\mu$ m BCP on a pure EP surface, also referred as EP+) treated cavities contribute up to quench fields of 40 MV/m with

one count at 42 MV/m, while the overall distribution of the quench fields is similar for BCP Flash and pure EP treatment, although the total number of cavity tests with EP surface was larger. In addition, EP+ and EP combined yields 19 quenches below 25 MV/m and 75 above, a good result for 80% of the quenching cells. The cell reaching  $> 50$  MV/m is from AC155 [24], one of the best large grain cavities [24]. The events at 0 MV/m can occur due to quenches close to the iris and result in improper assignment of the cells.

In summary, 80% of the EP and EP+ cavities exceed accelerating fields of 25 MV/m in the quenching cells, which is very promising for the European XFEL, as these treatments will be used for the 800 cavities [18].

### 4.2.3 Thermal breakdown fields in each cell

As about 25% of the non-BCP treated cells quench below 30 MV/m, the distribution of these quenches by cell is of interest. Fig. 4.9 shows the integrated number of quenches in relation to the quench field for each cell. As has been shown in Fig. 4.3, a large excess of quenches is seen in cells 1 and 2. Comparison with the quench fields show that eight out of 15 quenches in cell 2 occur at fields below 20 MV/m. A check of the underlying data indicates that cavity AC127 test 8 shows field emission below the BD\_FE threshold in  $4/9-1/9\pi$  and populate, according to the filter introduced

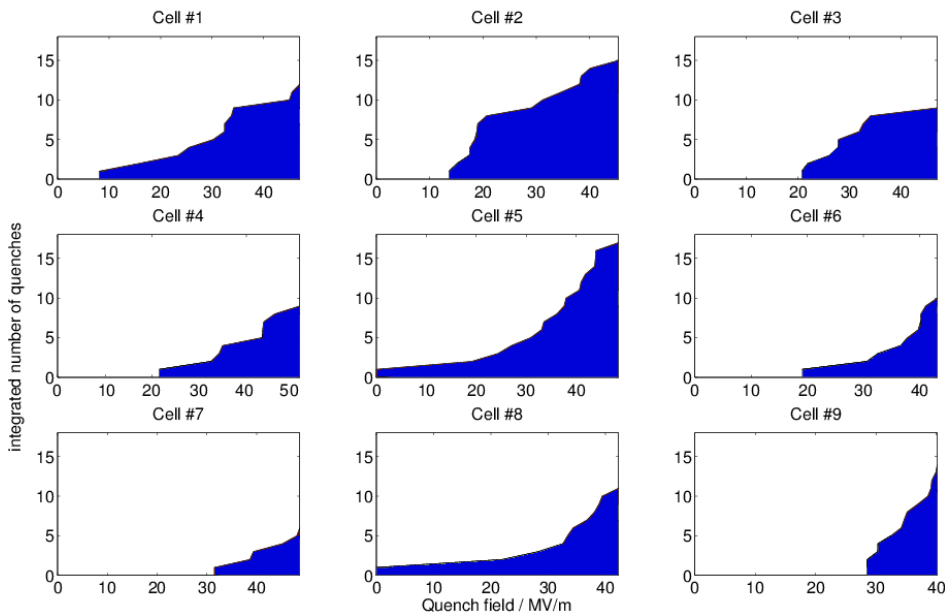


**Figure 4.9:** The integrated number of quenches corresponding to the field achieved in each quenching cell. Cell 2 showed more quenches than expected (cf. Fig. 4.3) and also shows most of the quench onsets below 30 MV/m compared to all other cells.

in the previous section, three 'different' locations in cell 2, which are most likely the same position in modes  $4/9\pi$  to  $2/9\pi$ . In addition, one of the quench locations with low field (CAV00506 test 2) has been detected close to iris 2 and cannot be properly assigned to cell 1 or 2. A few quenches below this threshold are also seen in cell 1. The quenches at 0 MV/m are errors, as the quenches appeared close to the iris region and allow no proper assignment to a cell, as described in the previous section. Cells 4 to 9 experience almost all quenches beyond 30 MV/m and show a strong increase from 30 to 40 MV/m. It seems that the suspicious cells 1 and 2 with an excess of quenches compared to the expectation are weakest at low fields, while all other cells show a more uniform behaviour: the quenches increase as the field is raised beyond 30 MV/m.

### 4.3 Angular distribution

Fig. 4.10 shows the angular distribution of all quench locations, also including BD\_FE limited modes, in bins of  $45^\circ$  but excluding multiple quenches nearby. This results in 121 quench locations. Based on a random occurrence of the quench locations as mentioned earlier, a uniform distribution is assumed, since the magnetic field amplitudes azimuthally along the cavity surface are rotationally symmetric. As mentioned earlier the angular region between  $270^\circ$  and  $90^\circ$  shows more quenches

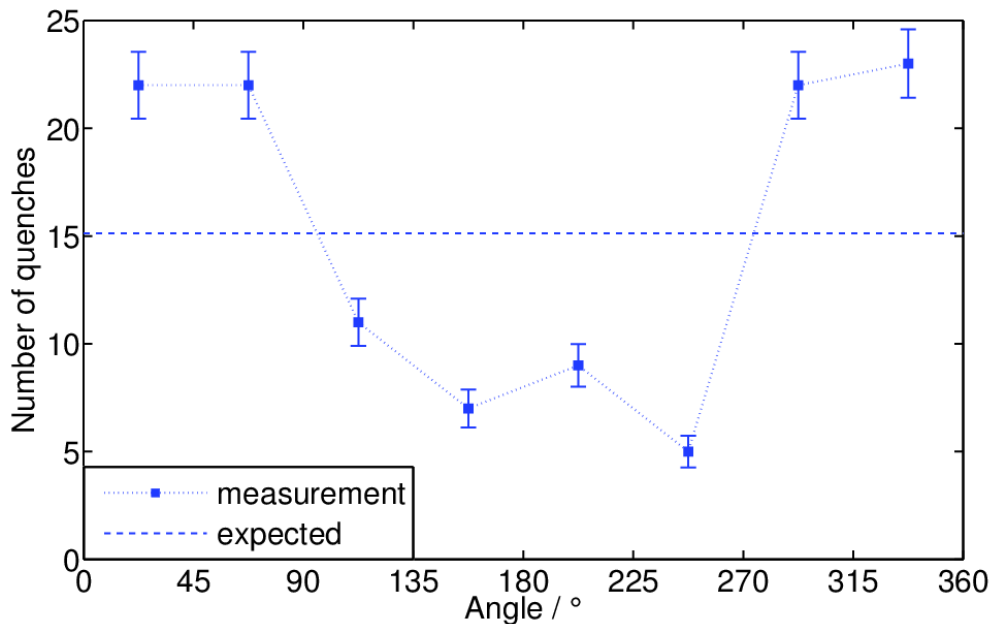


**Figure 4.10:** Angular quench distribution around the cavity. Multiple quenches at the same positions have been filtered out, and a total number of 121 quenches remains, resulting in an average of  $\approx 15$  quenches per bin for a binomial distribution.

than the averaged value of about 15 per bin while on the opposite side much less quenches are observed. Again, the uncertainties are those of a binomial distribution, for reasons explained earlier. The distribution initiated an investigation of dependencies of the quench locations with preparation and assembly steps.

### 4.3.1 Investigation of the shape of the angular distribution

#### Systematic error of the second sound setup

It is important to verify that the second sound measurement technique itself does not introduce a bias. Such biases could be due to varying sensitivity or broken OSTs. About ten cavity tests have been carried out with quench detection using second sound and temperature mapping simultaneously. Although these tests have shown consistent results, all tests carried out with temperature mapping up to three years before the installation of the second sound system have been examined: The quench locations found by the T-map system are given in Fig. 4.11 and show, although with lower statistics (nine tests with defined quench locations), a similar angular distribution. To exclude systematic uncertainties along the z-axis, the data available is not sufficient.

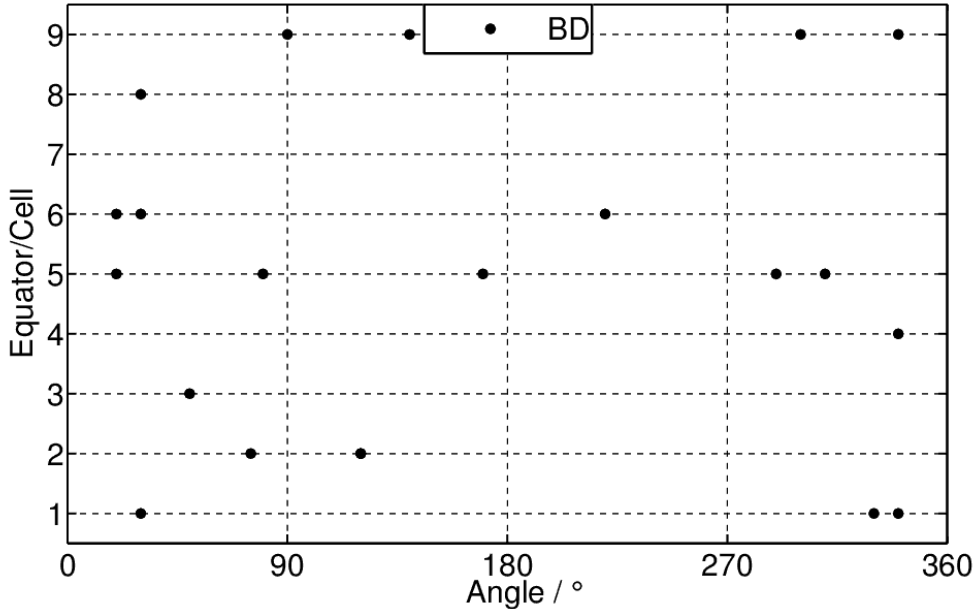


**Figure 4.11:** Distribution of quench locations found by rotating temperature mapping from June 2007 to March 2010. The angular clustering observed with second sound is also found in this diagram.

### Vendor dependent effects

For exclusion of vendor dependent effects, Fig. 4.12 shows the angular distribution of quench locations for both vendors providing cavities at DESY separately. In contrast to the longitudinal distribution discussed in the previous section, there is no obvious indication for one vendor with a significant concentration of quenches in a certain angular range. Both diagrams show an excess of quench locations in the previously discussed range around the power coupler flange, while vendor A exceeds expectation at  $\Phi > 270^\circ$  and vendor B at  $\Phi < 90^\circ$ . There must be other mechanisms at work, or both vendors apply the same production step causing this distinctive feature.

### Horizontal cavity preparation steps

Another possible source of the angular clustering might be found in the preparation steps of the cavities (cf. chapter 2). If preparation steps take place horizontally and with a defined angular orientation - the power coupler flange pointing downwards, they could influence the angular distribution of quench spots. This leads to the hypothesis that any kind of particles, humidity or other contamination on the surface accumulates in the lower half, i.e. in the angular region of the power coupler.

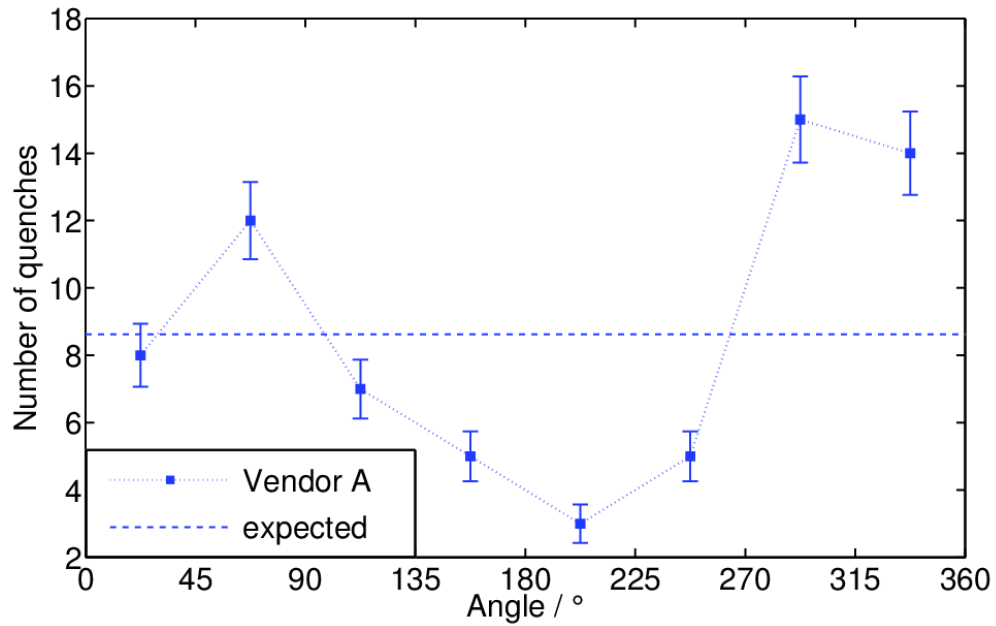
The 800 °C baking for reducing the hydrogen contamination is done in a horizontal furnace, but as the cavity is placed in the furnace with an arbitrary angle, the baking can be excluded as a cause of the observed distribution.

Further preparation proceeding in the clean-room including electropolishing, cavity handling and mounting of the flanges do not have a preferred angular orientation either and can be ruled out as well [116].

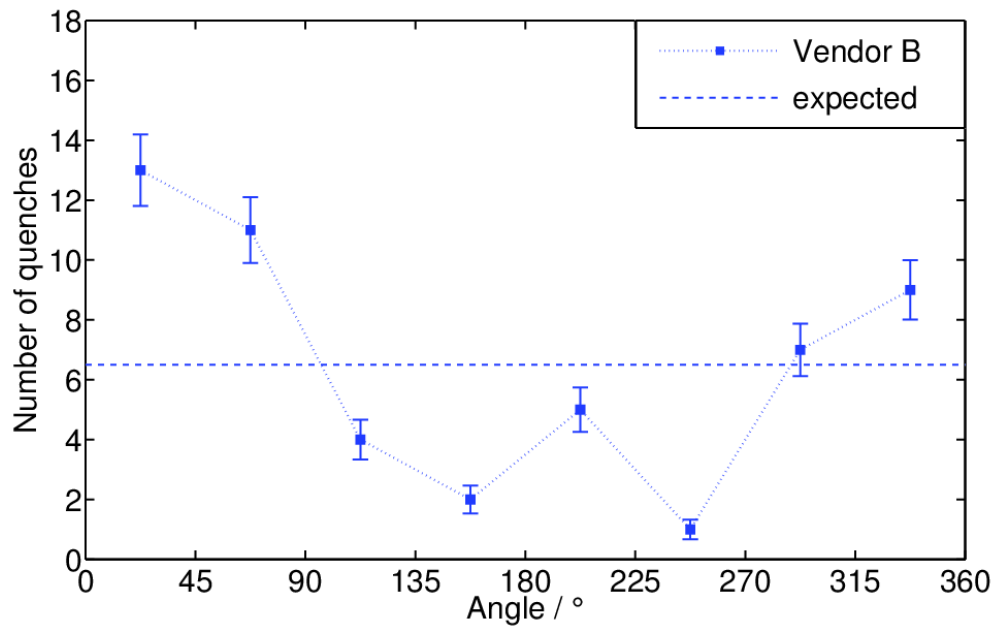
### Inserts and vertical cryostats

Another possibility identified to be the reason for the angular accumulation is found in the vertical cryostats (see Fig. 3.1). The filling of the cryostats with liquid helium with  $T > 2\text{ K}$  is usually done continuously, the filling lines at top and bottom of the cryostat may lead to slightly higher temperatures in the helium bath. This can be excluded, as the superfluid helium has a good thermal conductivity, the bath remains at  $T = 2\text{ K}$  because the heat is distributed fast and the cryostat is pumped continuously [119].

Both cryostats were checked for the helium inlets, and as the angular distribution of the filling lines is symmetric and the orientation of the inserts is always the same, only the lower filling line is in the section  $> 270^\circ$ , but the location is about half a meter below the first cell of the cavity and thereby can be excluded.



(a) Vendor A



(b) Vendor B

**Figure 4.12:** Angular distribution of quench locations for each vendor.



### 4.3.2 Angular distribution per insert

For the vertical tests, four cryostat inserts are in use. Table 4.1 shows the distribution of tests to the inserts and the number of quench locations obtained to explain the values in Fig. 4.13. It shows the total number of tests carried out in each insert. In addition the total number of quench locations acquired in each insert is given. The angular distribution of the quench locations for each insert is shown in Fig. 4.13.

**Table 4.1:** Data underlying for statistics in Fig. 4.13. The number of tests and the number of different quench locations per insert is given.

	Insert 1	Insert 2	Insert 3	Insert 4
number of tests	15	4	5	7
quench locations	58	14	22	27

Inserts 1 and 4 show the same behaviour as the global distribution in Fig. 4.10, so these inserts are checked carefully for magnetisable materials or magnetic fields. The inserts 2 and 3 have very low statistics, so the data cannot be representative.

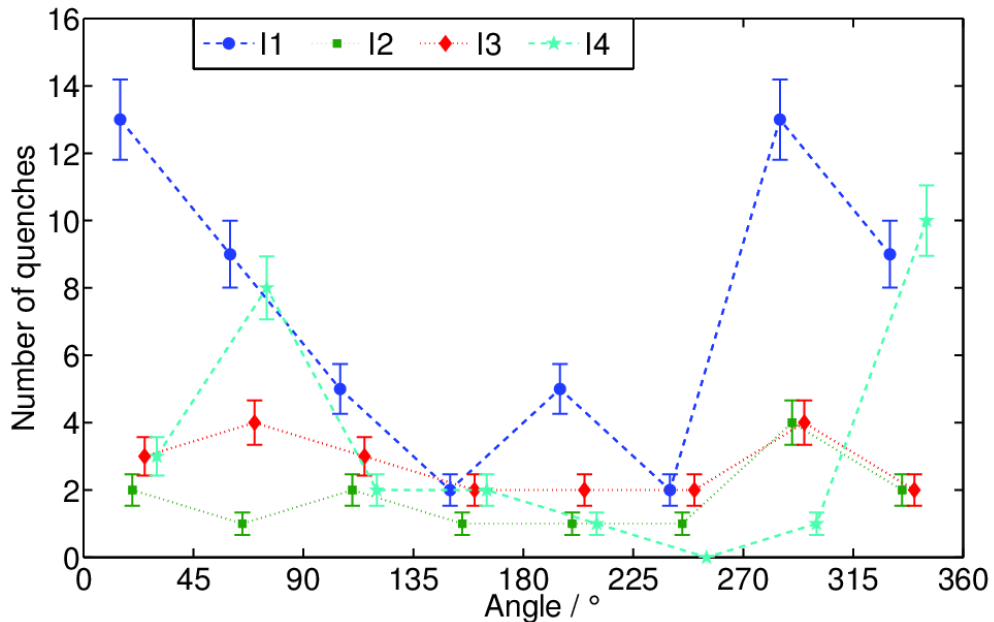


**Figure 4.13:** The angular quench distribution separated for each insert and sorted into bins of  $45^\circ$  width (shifted for better readability) starting from  $0^\circ$ . For inserts 1 and 4 a similar excess as in Fig. 4.10 is seen, for inserts 2 and 3 statistics is too low (see text).

### Magnetisation of cryostat inserts

All material close to the cavity in the vertical test has to be non-magnetisable to avoid freeze-out of magnetic flux in the niobium during cooldown (cf. chapter 3), resulting in lower quality factors and thus higher surface resistance (e.g. [22]). If a magnetic field is applied locally, it may result in earlier thermal breakdown in this area because the generation of heat by the surface magnetic field increases.

Insert 1 at the DESY cryogenic test stand includes a waveguide all along and close to the cavity right in the suspicious angular area. This waveguide has been tested for permeability. The measurement at several locations on the waveguide showed a relative permeability of  $\mu < 1.01$ , so it can be excluded as a source for a magnetic field.

Magnetic field gradient measurements with a fluxgate magnetometer showed a small magnetic field at the surface of a fixture part (so-called *horseshoe*) for the cavity in each vertical insert of some  $\mu\text{T}$  in the preparation area. This part is about 20 cm away from cell 1 of the cavity, the magnetometer has been placed close to the equator of the cell, and the fully equipped insert was placed in the cryostat to shield the earth magnetic field. The field components of the magnetic field measured at  $\Phi = 315^\circ$  and  $45^\circ$  at equator 1 were measured horizontally and vertically and did not exceed  $H = 0.04 \mu\text{T}$ . So a rough estimation for the absolute value of the magnetic field exposure at cell 1 of  $H_{est.} = 0.1 \mu\text{T}$  is feasible. Assuming that only cell 1 is affected by this magnetic field, with (1.7) and only taking 1/9 of the cavity surface into account, the additional resistance in this cell yields  $R_H(\text{cell 1}) \approx 0.12 \text{ n}\Omega$ , which is about 1% of the overall surface resistance and heat loss (see next chapter). For the empty cryostat the highest magnetic field was measured at an overlap of two magnetic shields with  $H < 0.5 \mu\text{T}$ . All other measurements gave negligible results. Assuming again an affection of only one cell, this accounts to  $R_H < 0.6 \text{ n}\Omega$ , which affects about the total surface resistance with an increase of about 5%. Again: this does not explain the angular behaviour or the cell distribution of the quench locations, since the z-position of the location with increased field is approximately where the upper third of the 9-cell cavities is placed in the cryostat. So only cells 7 to 9 should be affected, which were inconspicuous in this examination.

## 4.4 Correlations with surface inspection

Besides the global observation and exclusion of sources for the quench, the inspection of the inner surface can give evidence for irregularities causing thermal breakdown. Nevertheless, only few quenches can be correlated with features observed. Only two recently published [65, 98] examples will be explained briefly in the following paragraphs - more examples and more detailed analysis can be found in [105, 120].

### 4.4.1 Cavity Z161

Cavity Z161 has been produced to qualify a new process technology for equator welding. The vertical test showed poor results of  $E_{acc} = 13.6 \text{ MV/m}$  limited by thermal breakdown. The determination of the quench locations has been carried out

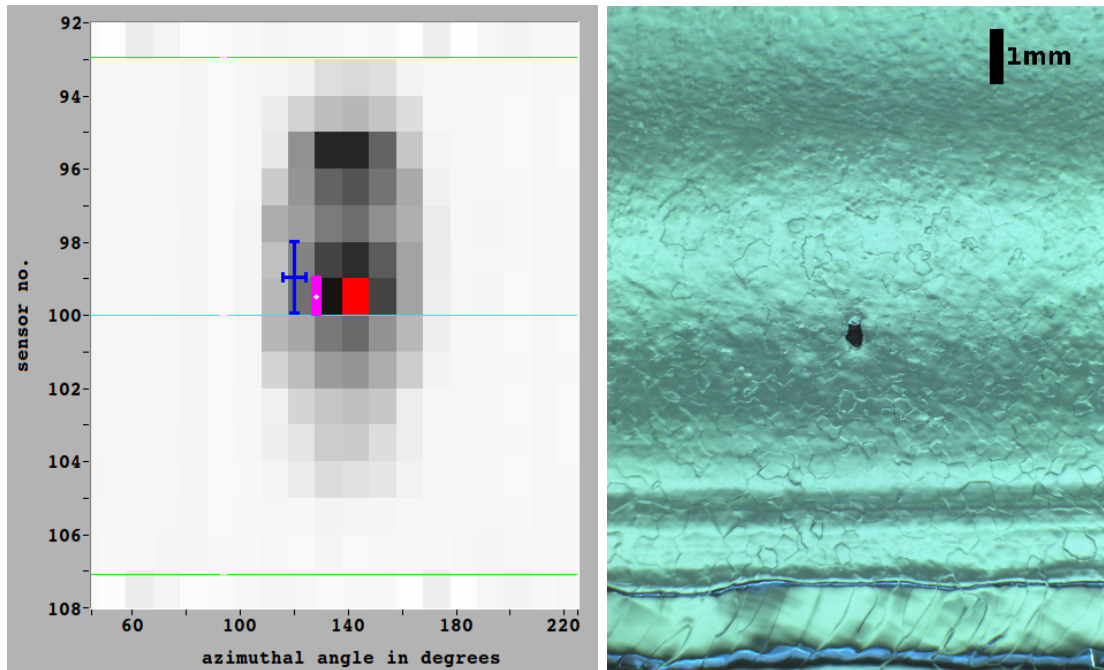


**Figure 4.14:** Correlation between T-Map, quench localisation by second sound and optical inspection for cavity Z161 [65]. Left: T-map of cell 2, the cyan coloured line indicates the equator position, the green lines are the irides. The greyscale indicates the temperature (dark = warm) and the red spot indicates the hot spot found by T-map, the blue point including the errorbars shows the quench location determined by second sound. Pink shows the area where the picture on the right was taken. Right: Picture at the determined quench location.

simultaneously with the rotating T-map system and second sound and the results are shown in Fig. 4.14 on the left. Optical inspection of the quenching area showed a black spot (Fig. 4.14 on the right). Several of these spots were found all along the cavity, and were also the cause for other quench locations in other passband modes. For further investigation the cavity was dissected and the black spots found in the cavity were examined for foreign material. It was found that these spots were aluminium flakes, reflecting much less light than the shiny niobium surface and appear to be 'black' in the optical inspection. The heat generated by the normal conducting aluminium during the application of rf field could be dissipated by the superconducting niobium up to a certain level, the quench limit.

#### 4.4.2 Cavity AC126

The accelerating field of cavity AC126 never exceeded  $E_{\text{acc}} = 21 \text{ MV/m}$ , although additional etching and several high pressure rinsing cycles were applied. For quench localisation the rotating T-map system and second sound was used. Both systems agreed on the position shown in Fig. 4.15. The optical inspection showed a rainbow

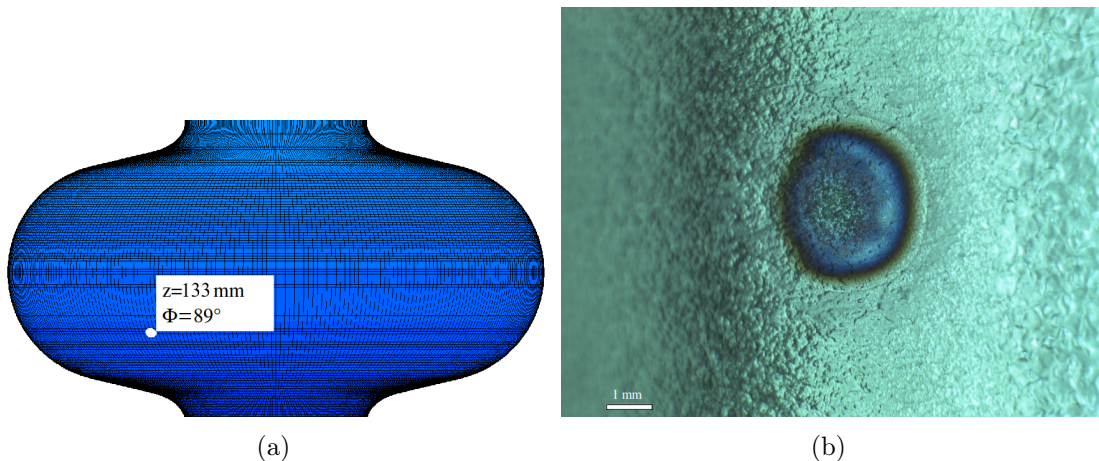


**Figure 4.15:** Correlation between second sound and optical inspection at cavity AC126 [98]. Left: Magnification of cell 2 in the second sound quench localisation software. The red spot indicates the quench location. The  $z$ - and  $\Phi$ -position is given according to Fig. 4.1. Right: Picture at the determined quench location (see text).

coloured spot at the quench location, which is evidence for  $\text{Nb}_2\text{O}_5$ . Further inspection revealed 7 more of those spots, and the distribution of these spots lead to the conclusion that the motors for moving the cavity in the high pressure rinsing system had an interruption during the rinse of AC126. As the movement of the cavity was stopped, the niobium surface was exposed to the high pressure water jet for an undefined long time, and the spots match perfectly the nozzle and spray pattern of the high pressure rinsing system. The extensive exposure of niobium to a high pressure water jet generates niobium oxides [121] with a higher surface resistance [122] which eventually results in thermal breakdown during the rf test.

#### 4.4.3 Equator weld overlap

The cavities are assembled by electron beam welding, as mentioned in chapter 2. The electron beam cannot be switched on at full current at once, so the current has to be increased at the beginning and decreased at the end. This results in an 'overlap' of the welding seam, since the beam has to penetrate all the bulk niobium at the edge.

The area at the weld overlap is of interest since this angular range of about  $30^\circ$  is heated twice, during fade in and fade out of the electron beam, at the welding

process. This may cause additional irregularities due to improper resolidification and inclusions of foreign material (especially gases). Thus a higher probability for thermal breakdown occurs in this region.

For 15 cavities which have been tested with quench localisation, pictures of the inner surface without surface treatment are available: it is possible to find the locations of the overlap of the equator weld (see section 2.1). An example is shown in Fig. 4.16.

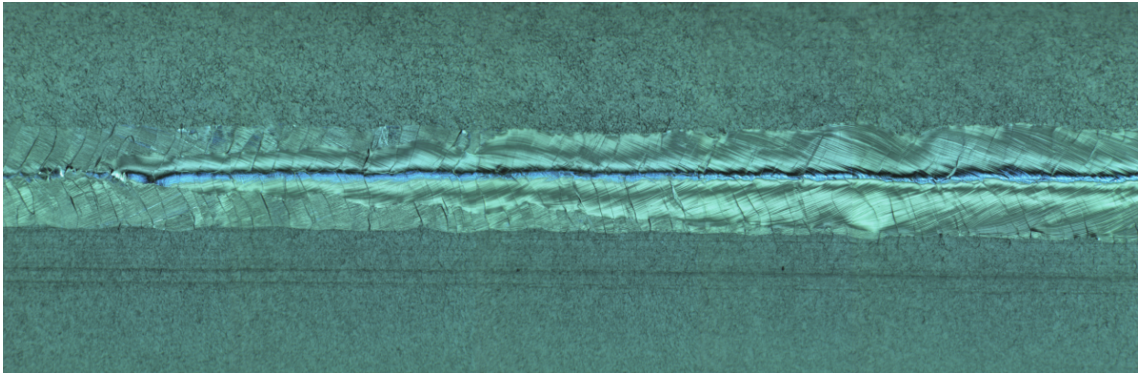


**Figure 4.16:** Picture of a welding seam overlap, taken of cell 1 at Z160. The welding seam is about 3 mm wide and the angle shown is about  $20^\circ$ , which is the visible part of the overlap at ramp down (the weld 'fades out' from right to the left) of the electron beam [107].

From 51 unique quench locations, only five are located at the weld overlap within uncertainty. The whole overlap region - as stated before - includes an angle of  $30^\circ$ , which yields an expectation value of 4-5 quenches for these 51 locations obtained, so the overlap region does not feature a special quench behaviour compared to the overall sample.

A suspicion that an identical welding pattern at vendor B is the reason for the noticeable number of quenches in cell 1 has not been confirmed: If the weld overlap in cell 1 would be always at the same angle, this might be evidence for a systematic issue in the welding process of the end-cells. But a check on several cavities of vendor B did not confirm this suspicion as the overlap has been found to be at random angles.

## 4.5 Summary

The quench localisation using second sound is a fast and powerful tool. It is possible to determine the quench locations of the cavities with very little effort. After implementation at DESY in the course of this work, the method is applied as a standard procedure during measurement cycles of cavities without attached helium vessel, and the large number of tests allows statistic statements.

In 31 cavity tests 189 quenches occurred in total, resulting in 121 different quench locations, including quenches with field emission. At a first glance, two different features were found: an accumulation of quench locations in cells 1 and 2, which are the bottom cells in vertical tests. And, second, about 70% of the quench locations are located in the angular range between  $270^\circ$  and  $90^\circ$ . Most of the found quenches were, as expected, in the high surface magnetic field region of the cavity, but not necessarily directly at the equator.

As two vendors provide cavities for DESY and the European XFEL, the data has been split up to investigate for vendor dependent effects. Cavities of both vendors exhibit a similar behaviour at cell 2, while it was possible to attribute an excess of quenches in cell 1 to one of both vendors. A suspicion for the reason is the assembly of the end-cells, as the mounting of the end-group containing the power coupler flange and the HOM coupler antenna can cause difficulties. In addition, both vendors show a similar angular distribution and there seems to be no vendor dependence for the angular excess.

For the angular dependence described before, no reason was found so far. The suspicion that a special angular orientation during horizontal storage and treatment causes contamination of the surface could not be verified: A special orientation of the cavity with the power coupler flange at  $\Phi = 0^\circ$  pointing downwards during cavity preparation and cleanroom assembly has not been found. In addition, the magnetic shielding in the vertical test cryostats has been measured to rule out the freeze-out of magnetic flux in the cavities resulting in higher surface resistances causing quenches in special angular regions. All cavity inserts have been examined for magnetised materials in this context, but the magnetisation was either negligible or in an unsuspecting region.

The quench fields achieved in the cells suffering from thermal breakdown vary from about 10 MV/m up to 50 MV/m. Again, the previously discussed cells 1 and 2 show a special behaviour: most of the quenches occur at fields below 30 MV/m, but no explanation for this feature has been found. For all other cells, most of the quenches were measured at accelerating fields beyond 30 MV/m, so it is important to understand the quenches in the 'lower' cells in future cavities, if the quench fields are similar.

## CHAPTER 5

# Quality factor analysis

---

The unloaded quality factor  $Q_0$  of superconducting cavities is important regarding the heat dissipation of the cavity into the surrounding helium bath. The loaded quality factor  $Q_l$  has already been introduced in section 3.2. It describes the ability to accept and to store the energy in the cavity, including all losses at the coupling antennas. For accelerators it is usually two to three orders of magnitude lower than  $Q_0$ , as it is mandatory to be able to fill the cavity with energy very fast to provide the same power for each particle bunch. The energy losses in the cavity are unaffected by the lowered  $Q_l$ .

For both pulsed and cw accelerators the  $Q_0$  is very important, as it is a measure for the power dissipation into the helium bath. It is directly related to the surface resistance and hence the dissipated heat of superconducting cavities via  $P_{\text{diss}} \propto R_s^2 \propto Q_0^{-2}$  as has been explained in section 1.3. It is favourable to reduce the cryogenic heat load as much as possible to either reduce the cryoplant cost or to allow higher accelerating fields - both require the highest achievable  $Q_0$ .

Comparison of averaged quality factors and variations for cavities made of different niobium ingots, surface treatments and niobium grain sizes are made in section 5.2. Furthermore this allows general statements for large scale productions of cavities for accelerators. While the BCS resistance  $R_{\text{BCS}}$  and some contributions to the residual resistance  $R_{\text{res}}$  are understood, loss mechanisms related to the amplitude of the rf field are still under discussion and data obtained at DESY will be discussed in section 5.3. Here, a recently developed model for the global behaviour of the surface resistance for superconducting cavities including different frequencies, shapes and operating temperatures [40] is applied on datasets obtained at DESY for 1.3 GHz 9-cell cavities.

As a large database of cavity measurements is available at DESY [25], using this data allows global observations by using recent cavities with state-of-the-art fabrication.

## 5.1 Data sample

To take latest results, only cavities starting from AC112 are taken into account, but special cavities (Z145, Z163, Z164: hydroformed 3-cell units; Z160-Z162: qualification of a new equator welding technique) are excluded for the analysis in section 5.2. Cavities AC112-AC114 and AC151-AC158 are made of large grain niobium [24], while the rest are made of fine grain material. All cavities have been heated in a vacuum furnace to degas the hydrogen out of the niobium surface and have been treated either with BCP, EP or EP+. All measurements have been carried out in  $\pi$ -mode at a helium bath temperature of  $T = 2$  K. To avoid the influence of multipacting on the Q vs. E curve, the data is only eligible after processing in the  $\pi$ -mode and - if carried out - mode measurements.

The abundance of field emission has been restricted to a measured radiation of  $10^{-4}$  mGy/min on the cryostat lid, which has been found empirically to leave the quality factor unaffected within the measurement uncertainties. While the Q vs. E datasets for section 5.2 are - if applicable - only used up to this threshold, any dataset exhibiting radiation is skipped completely for section 5.3.

A detailed listing of the data and thresholds used for this chapter is given in appendix B.2.

## 5.2 Average quality factors of cavities

The comparison of different surface treatments, large grain and fine grain niobium and the purity of the material (RRR) is carried out by averaging the quality factors of the respective data sample and showing the uncertainties within a standard deviation of  $\sigma = \sqrt{\frac{1}{n-1} \sum_{i=1}^n (Q_0 - \langle Q_0 \rangle)^2}$ . As the standard cavity measurement does not take data points at particular accelerating fields, usually no data point at the exact value of the 5 MV/m steps has been measured. Thus the neighbouring points were used for a linear interpolation to obtain an approximate quality factor for the field required. In addition, the restrictions for field emission as mentioned before apply, which usually results in a smaller data sample for higher accelerating fields. For better readability, the data depicted in the plots are slightly shifted around the related value and to indicate the trend of the quality factors, the data points are connected with lines.

### 5.2.1 $Q_0$ dependence on surface treatments

A direct comparative quality factor analysis for all surface treatments applied at DESY is possible for the cavities fabricated of large grain material, since the sequence of surface treatments and corresponding tests have been chosen for that reason:

All eleven cavities had a BCP surface treatment with subsequent vertical test. To compare between BCP and EP surface, all cavities got an additional EP treatment



to obtain a 'new' EP surface, followed by another vertical test. Due to disassembly, tank welding and reassembly of flanges and antennas, four cavities received an EP+ treatment. As shown in Fig. 5.1, the difference of cavity quality factors for

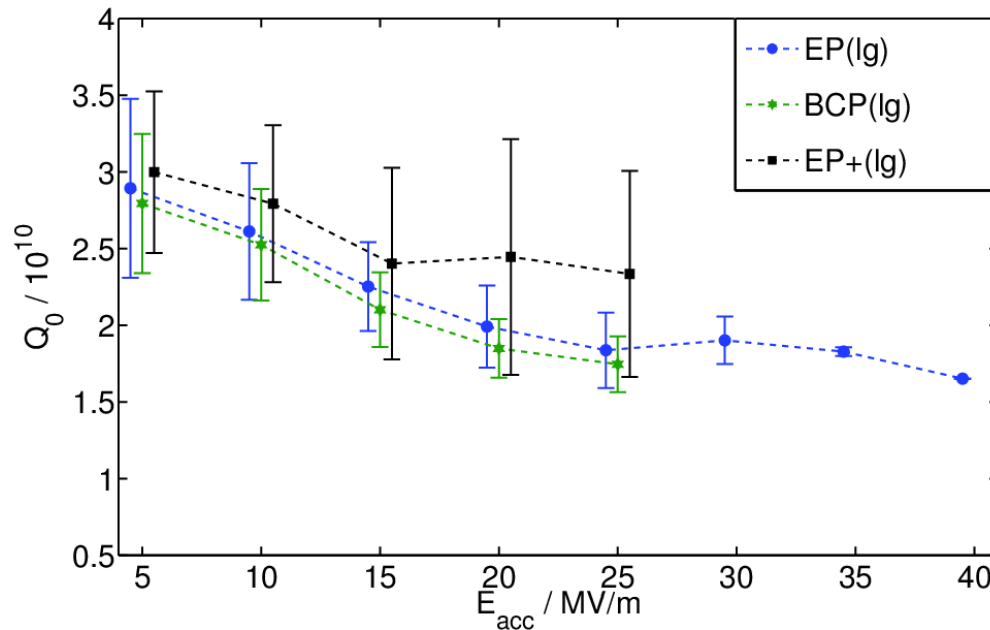


**Figure 5.1:** Averaged quality factors for different accelerating fields of eleven large grain cavities with different surface treatments. All treatments yield similar quality factors, for EP+ only four cavities were available and one cavity measurement yields a very high  $Q_0 > 3 \times 10^{10}$  up to 20 MV/m.

BCP and EP surface is almost negligible. The slope in  $Q_0$  is almost the same up to  $E_{acc} \leq 15$  MV/m, but a small offset of  $\Delta Q_0 \leq 10^9$  applies, which is within uncertainty but may account for the different surface properties, as EP leaves a smoother surface (see section 2.2 and [56]). In addition, it is visible that BCP treated cavities do not reach fields higher than 30 MV/m. The EP+ data yields a higher quality factor which has to be attributed to one out of the four cavity tests. Cavity AC157 showed a much higher  $Q_0$  than expected, which has been explained with a high coupling factor  $\beta > 10$  (see section 3.2 and [22]) yielding a lower external quality factor and an overestimation of  $Q_0$  [123]. If this dataset is subtracted, the EP+ values are also in very good agreement with the BCP and EP data.

The range from 20-25 MV/m shows no significant change for BCP and EP cavities, the small offset in  $Q_0$  persists, for EP+ only two cavities are included, which explains the increasing offset. Overall, if the cavities do not suffer from field emission,  $Q_0$  is always above  $1.6 \times 10^{10}$ , which is a promising result for further cavities being assembled from large grain material and state-of-the-art treatment.

For cavities made of fine grain material, only electropolished and EP+ cavity tests

are available in a sufficient number: 19 EP surfaces and 18 EP+ surfaces. In contrast to the large grain cavities, where the cavity sample is the same for all treatments, only six fine grain cavities were tested with both surface treatments. Thus the comparison in Fig. 5.2 only allows statements related to the surface treatments, since only few cavities are contained in both datasets.

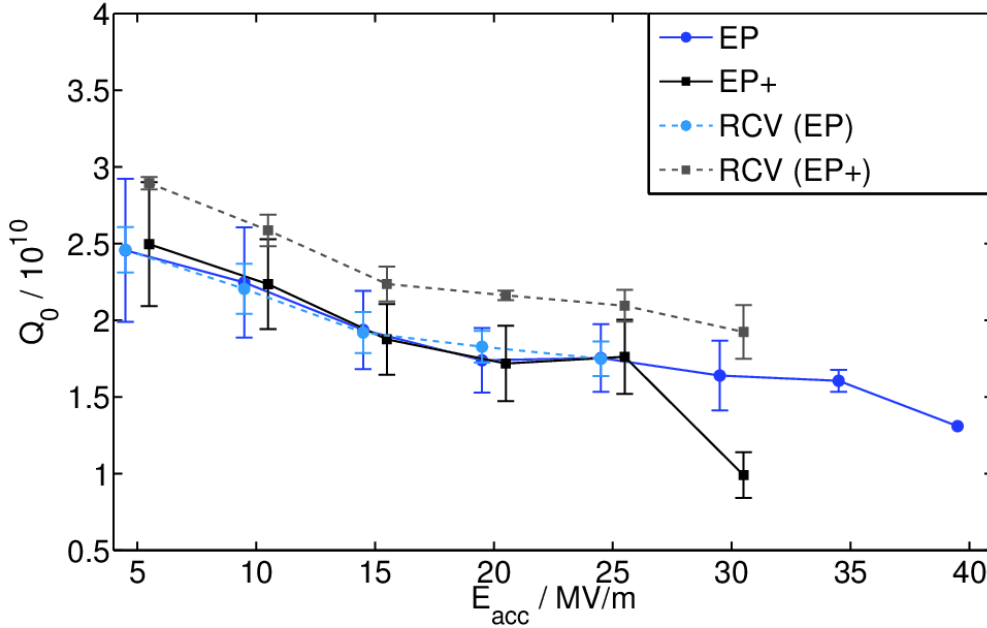


**Figure 5.2:** Averaged quality factors for different accelerating fields for fine grain cavities sorted by surface treatment. Although the data samples do not include all the same cavities, it is obvious that EP+ does not affect the quality factor negatively. The dashed lines show the reference cavities (RCV) of the industrial cavity production for the European XFEL, which meet the quality factors of the earlier cavities within uncertainties.

There is almost no difference in  $Q_0$  for the surface treatments up to  $E_{acc} = 25$  MV/m, although the tests available at this accelerating field reduce to 5/4 cavities (EP/EP+) due to field emission. The drop of the quality factor at 30 MV/m for the EP+ cavities can be accounted to the only two cavities remaining at this field: AC128 and AC129 got the full treatment, including 800°C firing and 120°C baking. They show no field emission and yet exhibit a strong reduction in the quality factor, which lacks of an explanation.

The first pre-series cavities, so-called reference cavities (RCVs), assembled by the cavity vendors for the European XFEL series production have been treated at DESY according to the treatments planned at the vendors' facilities. At a first glance, a slightly higher quality factor for cavities for EP+ is seen, but nevertheless, statistics is limited and measurement errors itself have not been taken into account. The values obtained are within uncertainty of the previously discussed EP+ cavity sample. The EP RCVs match the curve for EP treated cavities perfectly. One of the EP+ RCVs

exhibits some field emission above 15 MV/m, but the overall conclusion for the RCVs is, that the cavities exceed the specified quality factor of  $Q_0(23.6 \text{ MV/m}) > 10^{10}$  given in the technical design report for the European XFEL easily [18].

### 5.2.2 Large grain and fine grain material

Large grain cavities have several advantages regarding the quality factor and heat dissipation: The surface is much smoother after surface treatment and less grain boundaries contribute to the surface resistance [62]. For easier comparison, the EP data of the previous figures for large and fine grain material is combined in Fig. 5.3.

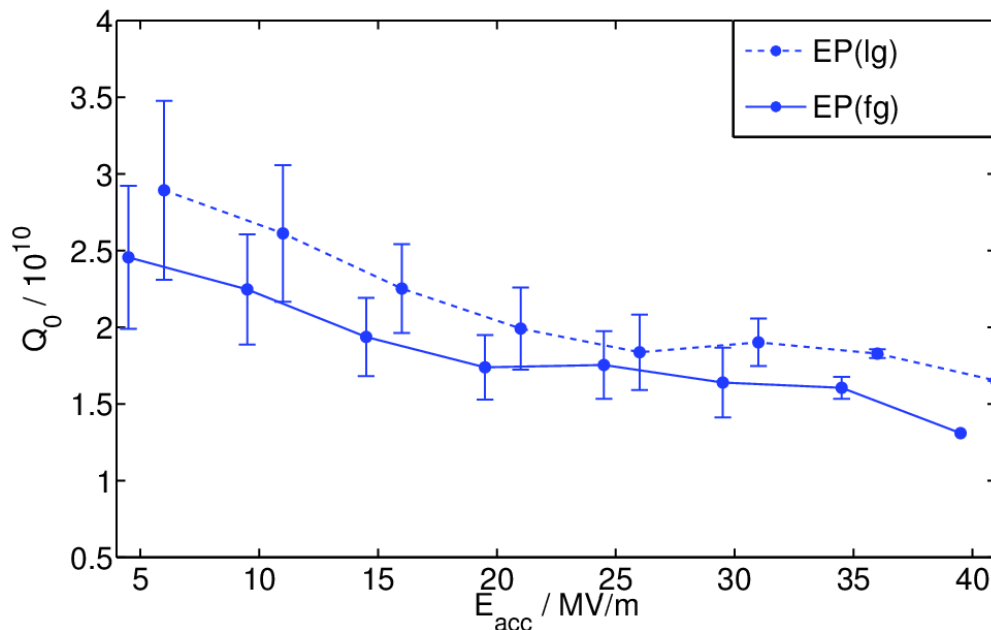


**Figure 5.3:** Quality factors of cavities made of large grain material compared to fine grain material.

It is obvious, that the cavities made of large grain material yield higher quality factors than fine grain cavities. The difference in surface resistance is about  $2 \text{ n}\Omega$  ( $\approx 20\%$ ) (apply (1.4)), which results in a reduction of dissipated heat of about  $1/6$  for the large grain cavities, due to a reduced overall length of grain boundaries. The cavities for large scale production are still made of fine grain material since the niobium vendors cannot produce a sufficient amount of large grain material up to now, and the assembly of those cavities is difficult [124].

### 5.2.3 Influence of RRR on the quality factor

A comparison of different niobium ingots is possible by using the eleven large grain cavities, as these were fabricated of three different ingots with different RRR:

- RRR(AC112-114)=505
- RRR(AC151-153)=406-438
- RRR(AC154-158)=340-355

Note that the RRR specified was measured for the single niobium sheets, so changes of RRR due to forming, welding and treatment are not taken into account. The quality factors of the cavities, separated by ingots and surface treatment are given in Fig. 5.4. The cavities made from lower RRR material yield higher quality factors

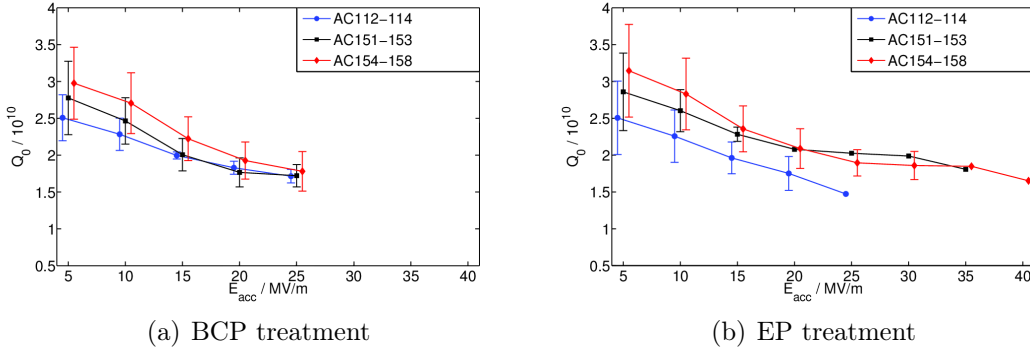


**Figure 5.4:** Comparison of quality factors for cavities made of different niobium ingots with varying RRR.

due to lower  $R_{BCS}$ , which complies with calculations and previous measurements [30]. Although a complete change of the surface (from BCP surface to clean EP surface) took place, the sequence of the quality factors compared to the sheet RRR remains the same up to 20 MV/m, there is no major variation of RRR due to the surface treatments. Above this threshold, other loss mechanisms are dominant, which will be discussed in the following section.

## 5.3 Surface resistance model

The behaviour of the quality factor and accordingly the surface resistance cannot be explained with the simple combination of the surface temperature dependent BCS resistance  $R_{BCS}$  and a constant term  $R_{res}$ , as shown in Fig. 1.8. There are field dependent mechanisms at work, which have been explained in [40] and also summarized in section 1.3.3.

The quality factor  $Q_0$  can be converted to the surface resistance  $R_s$  with (1.4),  $R_s = G/Q_0$ . With the simplified model introduced in section 1.3.3, the quality factor data of cavity AC158 shown in Fig. 1.8 has been fit to

$$R_s(E_{\text{acc}}) = \widetilde{R}_2 + \frac{b}{E_{\text{acc}}^2} + R_1 \left( \frac{1}{2} \left( \frac{E_{\text{acc}}}{E_c} \right)^2 + \frac{a^2}{3} \left( \frac{E_{\text{acc}}}{E_c} \right)^4 \right) \quad (5.1)$$

with

$$\widetilde{R}_2 = R_2 \left( 1 + \left( \frac{E_{\text{acc}}}{E_0} \right)^2 \right) \quad (5.2)$$

as 'field dependent' BCS resistance. It has been calculated with the use of the thermal feedback model introduced in section 1.3.3 with RRR=300 and a helium bath temperature of 2 K. Residual resistance is neglected. Parameter  $E_0 = 56.4$  MV/m has been obtained by fitting the data of the thermal feedback calculation in Fig. 1.8. To allow mathematical modelling of single tests of 9-cell 1.3 GHz cavities carried out at DESY, the following simplifications in (5.1) were made. These do not affect the results negatively as shown in the following discussion of the parameters, thus are justified.

- convert the surface peak magnetic field  $B$  to the accelerating field  $E_{\text{acc}}$  by using the conversion factor  $c_f = 4.26 \times 10^{-3} \frac{\text{T}}{\text{MV/m}}$ , as explained in section 1.3.1
- define  $\widetilde{R}_2(E_{\text{acc}})$  as the sum of the contributions of  $R_{\text{res}2}$ ,  $R_{\text{res}}(\omega)$ ,  $R_{\text{s,BCS}}(\omega, T)$  by approximating the BCS resistance by a thermal feedback model calculation and creating a relation  $E_{\text{acc}}(T)$  (see (5.2))
- absorb  $R_{\text{res}1}$  and  $R_{\text{s,fdt}}$  in parameter  $R_1$
- set  $a = \kappa = 0$ , as recalculation of (1.12) shows that  $\kappa$  is only included in the second order of the expansion and only contributes at very high fields [125], which are only achieved for AC158, although  $\kappa$  is expected to be in the order of 1 for niobium.

For the following discussion, the measurement uncertainties of Table 3.1 are taken into account and depicted as errorbars in the subsequent surface resistance plots.

The surface resistance data and the fit to (5.1) is shown in Fig. 5.5. The data are described well by the model, except in the mid-field region from  $E_{\text{acc}} \approx 10$  to 20 MV/m, which also results in overestimating the surface resistance in the low field region around  $E_{\text{acc}} \approx 5$  MV/m. Another example for a good global description of the data by the model is shown in Fig. 5.6. The fit parameters obtained for the previous examples are given in Table 5.1. Fit parameter  $a = \kappa$  is the Ginzburg-Landau

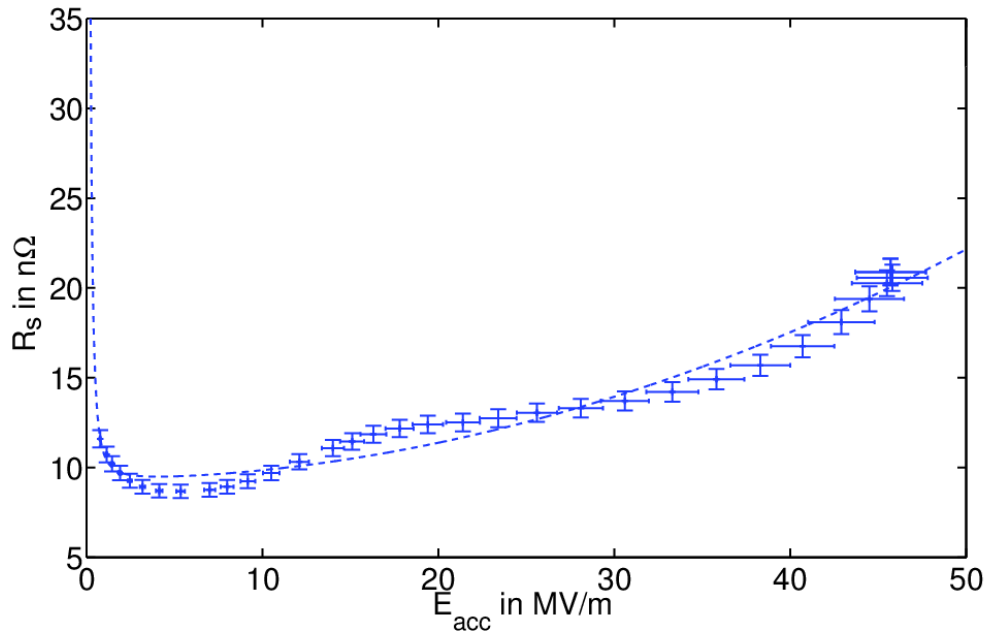


**Figure 5.5:** Calculation of the surface resistance and data fit to (5.1) for cavity AC158. The underlying data is well described by the model, but in the mid-field region from  $E_{acc} \approx 10 - 20$  MV/m the resistance exceeds the modelling fit.

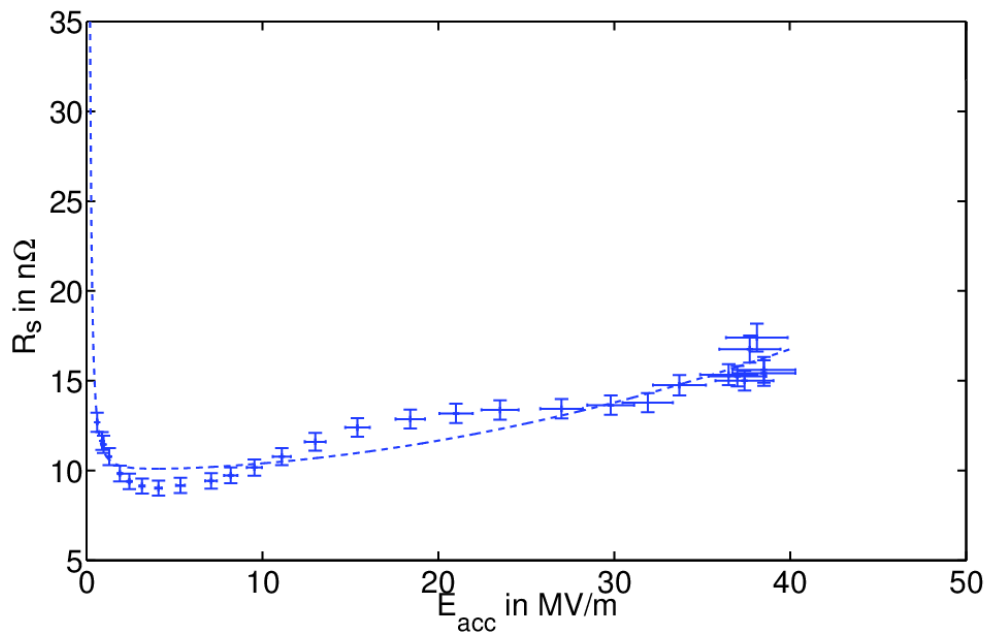


**Figure 5.6:** The data of cavity AC153 with electropolished surface shows a similar behaviour to AC158 in the mid-field region and the same overestimation at low fields, although it reaches only about  $E_{acc} = 38$  MV/m in total.

**Table 5.1:** Parameters of the fits obtained from cavities AC158 and AC153.

cavity	$R_2/n\Omega$	$R_1/n\Omega$	$a$	$b/n\Omega(\frac{MV}{m})^2$
AC158	$9.3 \pm 0.4$	$8.7 \pm 1.8$	$0.5 \pm 1.4$	$1.41 \pm 0.89$
AC153	$10.0 \pm 0.5$	$4.4 \pm 2.8$	$\approx 0$	$1.05 \pm 0.60$

parameter, which should be  $\kappa \approx 1$  for niobium. The only cavity which yields a satisfying result for  $a$  is cavity AC158 with  $a = \kappa = 0.5 \pm 1.4$ , and even here the error is large. This is due to the fact, that (5.1) contains an expansion of a logarithm (see [40]), and  $a$  appears first in the second order, which requires high fields close to the critical magnetic field  $B_c$  [125] and the critical electric field  $E_c$  respectively. A first tentative fit of all data sets always showed unstable fit results with  $a < 10^{-3}$ , except for cavity AC158, and large uncertainties.

The behaviour of the surface resistance in the mid-field range from 10 to 20 MV/m may cause a reduction of the accuracy of the fit. Thus it does not represent the shape of the data in the high-field regime perfectly, as already can be seen in the previous examples. The 'step' in the mid-field range is a phenomenon in all cavity tests, as will be discussed in section 5.3.2 and is also visible in the averaged values from the previous section (cf. Figs. 5.1 and 5.2, for example), albeit smoothed due to the averaging.

For the following discussion of the complete dataset of the other fit parameters, the parameter  $a$  is set to  $a = 0$ , for reasons explained above.

### 5.3.1 Fit parameters for 21 cavity tests

Applying the restrictions described in the introduction of this chapter, a selection of 21  $Q_0$  vs.  $E_{acc}$  curves acquired in vertical cavity tests have been investigated by applying the surface resistance model. Some datasets showed an outlying calibration point of the measurement software which has been excluded from the fit. The parameters  $R_2$ ,  $R_1$  and  $b$  will be discussed in relation to the maximum accelerating field  $E_{acc}$  achieved in each test, and the uncertainties given are the fit uncertainties for a 95% confidence level.

#### Parameter $R_2$

The fit parameter  $R_2 = R_{BCS} + R_{res}$  is used as constant, as the temperature dependence of  $R_{BCS}$  has been modelled in (5.2) as field dependence, with a constant  $R_2$ . It indicates the minimum of the surface resistance at low fields, assuming only small field dependent contributions within uncertainty apply. Fig. 5.7 shows the values obtained for all datasets. For accelerating fields of about 5 MV/m the surface resistance reaches a global minimum for all 1.3 GHz 9-cell cavities tested. As stated before, the minimum value is closest to  $R_{BCS} + R_{res}$ , where the expected surface resistance values are in the range from 9 to 14 n $\Omega$  for unloaded quality factors of

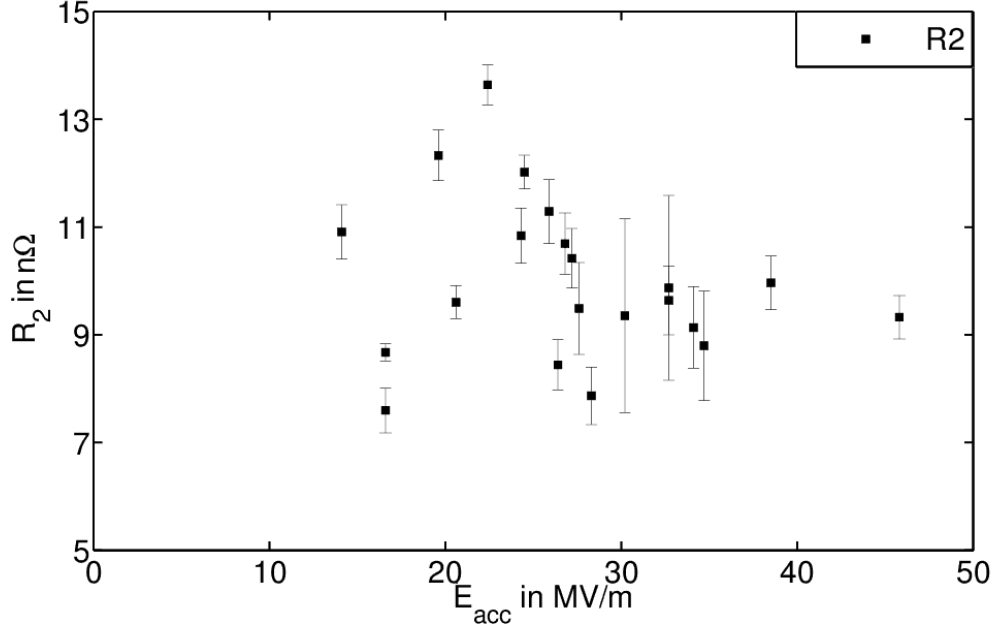


**Figure 5.7:** The fit parameter  $R_2$  related to the accelerating field limit varies from 7 – 14 nΩ which fits perfectly in the expected range.

2 to  $3 \times 10^{10}$  at  $T = 2\text{ K}$ . The variation of  $R_2$  from 8 – 14 nΩ is in very good agreement with the expected values of  $R_s$  at the low fields mentioned.

### Parameter $R_1$

Parameter  $R_1$  indicates the slope of  $R_s$  towards higher accelerating fields (see (5.1)). It describes small normal conducting defects, small enough to be penetrated by the superconducting current, like grain boundaries. As mentioned in the simplifications at the beginning of this section, it already absorbs the percolation term (1.11) in contrary to [40]. The values shown in Fig. 5.8 feature a special behaviour for cavities achieving only limiting fields below  $E_{\text{acc}} = 20\text{ MV/m}$ : The lower the limitation, the higher the parameter  $R_1$ . Cavities with higher limitations show values below 40 nΩ, which is in agreement with [40] stating a value for  $R_{\text{res}1} = 25\text{ nΩ}$ , keeping in mind that the contribution due to percolation has to be added, if applicable.

The values in the order of  $R_1 \approx 100\text{ nΩ}$  at low limiting fields are explainable with a fit example of cavity AC114 shown in Fig. 5.9. In comparison to Figs. 5.5 and 5.6 the fitting curve is not bent to higher fields with (still) rather low surface resistances. The mathematical explanation for this feature is that  $R_1$  defines the slope of the parabola towards high accelerating fields. Thus the calculated  $R_1$  for cavities with low accelerating field limit do not represent the expected behaviour of the surface resistance if higher accelerating fields are reached.



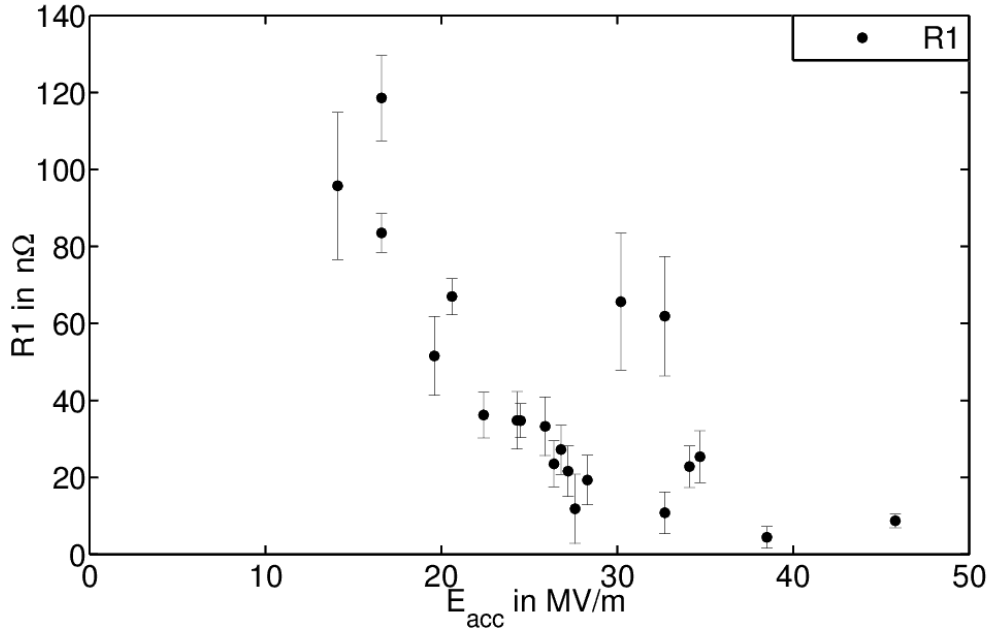


**Figure 5.8:** The fit parameter  $R_1$  in relation to the limiting accelerating field. It is very high at low fields and saturates at fields above 20 MV/m at values below 40 nΩ.

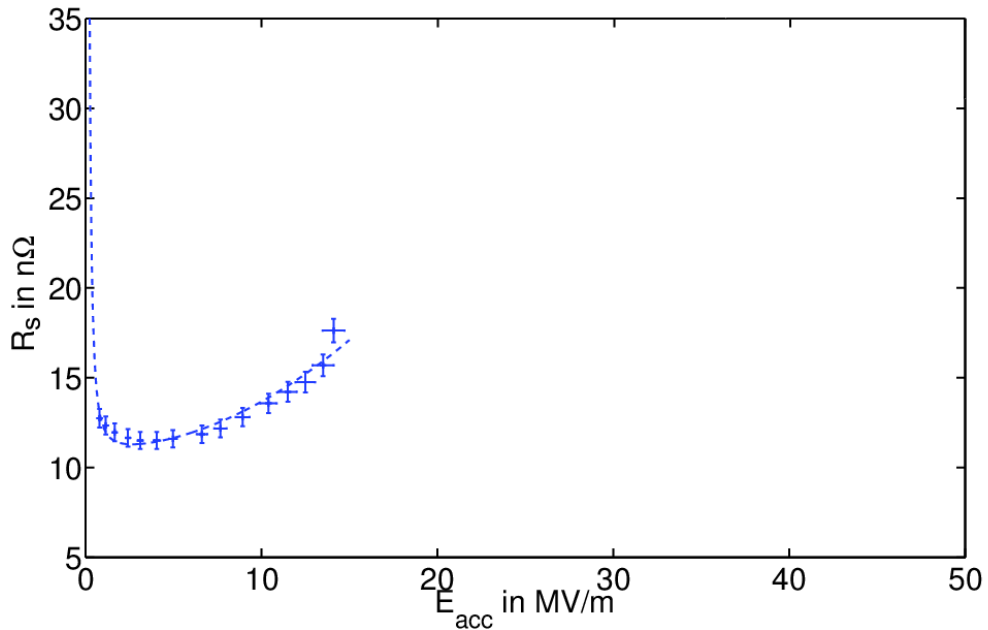


**Figure 5.9:** The fit at cavity AC114 matches perfectly, but the value of parameter  $R_1 = 95.8 \pm 18.9$  nΩ is very high (see Fig. 5.8).

Two cavities limited at  $E_{acc} = 30.2$  MV/m and  $32.7$  MV/m also show high values for  $R_1$ . One example (cavity AC129), the surface resistance of the other cavity behaves

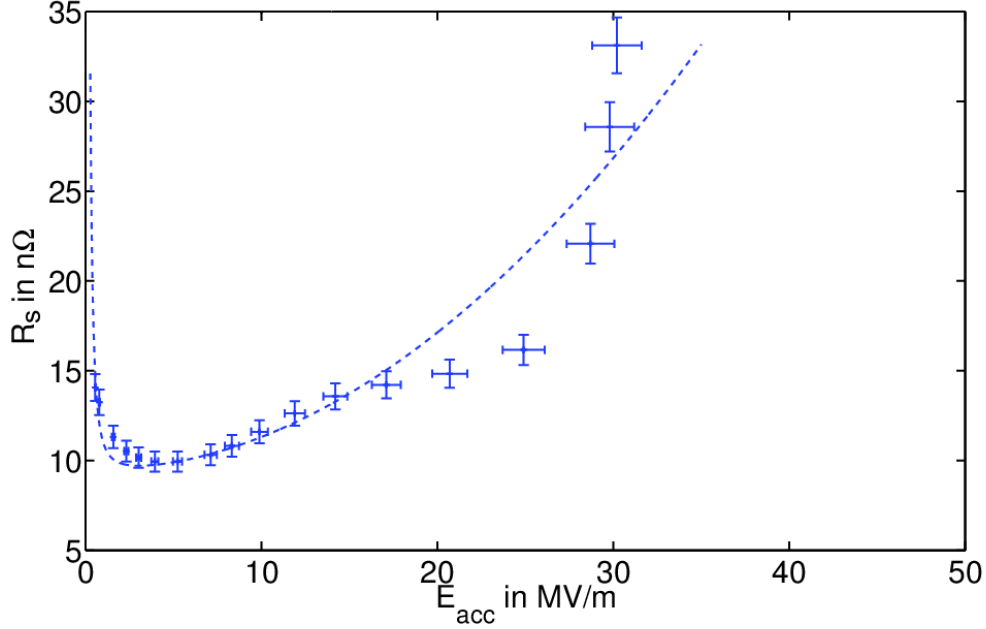


**Figure 5.10:** The surface resistance data of cavity AC129 indicates a steep slope close to the limiting accelerating field and the model fit yields a large  $R_1$ .

similar, is shown in Fig. 5.10. In this case, the absorption of the percolation term in [40] reflects in the high values of  $R_1$ , since the surface resistance rises sharply close to the limiting field, which may be an indication for insufficient baking or advanced percolation ( $T_{\text{surf}} > T^*$ ).

### Parameter $b$

The asymptotic increase of  $R_s$  with  $E_{\text{acc}} \rightarrow 0$  is indicative for the presence of dissolved elements in a thin surface layer according to [40]. This contribution to  $R_s$ , as explained in section 1.3.3 is modelled approximately with  $R_{\text{inc}}(E_{\text{acc}}) \approx \frac{b}{E_{\text{acc}}^2}$  and  $b$  describes the slope of the asymptotic part at low fields. The values obtained for  $b$  are displayed in Fig. 5.11.

The parameter  $b$  contains the latent heat  $L$  via

$$b = \frac{2\omega L \mu_0^2}{\pi c_f^2} \quad (5.3)$$

with  $\omega = 2\pi f$  as rf frequency,  $\mu_0$  as vacuum permeability, and  $c_f = 4.26 \times 10^{-3} \frac{\text{T}}{\text{MV/m}}$  as conversion factor between surface magnetic field and accelerating field (see also

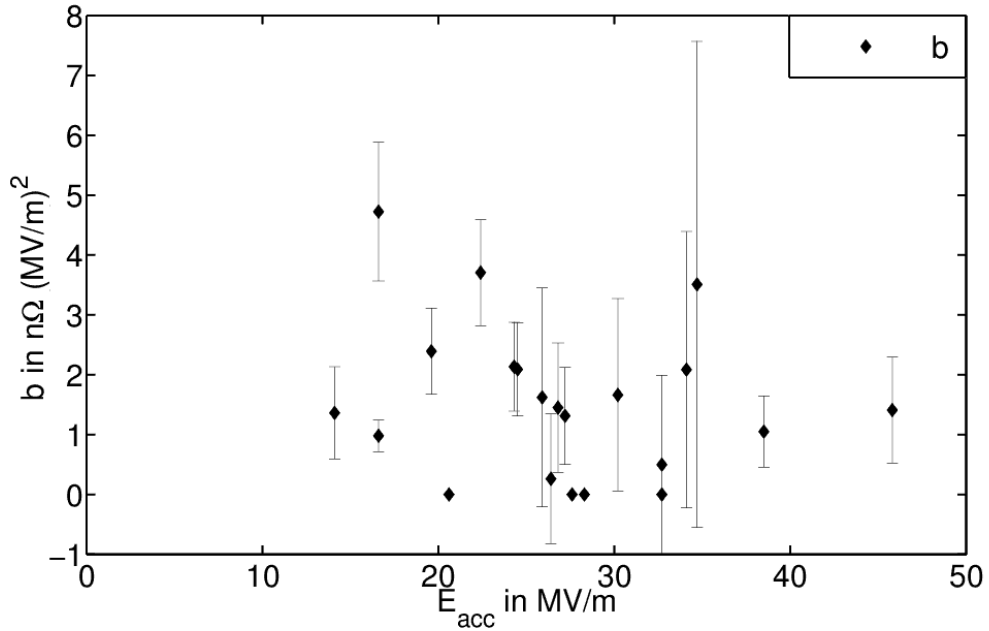


**Figure 5.11:** The fit parameter  $b$  in relation to the limiting accelerating field. It contributes to the low-field decrease of the surface resistance and is directly related to the latent heat.

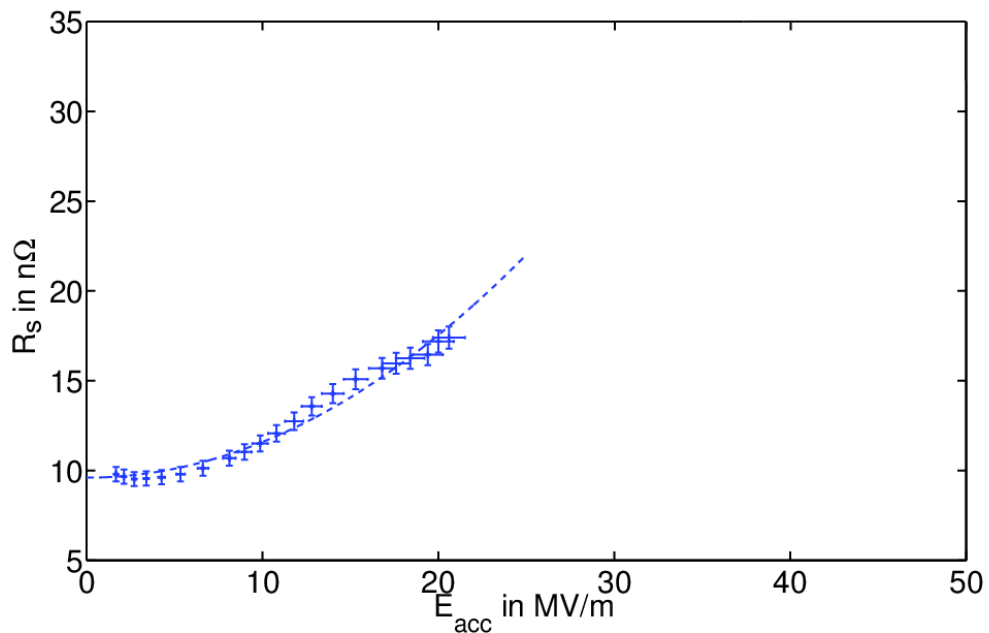


**Figure 5.12:** Cavity Z142 as example for parameter  $b$  bound to zero. The lack of data points at fields below 5 MV/m causes the uncertainty in the fit.

section 1.3.3). Modifying and insertion of (5.3) yields

$$L = \frac{\pi c_f^2}{2\omega\mu_0^2} b = 2.21 \times 10^{-12} \frac{\text{s}}{\Omega^2} \times b \quad (5.4)$$

As stated before, if  $b \leq 3 \Omega \left(\frac{\text{MV}}{\text{m}}\right)^2$  the latent heat is  $L \leq 6.6 \frac{\text{pJ}}{\text{m}^2}$  and in very good agreement with the data presented in [40].

The highest value  $b = 4.72 \Omega \left(\frac{\text{MV}}{\text{m}}\right)^2$  has been determined for cavity Z132 with a low quench limit and causes a large uncertainty in parameter  $R_1 = 118.6 \pm 11.1 \text{ n}\Omega$ . So this dataset is excluded from this consideration. In addition, four datasets yield  $b$  bound to zero. These are artefacts from the data samples itself, if an insufficient number of data points has been taken at lowest fields and hence the fit routine was not able to approximate the slope. As example in Fig. 5.12, the dataset of cavity Z142 is shown with underlying fit.

### 5.3.2 Additional resistance contribution

As the description in the accelerating field range of  $E_{\text{acc}} \approx 10 - 20 \text{ MV/m}$  of the previously introduced model is not very accurate, an additional resistance term is added to the fit function  $R_s(E_{\text{acc}})$  to describe the 'step' of the surface resistance:

$$R_{s,\text{mod}}(E_{\text{acc}}) = R_s(E_{\text{acc}}) + e_1 \times \text{erf}(e_2(E_{\text{acc}} - e_3)) + e_1 \quad (5.5)$$

It contains the errorfunction erf, which allows a description of a smooth step, as it is seen in the data. The parameter  $e_1$  indicates the additional loss  $R_{\text{step}} = 2e_1$ ,  $e_3$  gives the position of the inflexion point of the 'step' and  $e_2$  is a measure for the steepness, which is not needed for the discussion. Fig. 5.13 shows again the surface resistance data of cavity AC158 (cf. Fig. 5.5), including the fit with (5.1) and (5.5). While the fit with (5.1) yields a goodness of fit  $R^2 = 0.96$ , (5.5) achieves  $R^2 = 0.97$ , which is only a small change in accuracy.

The physical interpretation of the 'step' in this range is, that an additional loss mechanism contributes to the surface resistance from a certain accelerating field on. In particular the loss is switched on and then saturates towards higher fields, which is represented by  $R_{\text{step}} = 2e_1 = 1.3 \pm 0.8 \text{ n}\Omega$  for cavity AC158. The threshold accelerating field is given by fit parameter  $e_3 = 11.3 \pm 3.1 \text{ MV/m}$ . The fit parameters of  $R_s(E_{\text{acc}})$  are unaffected within the previously given uncertainty.

To exclude a temperature dependence of  $e_3$ , the measurements of the quality factor at a helium bath temperature of  $T = 1.8 \text{ K}$ , if available, have been examined as well and yield a similar behaviour compared to the measurements at  $2 \text{ K}$  at the same  $e_3$ . A systematic error in the measurement setup as a reason for the observed feature has been also excluded since similar curves have also been measured at other test facilities [126–128].

Using (5.5), the datasets exceeding an accelerating field of  $25 \text{ MV/m}$  have been examined. For four cavities (AC128, AC129, CAV00500 and CAV00503) the data

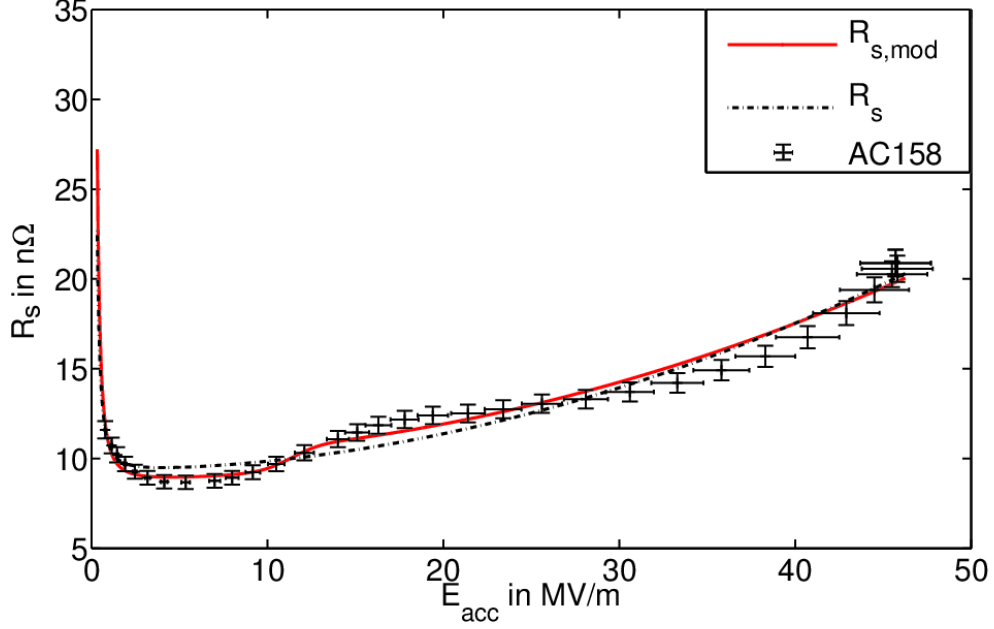


**Figure 5.13:** Cavity AC158 with underlying fits from  $R_s$  of (5.1) and  $R_{s,mod}$  of (5.5)

**Table 5.2:** Parameters of the fits for  $R_{step}$  including fitting uncertainties.

cavity	surface(grain)	$e_1/n\Omega$	$e_2/(MV/m)^{-1}$	$e_3/MV/m$	$R_{step}/n\Omega$
AC113	BCP(lg)	$1.77 \pm 0.66$	$0.23 \pm 0.13$	$13.1 \pm 1.2$	$3.44 \pm 0.93$
AC114	BCP(lg)	$1.50 \pm 0.42$	$0.24 \pm 0.10$	$12.2 \pm 0.9$	$3.00 \pm 0.59$
AC128	EP+(fg)	$2.64 \pm 0.63$	$0.20 \pm 0.05$	$10.8 \pm 0.8$	$5.28 \pm 0.89$
AC129	EP+(fg)	$1.17 \pm 0.89$	$0.38 \pm 0.56$	$10.7 \pm 2.1$	$2.34 \pm 1.26$
AC149	EP+(fg)	$1.83 \pm 0.46$	$0.22 \pm 0.10$	$10.7 \pm 1.0$	$3.66 \pm 0.65$
AC152	BCP(lg)	$1.53 \pm 0.19$	$0.21 \pm 0.04$	$11.8 \pm 0.4$	$3.06 \pm 0.27$
AC153	EP(lg)	$1.15 \pm 0.49$	$0.34 \pm 0.48$	$11.2 \pm 2.2$	$2.30 \pm 0.69$
AC155	BCP(lg)	$1.85 \pm 0.29$	$0.26 \pm 0.07$	$11.4 \pm 0.5$	$3.70 \pm 0.41$
AC156	BCP(lg)	$2.14 \pm 0.30$	$0.18 \pm 0.04$	$11.7 \pm 0.5$	$4.28 \pm 0.42$
AC158	EP(lg)	$0.63 \pm 0.39$	$0.55 \pm 1.78$	$11.3 \pm 3.1$	$1.26 \pm 0.55$
Z163	EP(fg,hyd.)	$1.97 \pm 0.13$	$0.20 \pm 0.02$	$11.6 \pm 0.3$	$3.94 \pm 0.18$
CAV00500	EP+(fg)	$1.12 \pm 0.62$	$0.24 \pm 0.15$	$12.3 \pm 1.2$	$2.24 \pm 0.88$
CAV00503	EP+(fg)	$0.97 \pm 0.33$	$0.25 \pm 0.12$	$11.7 \pm 0.9$	$1.94 \pm 0.47$

had to be manipulated by excluding the data points in the steep slope (cf. Fig. 5.10) close to the limiting gradient, as the simplification of the model in [40] cannot represent this data range accurately.

The overall results shown in Table 5.2 yield a very small onset range of the loss mechanism at  $E_{acc} = 11 - 13 MV/m$ , while the amplitude of the loss has a large

variation of  $R_{\text{step}} = 1.3 - 5.3 \text{ n}\Omega$ . The spread cannot be explained by EP and EP+ surface treatment, since Z163 with an EP'd surface also yields  $R_{\text{step}}(\text{Z163}) = 3.9 \text{ n}\Omega$ , while the other EP cavities AC153 and AC155 have rather low values below  $2 \text{ n}\Omega$ . Cavity CAV00503 with EP+ treatment as well shows a low value.

The comparison of BCP and EP treated large grain cavities shows, with two available tests for EP and five for BCP a significant difference:  $\overline{R_{\text{step}}}(\text{EP}) = 1.8 \text{ n}\Omega$ , while  $\overline{R_{\text{step}}}(\text{BCP}) = 3.5 \text{ n}\Omega$ . This supports observations made in grain boundary sample studies with applied magnetic field parallel to the grain boundary [129]. In the cavity case, the magnetic field is perpendicular to the grain boundary, where the studies [129] show no influence, as the effect diminishes by rotating the magnetic field from parallel towards perpendicular and disappears in perpendicular orientation.

Comparison of large grain and fine grain cavities with the same surface treatment is only possible with low statistics (two large grain, one fine grain with EP surface and hydroformed), although the values  $R_{\text{step}}(\text{lg}) = 2.3, 1.3 \text{ n}\Omega$  and  $R_{\text{step}}(\text{fg}) = 4.0 \text{ n}\Omega$  may give evidence for a dependence of the overall length of grain boundaries and hence resistive 'weak links' for the cooper pairs and thus reduced superconductivity.

### Interface tunnel exchange

An explanation for the increase of the surface resistance starting above 5 to 7 MV/m can be the interface tunnel exchange, as introduced in section 1.3.3 [44]. The losses occur abruptly at a certain electric field level and saturate at a higher field level as shown in Fig. 5.14. As this model only describes the loss mechanism at the  $R_s$  increase after the global minimum of  $R_s$ , for better fit results the low-field Q increase of (1.9) in the simplified version is also taken into account. The fit function is (with  $R_{\text{const.}}$  as 'arbitrary' offset, since other loss mechanisms are not taken into account as will be explained later)

$$R_{s,\text{itefit}}(E_{\text{acc}}) = \frac{b}{E_{\text{acc}}^2} + R_{\text{sat}}^E \frac{f}{400 \text{ MHz}} \left( e^{-k/(2E_{\text{acc}})} - e^{k/E^0} \right) + R_{\text{const.}}, 2E_{\text{acc}} \geq E^0. \quad (5.6)$$

The parameters obtained for the exemplary fit to data of AC155 are given in Table 5.3. The parameter  $b = 2.04$  for the low-field Q increase is reasonable, as has

**Table 5.3:** Parameters of the ITE fit obtained from cavity AC155.

$b/\text{n}\Omega(\frac{\text{MV}}{\text{m}})^2$	$R_{\text{sat}}^E/\text{n}\Omega$	$k/\text{MV}/\text{m}$	$E^0/\text{MV}/\text{m}$	$R_{\text{const.}}/\text{n}\Omega$
$2.04 \pm 0.48$	$16.7 \pm 1.3$	$25.1 \pm 10.4$	$14.6 \pm 1.6$	$10.8 \pm 0.2$

been discussed in section 5.3.1 and the offset indicated by  $R_{\text{const.}}$  is also reasonable as it complies with the values obtained for parameter  $R_2$  in the aforementioned section. The onset of the tunnelling process is given by parameter  $E_0 = 14.6 \text{ MV}/\text{m}$ , which indicates the peak electric field in an rf cycle and is  $7.3 \text{ MV}/\text{m}$  in accelerating field.

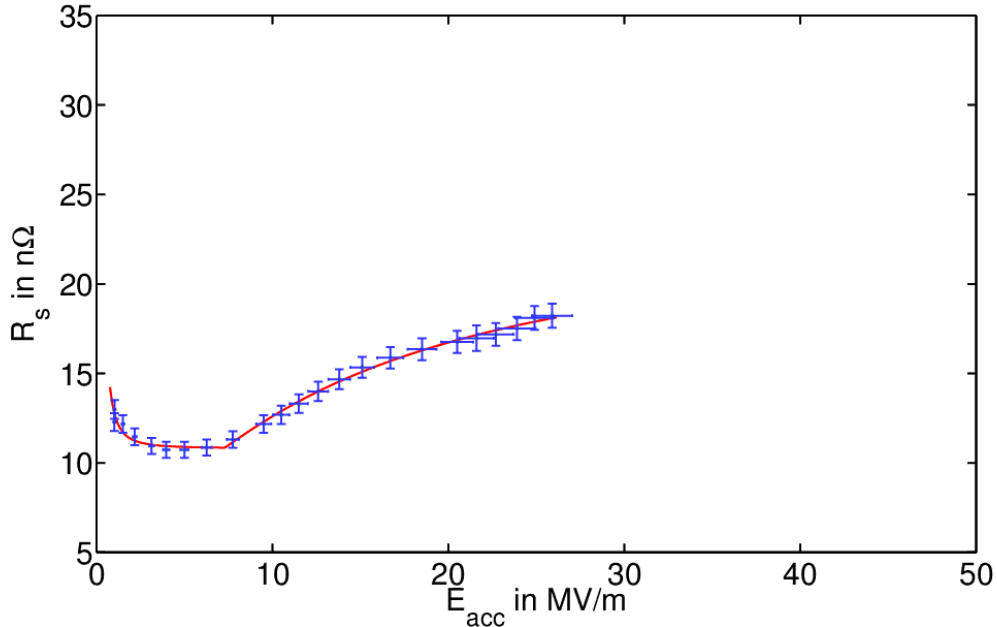


**Figure 5.14:** Surface resistance data of cavity AC155 with BCP treatment and fit to the interface tunnel exchange model including the low field Q increase  $R_{s,Q\text{-inc}}$  of [40]

This result is comparable with results obtained at other laboratories as mentioned earlier [126–128]. Parameter  $R_{\text{sat}}^E = 16.7 \text{ n}\Omega$  gives evidence of the maximum loss contribution at saturation. It is related to the total density of localised states in the oxidised grain boundaries, as the losses generated by the tunnelling will occur most likely at the boundaries. As cavity AC155 is made of large grain material, the value is lower compared to cavities made of fine grain material, as predicted by the model [130]. The parameter  $k$  contains material parameters and indicates the decay of the wave function of the cooper pairs in the insulating  $\text{Nb}_2\text{O}_5$  layer. The fit yields  $k = 25.1 \text{ MV/m}$ , which is also reasonable [130].

Note that the interface tunnel exchange model only explains the increase of  $R_s$  at low fields and the medium field Q-slope [45]. As the electric loss saturates, the model cannot describe the high field Q-drop, which is observed at usual cavity measurements reaching high accelerating fields. In addition, the increase of the quality factor at lowest fields also cannot be explained. As all losses induced by magnetic and electric field have to be considered equally, it is difficult to examine the loss mechanisms introduced, since for single cavity tests at a fixed rf frequency  $f$  and fixed temperature  $T$  it is not possible to distinguish each loss mechanism. Thus a proper measurement of the loss contributions is still missing and will require more detailed examination.

## 5.4 Summary

The quality factors and surface resistances of cavities with state-of-the-art fabrication and surface treatments were measured and show promising results. With a statistical sample of about 70 cavity tests, an averaged quality factor exceeding  $1.5 \times 10^{10}$  has been achieved, even at highest accelerating fields beyond 35 MV/m. If the cavities do not suffer from field emission or early thermal breakdown, this is very promising regarding heat loss in the cryogenic environment - and yields a reduced cryogenic heat load by about 30% compared to the specifications of  $Q_0 > 10^{10}$  for the European XFEL and ILC. No significant differences in quality factors have been found for different surface treatments like EP, EP+ and BCP. Cavities fabricated of large grain niobium yield a 10-20% higher quality factor than fine grain cavities, which coincides with observations made at other laboratories, as large grain material yields a smoother surface and grain boundaries. The variation of the quality factor and hence the surface resistance related to the RRR of the cavity material for  $RRR > 40$  has been confirmed: Higher RRR results in a higher BCS resistance and a lower  $Q_0$ , as has been shown for the eleven large grain cavities fabricated of three different niobium ingots with varying RRR.

Surface resistance data of 21 cavity tests were evaluated and a recently developed surface resistance model by Weingarten was tested on the data. The parameters obtained out of this data analysis agree with the values given by the surface resistance model. Despite the accordance, for the medium field regime between 10 and 20 MV/m the description seems to be incomplete: A smooth 'step' increases the surface resistance by 1 to 5 n $\Omega$  at accelerating fields of about 12 MV/m. To analyse this feature, an additional loss mechanism has been assumed. The results show a possible physical explanation for the additional loss, as there is first evidence for a correlation between the magnitude of the effect and the overall length of the niobium grain boundaries. A loss mechanism introduced by Halbritter in 1999, the interface tunnel exchange model, is able to explain this correlation: It describes a tunnelling effect of the electrons between the normal conducting niobium oxide layer at the grain boundaries and the superconducting bulk niobium. Detailed analysis of the heat loss at the grain boundaries of cavities is required, e.g. with temperature mapping, to confirm this loss. Thus further studies on future large and fine grain cavity quality factors with different surface treatment are required.



## CHAPTER 6

# Conclusion and Outlook

---

Two important features of superconducting rf cavities have been examined: The thermal breakdown (quench) of superconductivity and the quality factor, a measure for the surface resistance of the 1.3 GHz 9-cell cavities at DESY.

For the determination of the quench locations of cavities a measurement setup using the second sound in superfluid helium has been established and implemented at the cavity test facility at DESY. The capacitor microphone-like detectors measure the second sound signal and the calculated propagation times allow a reconstruction of the quench location with an uncertainty in the order of 1 cm. This fast method allowed measurements of the quench locations of about 30 cavities, resulting in 189 quench locations.

Most quenches have been located in the high magnetic field region of each cell, but not necessarily at the equator weld. The accelerating field achieved in the quenching cells varies from 10 to 50 MV/m. Most of the quenches occurred at fields above 30 MV/m, but the quenches in cells 1 and 2 occurred often below 30 MV/m. It also has been shown that the latter cells quench more often than expected from the field distribution: For cell 2 no particular reason was found, as the cavity assembly and treatment does not show features which can explain the excess. A comparison of both cavity vendors providing cavities to DESY allowed an attribution of the large number of quenches in cell 1 to one of both vendors. Hence there is indication that an assembly step at the cavity manufacturer causes the surplus in quenches.

The angular distribution of the quench locations shows about 70% in the region between  $270^\circ$  and  $90^\circ$ , while only 50% are expected, if an uniform distribution is assumed. Several possible causes related to cavity assembly and treatment have been examined, but no reason was found.

In summary there is evidence that there are characteristic non-random distributions of the quench locations. Although some quenches can be correlated with features found on the inner cavity surface, for most of the quenches no specific reason is found. Thus it is important to follow the production and treatment process of future cavities very closely at DESY and other laboratories to find statistic correlations between

quench locations and the fabrication process and eventually eliminate the origin causing the unwanted thermal breakdown.

At DESY this will be possible for a sample of 24 ILC-HiGrade cavities extracted from the series production for the European XFEL, where detailed production parameters will be of avail. In addition the second sound setup will be extended to a larger number of detectors to reduce the measurement uncertainties.

An investigation of the quality factors and surface resistances of the 1.3 GHz 9-cell cavities at DESY has been carried out in the course of this work and shows promising results regarding the European XFEL and the ILC.

Comparing the averaged quality factors  $Q_0$  for cavities made of large grain and fine grain material shows a  $Q_0$  which is about 20% higher for the large grain cavities, which meets the expectations, as the surface of the large grain cavities is much smoother and has fewer grain boundaries. The surface treatments for the cavities do not have different effects on the quality factor, but BCP surface cavities are usually limited at about 30 MV/m. Cavities made of niobium ingots with different RRR showed the expected behaviour, that higher RRR results in a higher BCS resistance and hence in a higher surface resistance. All cavities meet the quality factor specifications for the European XFEL and, if the required accelerating field is reached, for the ILC.

A detailed analysis for a total number of 21  $Q_0$  vs.  $E_{\text{acc}}$  measurements has been performed by applying a recently developed surface resistance model by Weingarten. Although the model fits reasonably to the data and the values obtained in the associated publication, it has been found to be incomplete. The application of the modified surface resistance function gives evidence for a loss mechanism emerging at accelerating field larger than 10 MV/m and contributes to the surface resistance for higher fields with 1 to 5 n $\Omega$ . It should be pointed out that the loss mechanism suggested by Halbritter, the interface tunnel exchange model, can describe the sudden increase of the surface resistance. It accounts for electric losses at the niobium oxide at the grain boundaries, which complies with the comparison of the strength of this effect at large and fine grain cavities. It is important that this effect is understood and eventually reduced, it can result in a maximum reduction of heat losses of about 30% for the European XFEL and 25% for the ILC.

Albeit the data sample for the examination of the surface resistance was limited to a fixed operation temperature and a single frequency, observations lead to a first improvement by using a model for an additional loss mechanism.

For a complete description of the surface resistance and discrimination of its contributions, data from superconducting cavities with various frequencies and measurements at several temperatures are required, as some contributions depend on frequency and operating temperature. While the impact of temperature dependent effects can be examined with the cavities available at DESY, the analysis of frequency dependencies will require data and detailed measurement conditions from laboratories testing cavities in other frequency bands.

# Abbreviations

ac	alternating current
BCP	Buffered Chemical Polishing
BCP Flash	up to 20 $\mu\text{m}$ BCP on EP surface
CBP	Centrifugal Barrel Polishing
CERN	European Organization for Nuclear Research
CMTB	Cryomodule Test Bench
cw	continuous wave
dc	direct current
DESY	Deutsches Elektronen-Synchrotron
EBW	electron beam weld
EP	Electropolishing
EP+	see BCP Flash
European XFEL	European X-Ray Free Electron Laser
FEL	Free-Electron Laser
FLASH	Free-Electron Laser in Hamburg
HOM	Higher Order Modes
HPR	High Pressure Rinsing
ILC	International Linear Collider
LCLS	Linac Coherent Light Source
LHC	Large Hadron Collider
linac	Linear Accelerator
mp	multipacting
OBACHT	Optical Bench for Automated Cavity Inspection with High Resolution on Short Time Scales
PLC	programmable logic controller
rf	radio frequency
PLL	Phase Lock Loop
RCV	Reference cavities for the European XFEL series production

## 6 Conclusion and Outlook

---

SACLA	SPring-8 Angstrom Compact Free Electron Laser
SLC	Stanford Linear Collider
SRF	Superconducting Radio Frequency
TESLA	Superconducting Electron-Positron Linear Collider with an Integrated X-Ray Laser Laboratory
T-map	Temperature mapping
TTF	Tesla Test Facility

## APPENDIX A

# Quench localisation

---

### A.1 Measurement Accuracy

As described in section 3.3.2, the estimated uncertainty for the localisation of the quench spot is in the order of 1 cm.

In addition, shown in chapter 4, quenches in the end cells 1 and 9 are difficult to detect, as the OSTs are placed in the range from cells 2 to 8 and the short propagation times then result in a larger error along the z-axis, as all detector signals yield a position to the center of the cavity.

For better resolution a total of 16 OSTs reduces the uncertainties by a factor of 2 and hence can specify the quench location for optical inspection or other instrumentation, which is favourable for the 24 cavities of the HiGrade programme. If required, after a first measurement, the OSTs can be clustered around the determined quench location to achieve more precise results.

### A.2 Installation Issues

#### A.2.1 High Voltage

The OSTs are biased with 120 V DC. In general, the connection and operation of the amplifier electronics is only allowed, when the cryostat insert is placed in the cryostat, so it is impossible to tear the OST diaphragm and hence touch the brass electrode on 120 V DC.

In addition, SMA connectors are not specified for the applied potential, and no standard SMA cabling is allowed - special high voltage coaxial cabling is required. The connectors and vacuum feedthrough at the cryostat lid also have to meet the voltage specifications. In addition, the connector in the helium atmosphere, especially the pins where the wires from the OSTs are soldered on, have to be isolated against each other properly, since the breakdown voltage in a helium atmosphere at  $\approx 30$  mbar, which is required for 2 K operation is lower than 50 V

For test purposes outside of the cryostat, only qualified electrotechnical staff or a electrically instructed person in strict accordance with the safety requirements is allowed to operate the OST setup.

### A.2.2 Electronic Noise

The first tests of the OSTs and the amplifier electronics showed a lot of noise (noise amplitude at the scope  $> 100$  mV with usual OST signals of  $50 - 500$  mV). As the ground potential of the cryostat itself has been excluded, the ground of the power plug was one of the noise sources, which has been disabled by using an insulating transformer. Another issue was the ground potential of the electronic racks, where are the electronic devices for cavity measurement are installed, and the switch power supplies of these devices induce noise on the racks. Hence the amplifier electronics has been placed outside of the electronic racks.

### A.2.3 Helium Bath

A first test for choose the proper helium bath temperature at DESY showed best second sound signals/amplitudes at  $T(\text{LHe}) < 1.8$  K. But to keep a stable temperature during the measurement, the limit is  $T(\text{LHe}) = 1.8$  K, which is also required for the Q vs. E measurements. In addition, the propagation velocity of the second sound in liquid helium at 1.8 K is 19.9 m/s and only varies slightly (about 2%) for a temperature measurement uncertainty of 0.1 K [99].

Another observation was made, if the dissipated power of the cavity exceeds about 100 W, the second sound signals seem 'damped', which indicates that the ratio of energy carrier medium (He II) is no longer stable around the cavity and hence the second sound signals cannot propagate as expected. This is also observed for cavities with field emission.

## A.3 Oscillating Superleak Transducers

The Oscillating Superleak Transducers (OSTs) consist of an aluminum body, a brass electrode and an aluminum retaining ring. The technical drawings are shown in Fig. A.1.

A SMA mountable socket is soldered with its pin into the pit of the brass electrode, and then glued with Stycast<sup>®</sup> 2850FT into the aluminum body. Finally, the remnants of the epoxy are removed by polishing the brass electrode to an averaged roughness of about  $1 \mu\text{m}$  [131]. The polycarbonate diaphragms Whatman 110606 have been sputtered with a thin gold layer of about 45 nm in thickness [132], and one each is placed inbetween the OST body and the retaining ring and hence is fixed. An exploded assembly drawing is shown in Fig. A.2.

### A.3 Oscillating Superleak Transducers

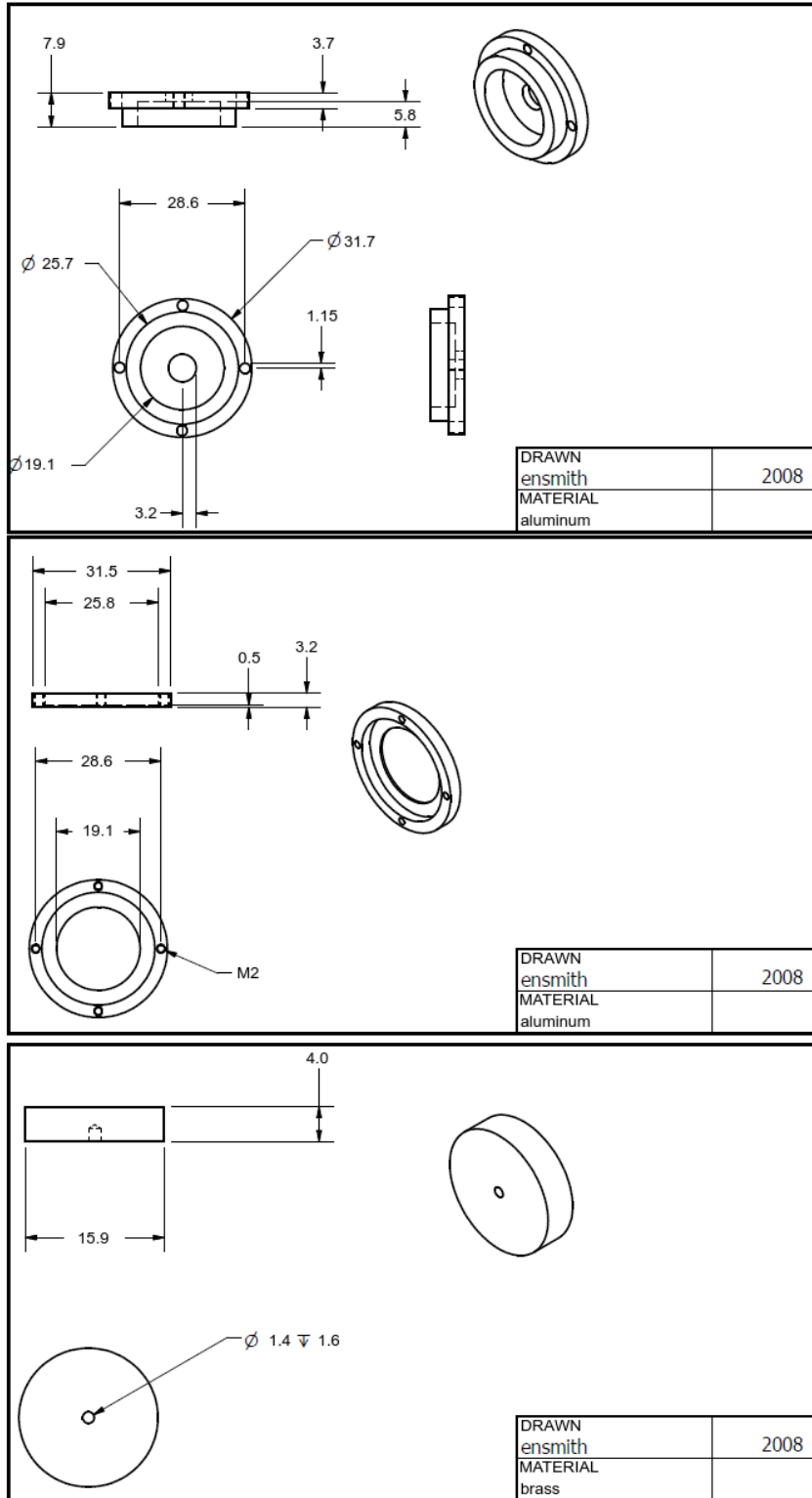
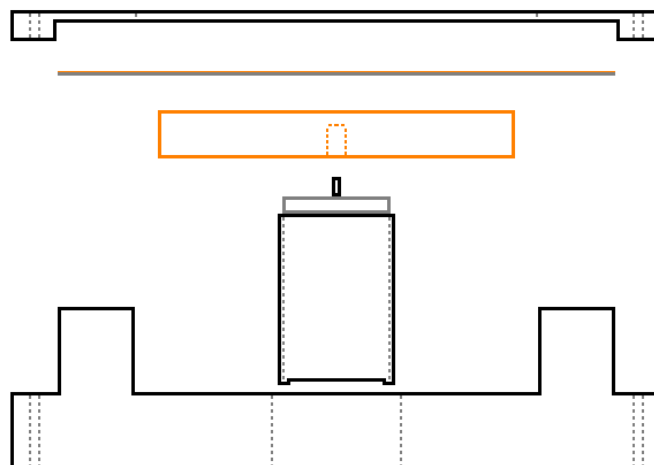


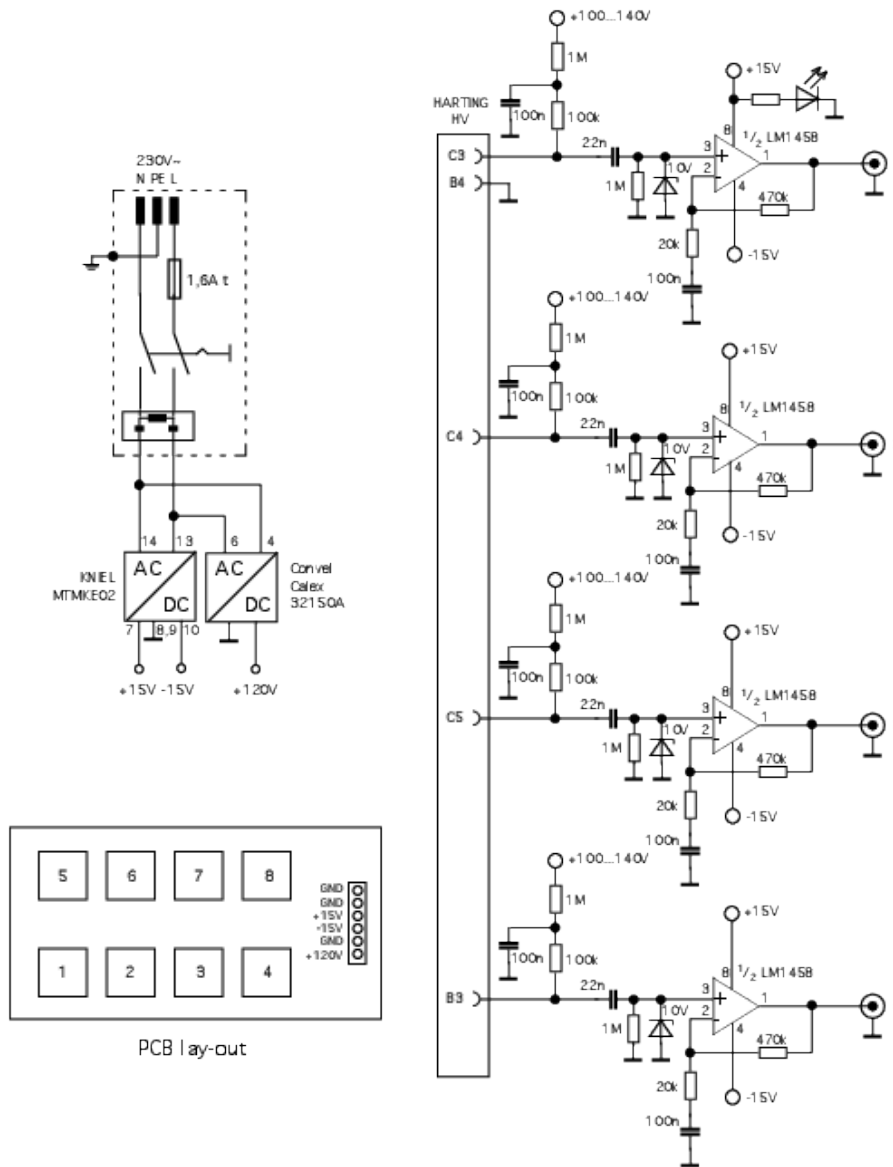
Figure A.1: Technical drawings of the OST parts *Courtesy of Cornell University*



**Figure A.2:** Exploded assembly drawing of an OST (not to scale). The SMA socket is soldered into the brass electrode and the other parts are assembled as shown.

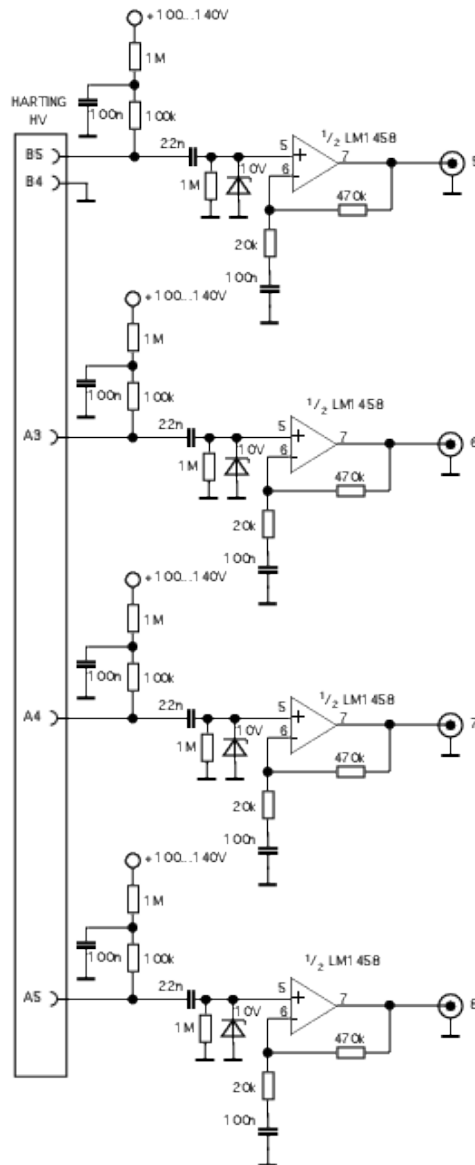


# A.4 Electronics



	Name	Date	Scale	Replacement for:	 	Cart no.:
Drawn	T.Külper	10.01.10		<b>Second Sound Amplifier circuit diagram</b> File: SecondSoundCircuit.vcx		 
Mod	T.Külper	16.10.10				
Mod						
Mod					Page 1 of 2	

## A Quench localisation





	Name	Date	Scale	Replacement for:		Cont. no.:
Drawn	T.Külper	10.02.10		<b>Second Sound Amplifier circuit diagram</b>		
Mod	T.Külper	06.10.10				
Mod				File	SecondSoundCircuit.cvx	Page 1 of 1

Figure A.3: Second sound amplifier electronics *Courtesy of T. Külper*

## APPENDIX B

# Used Datasets

---

### B.1 Second Sound Data

Table B.1 explains how the second sound datasets in Table B.2 are displayed. The data shown for the accelerating fields has been calculated from the ideal field distribution as it is used regularly during the Q vs. E mode measurements.

**Table B.1:** Explanation and example for Table B.2

'Cavity no.' test 'X'				
AC126 test 5				
x/9- $\pi$ mode	quenching cell	$E_{acc}$ /MV/m in cell	z / mm	$\Phi$
9/9	2	20.7	133	80°
8/9	2	21.0	133	80°
...	...	...	...	...

**Table B.2:** Second sound datasets

AC126 test 5					AC120 test 2				
9/9	2	20.7	133	80°	9/9	-	-	-	-
8/9	2	21.0	133	80°	8/9	-	-	-	-
7/9	9	34.2	905	340°	7/9	-	-	-	-
6/9	3	26.1	255	330°	6/9	-	-	-	-
5/9	3	25.6	255	330°	5/9	-	-	-	-
4/9	2	21.1	133	80°	4/9	-	-	-	-
3/9	2	20.8	133	80°	3/9	-	-	-	-
2/9	2	19.1	133	80°	2/9	-	-	-	-
1/9	3	21.7	255	330°	1/9	-	-	-	-

## B Used Datasets

---

Z160 test 3					Z161 test 1				
9/9	-	-	-	-	9/9	2	13.7	126	119°
8/9	8	21.9	843	35°	8/9	2	12.0	128	118°
7/9	5	27.1	463	280°	7/9	5	19.1	456	289°
6/9	1	25.4	33	29°	6/9	3	20.8	245	93°
5/9	5	26.7	463	280°	5/9	5	21.8	455	289°
4/9	-	-	-	-	4/9	2	13.5	125	128°
3/9	-	-	-	-	3/9	2	13.4	124	127°
2/9	3	27.8	259	218°	2/9	2	11.1	108	124°
1/9	5	23.7	463	280°	1/9	5	17.3	456	288°
Z162 test 2					AC151 test 3				
9/9	9	30.9	885	350°	9/9	-	-	-	-
8/9	9	30.3	884	349°	8/9	-	-	-	-
7/9	5	33.1	457	344°	7/9	-	-	-	-
6/9	9	32.4	905	350°	6/9	-	-	-	-
5/9	5	37.6	456	344°	5/9	-	-	-	-
4/9	6	36.7	565	347°	4/9	-	-	-	-
3/9	8	34.4	773	358°	3/9	-	-	-	-
2/9	3	27.8	245	293°	2/9	-	-	-	-
1/9	5	31.1	456	344°	1/9	5	43.8	452	167°
AC155 test 3					AC156 test 2				
9/9	2	45.4	173	200°	9/9	8	28.3	778	351°
8/9	1	45.5	-21	133°	8/9	1	30.2	-7	31°
7/9	1	47.0	58	230°	7/9	5	30.9	460	17°
6/9	1	43.8	58	230°	6/9	6	32.6	565	336°
5/9	5	48.5	452	186°	5/9	5	33.0	459	18°
4/9	4	51.3	353	274°	4/9	6	31.2	563	337°
3/9	2	47.9	173	200°	3/9	8	29.2	771	348°
2/9	3	47.1	247	278°	2/9	3	34.1	249	89°
1/9	5	54.4	453	186°	1/9	5	34.7	460	19°

B.1 Second Sound Data

AC158 test 3					Z160 test 5				
9/9	5	25.1	452	3°	9/9	2	19.5	76	45°
8/9	-	-	-	-	8/9	4	7.8	305	48°
7/9	-	-	-	-	7/9	1	24.7	16	6°
6/9	-	-	-	-	6/9	-	-	-	-
5/9	-	-	-	-	5/9	-	-	-	-
4/9	-	-	-	-	4/9	-	-	-	-
3/9	-	-	-	-	3/9	-	-	-	-
2/9	-	-	-	-	2/9	-	-	-	-
1/9	-	-	-	-	1/9	-	-	-	-
AC152 test 3					AC156 test 3				
9/9	3	38.2	236	119°	9/9	6	30.6	571	295°
8/9	-	-	-	-	8/9	9	36.9	883	119°
7/9	1	39.9	34	53°	7/9	9	32.7	885	112°
6/9	1	23.4	33	358°	6/9	6	32.5	564	294°
5/9	-	-	-	-	5/9	9	30.3	884	96°
4/9	-	-	-	-	4/9	6	30.5	568	296°
3/9	-	-	-	-	3/9	8	39.5	794	80°
2/9	2	17.4	128	345°	2/9	7	42.1	675	79°
1/9	2	15.8	147	345°	1/9	6	33.3	568	296°
AC157 test 2					AC153 test 2				
9/9	2	22.3	113	108°	9/9	8	36.8	791	140°
8/9	-	-	-	-	8/9	9	38.6	887	86°
7/9	-	-	-	-	7/9	9	38.3	887	85°
6/9	-	-	-	-	6/9	9	37.6	886	86°
5/9	-	-	-	-	5/9	5	41.0	464	293°
4/9	-	-	-	-	4/9	4	43.3	358	242°
3/9	-	-	-	-	3/9	8	38.9	787	151°
2/9	-	-	-	-	2/9	-	-	-	-
1/9	-	-	-	-	1/9	5	43.4	464	292°

## B Used Datasets

---

AC127 test 8					AC146 test 2				
9/9	2	16.5	149	269°	9/9	6	40.2	565	327°
8/9	2	17.6	128	272°	8/9	-	-	-	-
7/9	5	24.8	481	66°	7/9	-	-	-	-
6/9	6	22.8	591	305°	6/9	-	-	-	-
5/9	7	28.5	706	305°	5/9	-	-	-	-
4/9	2	18.8	153	275°	4/9	-	-	-	-
3/9	2	18.4	143	262°	3/9	-	-	-	-
2/9	2	19.0	119	302°	2/9	-	-	-	-
1/9	6	19.2	571	301°	1/9	-	-	-	-
AC152 test 5					AC154 test 3				
9/9	-	-	-	-	9/9	8	36.5	866	350°
8/9	-	-	-	-	8/9	8	33.5	866	16°
7/9	-	-	-	-	7/9	8	23.1	866	74°
6/9	-	-	-	-	6/9	8	0	866	72°
5/9	-	-	-	-	5/9	5	43.9	473	280°
4/9	-	-	-	-	4/9	-	-	-	-
3/9	-	-	-	-	3/9	8	42.3	788	33°
2/9	-	-	-	-	2/9	-	-	-	-
1/9	2	15.2	104	349°	1/9	4	43.7	360	275°
AC157 test 3					AC158 test 4				
9/9	3	23.2	263	142°	9/9	7	45.2	730	127°
8/9	-	-	-	-	8/9	1	45.0	33	267°
7/9	5	34.9	429	225°	7/9	-	-	-	-
6/9	3	21.9	261	142°	6/9	1	41.7	33	267°
5/9	3	21.4	258	142°	5/9	-	-	-	-
4/9	-	-	-	-	4/9	4	46.0	354	272°
3/9	5	33.5	440	224°	3/9	7	22.0	730	127°
2/9	3	22.6	241	140°	2/9	7	48.1	674	342°
1/9	3	20.5	265	141°	1/9	1	8.1	-27	304°

B.1 Second Sound Data

CAV00001 test 1					Z88 test 10				
9/9	9	28.5	927	91°	9/9	-	-	-	-
8/9	9	29.3	936	93°	8/9	1	36.0	-36	111°
7/9	9	28.6	917	79°	7/9	5	33.8	452	191°
6/9	9	29.8	931	91°	6/9	4	35.6	370	61°
5/9	-	-	-	-	5/9	5	32.3	446	191°
4/9	4	32.5	355	68°	4/9	4	34.9	372	59°
3/9	2	38.1	110	316°	3/9	-	-	-	-
2/9	7	39.4	690	137°	2/9	2	31.1	117	273°
1/9	-	-	-	-	1/9	4	30.8	355	44°
Z133 test 6					Z160 test 6				
9/9	1	16.0	37	304°	9/9	2	16.3	76	45°
8/9	1	15.6	37	305°	8/9	2	15.2	74	48°
7/9	1	15.9	37	305°	7/9	1	21.8	16	6°
6/9	1	16.3	37	303°	6/9	-	-	-	-
5/9	1	17.0	36	304°	5/9	-	-	-	-
4/9	1	17.4	37	304°	4/9	-	-	-	-
3/9	5	31.1	471	71°	3/9	-	-	-	-
2/9	7	31.5	721	296°	2/9	-	-	-	-
1/9	5	24.4	470	71°	1/9	-	-	-	-
Z163 test 2					CAV00004 test 1				
9/9	8	32.6	774	52°	9/9	8	38.1	770	290°
8/9	1	33.7	13	22°	8/9	9	40.0	889	15°
7/9	1	32.4	-19	12°	7/9	5	40.6	472	93°
6/9	6	41.1	588	146°	6/9	9	39.2	881	32°
5/9	5	43.7	470	340°	5/9	5	42.6	474	90°
4/9	6	37.9	546	175°	4/9	4	43.4	353	57°
3/9	2	29.1	92	202°	3/9	-	-	-	-
2/9	8	27.8	775	54°	2/9	7	48.7	660	293°
1/9	4	21.6	346	13°	1/9	5	22.9	473	89°

CAV00002 test 1					CAV00500 test 1				
9/9	7	37.6	666	333°	9/9	1	34.2	31	184°
8/9	9	39.1	888	340°	8/9	1	34.6	20	188°
7/9	9	40.1	888	200°	7/9	1	34.8	33	184°
6/9	7	41.1	668	332°	6/9	1	34.5	36	182°
5/9	7	42.4	676	322°	5/9	5	41.8	460	198°
4/9	6	43.2	587	4°	4/9	6	39.8	566	231°
3/9	2	40.1	125	282°	3/9	8	39.4	778	122°
2/9	7	38.6	675	315°	2/9	-	-	-	-
1/9	6	40.3	575	351°	1/9	-	-	-	-
CAV00503 test 1					CAV00502 test 1				
9/9	9	34.7	902	65°	9/9	9	29.7	885	6°
8/9	9	35.2	928	67°	8/9	9	30.3	884	7°
7/9	-	-	-	-	7/9	-	-	-	-
6/9	-	-	-	-	6/9	1	32.4	4	327°
5/9	5	36.1	463	356°	5/9	5	37.6	440	321°
4/9	4	34.2	321	65°	4/9	-	-	-	-
3/9	8	33.4	795	87°	3/9	2	38.4	100	80°
2/9	3	31.9	238	22°	2/9	-	-	-	-
1/9	5	33.8	463	356°	1/9	-	-	-	-
CAV00506 test 2									
9/9	2	34.7	89	298°					
8/9	-	-	-	-					
7/9	2	17.5	70	2°					
6/9	2	0	69	7°					
5/9	5	38.0	442	75°					
4/9	5	0	434	348°					
3/9	2	36	86	297°					
2/9	3	32.7	257	52°					
1/9	-	-	-	-					

## B.2 Quality Factor Data

The data reads as follows: For example AC112 t2 c10 25 30 means cavity AC112, (t)est 2, Q vs. E (c)urve number 10. The data behind shows the limit of inclusion in the statistics because of field emission (FE) onset ( $> 10^{-4}$  mGy/min), which is 25 MV/m in the example given, followed by the maximum accelerating field (lim.) achieved (30 MV/m). If no limit of inclusion is given, the cavity is included up to the maximum field.



### B.2.1 Data for Averaged Quality Factors

**Table B.3:** Data of large grain cavities

BCP					EP					EP+				
Cav.	t	c	FE	lim.	Cav.	t	c	FE	lim.	Cav.	t	c	FE	lim.
AC112	2	10	25	30	AC112	10	12	25	42					
AC113	3	10	-	27	AC113	4	13	20	37					
AC114	2	10	-	27	AC114	3	10	-	14					
AC151	2	12	-	27	AC151	6	2	10	23	AC151	10	2	10	22
AC152	2	12	-	27	AC152	5	13	15	32	AC152	7	2	15	29
AC153	1	3	-	24	AC153	2	10	-	39					
AC154	1	4	-	26	AC154	3	11	20	37					
AC155	1	13	-	26	AC155	3	12	30	46					
AC156	2	12	-	28	AC156	3	2	25	30	AC156	5	2	25	32
AC157	1	3	-	27	AC157	3	13	15	23	AC157	5	2	25	30
AC158	3	3	15	26	AC158	4	16	-	46					

**Table B.4:** Data of reference cavities

EP					EP+				
Cav.	t	c	FE	lim.	Cav.	t	c	FE	lim.
CAV00001	1	12	20	28	CAV00500	1	11	-	34
CAV00002	1	12	20	38	CAV00502	1	12	15	30
CAV00003	1	5	25	34	CAV00503	2	11	-	35
CAV00004	1	11	25	38	CAV00506	2	11*	-	35

\* first test had very strong field emission

**Table B.5:** Data of fine grain cavities

Cav.	EP				Cav.	EP+			
	t	c	FE	lim.		t	c	FE	lim.
AC115	1	10	30	39	AC116	1	10	25*	37
AC117	5	11	25	40	AC117	1	7	10	22
AC122	2	11	20	40	AC118	1	2	20	29
AC124	1	10	10	26	AC119	1	6	20	24
AC126	1	10	5	16	AC120	3	8	-	22
AC127	1	11	20	31	AC121	3	12	15	22
AC146	2	4	-	40	AC123	1	2	20*	32
AC147	2	3	-	38	AC126	3	9	-	20
AC149	1	11	22	27	AC128	2	10	-	32
AC150	1	10	-	34	AC129	1	6	-	30
Z131	2	11	-	17	AC147	1	11	15	27
Z132	1	6	-	17	AC149	6	2	-	28
Z134	5	4	20	36	Z132	2	10	-	17
Z136	2	3	10	25	Z133	1	8	20	27
Z137	1	11	20	25	Z135	1	6	15	29
Z139	1	12	10	25	Z137	2	10	-	24
Z141	1	11	10	18	Z138	6	5	20	35
Z142	1	11	-	21	Z140	2	12	15	22
Z143	1	9	20	33					

\* the limits given are due to the occurrence of another mode ( $7/9\pi$ ) starting from this threshold.

## B.2.2 Data for Surface Resistance Model

**Table B.6:** Data for surface resistance model tests

Cav.	t	c
AC113	3	10
AC114	2	10
AC114	5	11
AC120	3	8
AC126	3	9
AC128	2	10
AC129	1	6
AC149	6	2
AC152	2	10
AC153	1	3
AC153	2	10
AC155	1	11
AC156	2	10
AC158	4	16
CAV00500	1	11
CAV00503	2	11
Z130	3	11
Z132	2	10
Z137	2	10
Z142	1	11
Z163	2	10



# List of Figures

1.1	Schematic overview of the International Linear Collider [21]. . . . .	6
1.2	Schematic rf accelerator. . . . .	7
1.3	Schematic view of a part of a cavity with (a) cut-off tube, (b) cell, (c) equator and (d) iris. . . . .	8
1.4	Overview of a 9-cell TESLA type cavity including rf power coupler, pickup for the rf signal and HOM dampers [18]. . . . .	9
1.5	Overview of the electromagnetic field distribution in a 9-cell cavity in $\pi$ -mode. The electric field is excited along the beam axis, while the magnetic field is perpendicular and induces currents in the niobium surface [23]. . . . .	10
1.6	Field amplitudes in a 9-cell cavity depending on the mode excited. The number (x) above each plot indicates the passband mode $x/9-\pi$ . . . . .	11
1.7	Phase diagram for superconductors of type I and II. . . . .	12
1.8	Measurement of the quality factor $Q_0$ as a function of the accelerating field $E_{acc}$ for cavity AC158. . . . .	16
1.9	Signatures of performance limitations regarding the quality factor Q or the accelerating electric field E in the Q(E) curve [48]. . . . .	20
1.10	Schematic examples for multipacting (mp): (a) 1 <sup>st</sup> order mp, (b) 2 <sup>nd</sup> order mp, (c) two point mp. . . . .	21
1.11	Example for calculated trajectories of electrons starting from a field emitter [22]. . . . .	22
1.12	left: a defect generating joule heating of the surrounding niobium, but not exceeding $T_c$ ; right: niobium exceeds $T_c$ resulting in thermal breakdown [22]. . . . .	24
2.1	Superconducting 9-cell 1.3 GHz XFEL-type cavity. . . . .	25
2.2	Schematic drawing of a horizontal electropolishing device with a single cell cavity. . . . .	29
2.3	Cavity preparation schemes for the European XFEL cavities [83]. . . . .	32
3.1	Schematic drawing of a vertical cryostat including cavity insert. . . . .	34

---

3.2	Simplified overview of the rf circuit required for vertical test: The amplified and modulated signal by the rf generator is fed into the cavity and the available powers are recorded [86]. . . . .	36
3.3	Typical reflected power signals on cavity acceptance test. . . . .	37
3.4	Temperature mapping resistor card. . . . .	39
3.5	Temperature mapping system. . . . .	40
3.6	The propagation of second sound. . . . .	41
3.7	Functionality and picture of an Oscillating Superleak Transducer. . .	42
3.8	Example for a second sound event. . . . .	43
3.9	Example for the quench localisation using second sound. . . . .	44
3.10	Schematic drawing of the Kyoto Camera System in use at DESY. . .	46
3.11	Picture of the inner surface of a cavity at the equator weld. . . . .	46
3.12	The OBACHT cavity surface inspection system. . . . .	47
4.1	The coordinate system of the 1.3 GHz cavities. . . . .	50
4.2	Scatter plot of all 189 quench locations determined by second sound at DESY. . . . .	50
4.3	The total number of quenches observed in each cell. . . . .	52
4.4	Observation of quenches per cell, separated for each vendor. The dashed line shows the expected number for each cell. . . . .	53
4.5	The probabilities for the quench distribution as shown in 4.4. . . . .	54
4.6	Distribution of all thermal breakdown locations in cells 2-8 without or low field emission, summed up. In addition, a gaussian fit is shown. . . . .	55
4.7	Distribution of quench locations within a cell. . . . .	56
4.8	The number of quenches related to the field achieved in the quenching cell with 5 MV/m binning. . . . .	57
4.9	The integrated number of quenches corresponding to the field achieved in each quenching cell. . . . .	58
4.10	Angular quench distribution around the cavity. . . . .	59
4.11	Distribution of quench locations found by rotating temperature mapping from June 2007 to March 2010. . . . .	60
4.12	Angular distribution of quench locations for each vendor. . . . .	62
4.13	The angular quench distribution separated for each insert. . . . .	63
4.14	Correlation between T-Map, quench localisation by second sound and optical inspection for cavity Z161. . . . .	65
4.15	Correlation between second sound and optical inspection at cavity AC126. . . . .	66
4.16	Picture of a welding seam overlap, taken of cell 1 at Z160. . . . .	67
5.1	Averaged quality factors for different accelerating fields of eleven large grain cavities with different surface treatments. . . . .	71
5.2	Averaged quality factors for different accelerating fields for fine grain cavities sorted by surface treatment. . . . .	72

---

5.3	Quality factors of cavities made of large grain material compared to fine grain material. . . . .	73
5.4	Comparison of quality factors for cavities made of different niobium ingots with varying RRR. . . . .	74
5.5	Calculation of the surface resistance and data fit to (5.1) for cavity AC158. . . . .	76
5.6	Calculation of the surface resistance and data fit to (5.1) for cavity AC153. . . . .	76
5.7	The fit parameter $R_2$ related to the accelerating field limit varies from 7 – 14 n $\Omega$ which fits perfectly in the expected range. . . . .	78
5.8	The fit parameter $R_1$ in relation to the limiting accelerating field. . .	79
5.9	The fit at cavity AC114 matches perfectly, but the value of parameter $R_1 = 95.8 \pm 18.9$ n $\Omega$ is very high (see Fig. 5.8). . . . .	79
5.10	The surface resistance data of cavity AC129 indicates a steep slope close to the limiting accelerating field and the model fit yields a large $R_1$ . . . . .	80
5.11	The fit parameter $b$ in relation to the limiting accelerating field. It contributes to the low-field decrease of the surface resistance and is directly related to the latent heat. . . . .	81
5.12	Cavity Z142 as example for parameter $b$ bound to zero. The lack of data points at fields below 5 MV/m causes the uncertainty in the fit. . . . .	81
5.13	Cavity AC158 with underlying fits from $R_s$ of (5.1) and $R_{s,mod}$ of (5.5)	83
5.14	Surface resistance of cavity AC155 with interface tunnel exchange fit.	85
A.1	Technical drawings of OST parts . . . . .	93
A.2	Exploded assembly drawing of an OST . . . . .	94
A.3	Second sound amplifier electronics <i>Courtesy of T. K�ulper</i> . . . . .	96





# List of Tables

1.1	Design parameters of the European XFEL accelerator [18]	5
1.2	Design parameters of the ILC main linacs [19]	6
2.1	Design parameters of the 1.3 GHz 9-cell cavities for the European XFEL [18]	25
3.1	Parameters and uncertainties for calculation of $Q_0$ and $E_{\text{acc}}$ , the power errors are 0.2 dB	38
4.1	Angular distribution of quenches separated for inserts.	63
5.1	Parameters of the fits obtained from cavities AC158 and AC153.	77
5.2	Parameters of the fits for $R_{\text{step}}$ including fitting uncertainties.	83
5.3	Parameters of the ITE fit obtained from cavity AC155.	84
B.1	Explanation and example for Table B.2	97
B.2	Second sound datasets	97
B.3	Data of large grain cavities	103
B.4	Data of reference cavities	103
B.5	Data of fine grain cavities	104
B.6	Data for surface resistance model tests	105



# References

- [1] K. Balewski, (ed.), W. Brefeld, (ed.), W. Decking, (ed.), H. Franz, (ed.), R. Roehrsberger, (ed.), and E. Weckert, (ed.). Petra III: A Low Emittance Synchrotron Radiation Source - Technical Design Report. Technical report, DESY, 2004.
- [2] R. Wideroe. Ueber Ein Neues Prinzip Zur Herstellung Hoher Spannungen. *Archiv fuer Elektronik und Uebertragungstechnik*, 21:387, 1928.
- [3] E. O. Lawrence. Method and Apparatus for the Acceleration of Ions, 1934.
- [4] V. I. Veksler. A New Method of Accelerating Relativistic Particles. *Comptes Rendus (Doklady) de l'Academie Sciences de l'URSS*, 43:329–331, 1944.
- [5] LHC Design Report.  
<http://lhc.web.cern.ch/lhc/LHC-DesignReport.html>.
- [6] Georges Aad et al. Observation of a new particle in the search for the Standard Model Higgs boson with the ATLAS detector at the LHC. *Phys.Lett.*, B716:1–29, 2012.
- [7] Serguei Chatrchyan et al. Observation of a new boson at a mass of 125 GeV with the CMS experiment at the LHC. *Phys.Lett.*, B716:30–61, 2012.
- [8] J.E. Augustin, N. Dikansky, Ya. Derbenev, J. Rees, Burton Richter, et al. Limitations on Performance of e+ e- Storage Rings and Linear Colliding Beam Systems at High Energy. *eConf*, C781015:009, 1978.
- [9] R.B. Neal, (ed.), D.W. Dupen, H.A. Hogg, and G.A. Loew. *The Stanford two mile accelerator*. 1968.
- [10] R. Erickson, (ed.). SLC Design handbook. Technical report, SLAC, 1984.
- [11] A. Richter. Operational Experience at the S-DALINAC. In *Proceedings of the 5th European Particle Accelerator Conference (EPAC 1996)*, 1996.
- [12] R. Legg. Operating Experience at CEBAF. In *Proceedings of the European Particle Accelerator Conference EPAC1996*, 1996.

- [13] R. Brinkmann, (ed.), K. Flöttmann, (ed.), J. Rossbach, (ed.), P. Schmüser, (ed.), N. Walker, (ed.), and H. Weise, (ed.). TESLA: The superconducting electron positron linear collider with an integrated X-ray laser laboratory. Technical design report. Pt. 2: The accelerator. Technical report, TESLA, 2001. DESY-01-011.
- [14] Carlo Pagani. Developments and Achievements at the TESLA Test Facility (TTF). *IEEE Transactions on Applied Superconductivity*, 9(2):276–281, June 1999.
- [15] J. R. Schneider, R. H. Nielsen, J. Feldhaus, B. Keitel, W. Laasch, P. Schmüser, B. Sonntag, and K. Tiedke. *Flash - The Free Electron Laser in Hamburg*. Deutsches Elektronen-Synchrotron DESY, 2007.
- [16] J. et al. Arthur. Linac Coherent Light Source: Conceptual Design Report. Technical Report SLAC-R-593 UC-414, SLAC, 2002.
- [17] T. Tanaka, (ed.) and T. Shintake, (ed.). SCSS X-FEL Conceptual Design Report. Technical report, RIKEN Harima Institute/SPRING-8, 2005.
- [18] M. Altarelli et al. The European X-Ray Free Electron Laser Technical Design Report. Technical Report DESY 06-97, Deutsches Elektronen-Synchrotron DESY, 2007.
- [19] J. Brau, (ed.) et al. International Linear Collider Reference Design Report. 1: Executive Summary. 2: Physics at the ILC. 3: Accelerator. 4: Detectors. Technical report, ILC Global Design Effort, 2007.
- [20] E. Elsen, (ed.), M. Harrison, (ed.), L. Heslach, (ed.), M. Ross, (ed.), P. Royole-Degieux, (ed.), R. Takahashi, (ed.), N. Walker, (ed.), B. Warmbein, (ed.), A. Yamamoto, (ed.), Y. Yokoya, (ed.), and M. Zhang, (ed.). International Linear Collider: A Technical Progress Report. Technical Report ILC-Report-2011-30, International Linear Collider, 2011.
- [21] J. Carwardine, (ed.). International Linear Collider: Technical Design Report. Technical report, International Linear Collider, to be published.
- [22] H. Padamsee, J. Knobloch, and T. Hays. *RF Superconductivity for Accelerators*. Wiley-VCH Verlag, Weinheim, 2008.
- [23] M. Pekeler. *Untersuchungen der feldbegrenzenden Mechanismen in supraleitenden Niob-Resonatoren*. PhD thesis, Universität Hamburg, 1996.
- [24] D. Reschke, S. Aderhold, A. Goessel, J. Iversen, S. Karstensen, D. Kostin, G. Kreps, A. Matheisen, W.-D. Moeller, F. Schlander, W. Singer, X. Singer, N. Steinhilber, A. A. Sulimov, and K. Twarowski. Update on Large

- 
- Grain Cavities with 45 MV/m in a Nine-Cell Cavity at DESY. In *Proceedings of the 15th International Conference on RF Superconductivity*, 2011.
- [25] Cavity Database of the Tesla Technology Collaboration, 2012.  
[http://tesla-new.desy.de/cavity\\_database/](http://tesla-new.desy.de/cavity_database/).
- [26] F. Schlander, S. Aderhold, E. Elsen, D. Reschke, and M. Wenskat. Quality Assessment for Industrially Produced High-Gradient Superconducting Cavities. In *Proceedings of the 2011 International Particle Accelerator Conference (IPAC 2011)*, 2011.
- [27] J. Sekutowicz, K. Ko, L. Ge, L. Lee, Z. Li, C. Ng, Schussman G., L. Xiao, I. Gonin, T. N. Khabiboulline, N. Solyak, Y. Morozumi, K. Saito, and P. Kneisel. Design of a Low Loss SRF Cavity for the ILC. In *Proceedings of the 1995 Particle Accelerator Conference*, 2005.
- [28] J. Bardeen, L. N. Cooper, and J. R. Schrieffer. Theory of Superconductivity. *Physical Review*, 108:1175–1204, 1957.
- [29] A. Grassellino, C. Beard, P. Kolb, R. Laxdal, D. Longuevergne, V. Zvyagintsev, and A. Romanenko. Q-Slope Analysis of Low-Beta SRF Cavities. In *AIP Conf. Proc.*, volume 1352, pages 161–168, 2011.
- [30] F. Palmer. Surface Resistance of Superconductors - Examples from Nb-O Systems. In *Proceedings of the 3rd Workshop on RF Superconductivity*, 1987.
- [31] B. Piosczyk, P. Kneisel, J. Stoltz, and J. Halbritter. Investigations of Additional Losses in Superconducting Niobium Cavities due to Frozen-In Flux. In *Proceedings of the Particle Accelerator Conference PAC1973*, 1973.
- [32] H. Padamsee. *RF Superconductivity*. Wiley-VCH Verlag, Weinheim, 2009.
- [33] P. Bauer, N. Solyak, G.L. Ciovati, G. Ereemeev, A. Gurevich, L. Lilje, and B. Visentin. Evidence for Non-Linear BCS Resistance in SRF Cavities. In *Proceedings of the 12th Workshop on RF Superconductivity*, 2005.
- [34] G. Ciovati and J. Halbritter. Analysis of the Medium Field Q-Slope in Superconducting Cavities made of Bulk Niobium. In *Proceedings of the 12th International Workshop on RF Superconductivity*, 2005.
- [35] B. Visentin. Review on Q-drop mechanism. In *The International Workshop on Thin Films*, 2006.
- [36] A. Gurevich. Multiscale Mechanisms of SRF Breakdown. In *Proceedings of the 12th International Conference on RF Superconductivity*, 2005.
- [37] H. Elias. Diplomarbeit. Master’s thesis, Bergische Universitaet Wuppertal, 1985.

## References

---

- [38] P. L. Kapitza. *J. Phys. U.S.S.R.*, 4:181, 1941.
- [39] D. Reschke. Thermal Model Calculations for 1.3 GHz TTF Accelerator Cavities. In *Proceedings of the 8th Workshop on RF Superconductivity*, 1997.
- [40] Wolfgang Weingarten. Field-dependent surface resistance for superconducting niobium accelerating cavities. *Phys.Rev.ST Accel.Beams*, 14:101002, 2011.
- [41] C. Poole. *Handbook of Superconductivity*. Academic Press London, 2000.
- [42] G. Deutscher and P.G. de Gennes. Proximity Effects. In *Superconductivity*, page 1005, 1969.
- [43] J. Halbritter. On the Oxidation and on the Superconductivity of Niobium. *Applied Physics A - Solids and Surfaces*, 43:1–28, 1987.
- [44] J. Halbritter. Residual Losses, High Electric and Magnetic RF Fields in Superconducting Cavities. In *Superconducting Materials for High Energy Colliders - Proceedings of the 38th Workshop of the INFN Eloisatron Project*, 1999.
- [45] T. Junginger. *Investigations of the Surface Resistance of Superconducting Materials*. PhD thesis, Ruperto-Carola University of Heidelberg, 2012.
- [46] J. D. Jackson. *Classical Electrodynamics*. New York Wiley, 2006.
- [47] B. Aune, R. Bandelmann, D. Bloess, B. Bonin, A. Bosotti, M. Champion, C. Crawford, B. Deppe, D. A. Edwards, H. T. Edwards, M. Ferrario, M. Fouaidy, P.-D. Gall, A. Gamp, A. Goessel, J. Graber, D. Hubert, M. Huening, M. Juillard, T. Junquera, H. Kaiser, G. Kreps, M. Kuchnir, R. Lange, M. Leenen, M. Liepe, L. Lilje, A. Matheisen, W.-D. Moeller, A. Mosnier, H. Padamsee, C. Pagani, M. Pekeler, H.-B. Petersen, O. Peters, D. Proch, K. Rehlich, D. Reschke, H. Safa, T. Schilcher, P. Schmueser, J. Sekutowicz, S. Simrock, W. Singer, M. Tigner, D. Trines, K. Twarowski, G. Weichert, J. Weisend, J. Wojtkiewicz, S. Wolff, and K. Zapfe. Superconducting TESLA cavities. *Physical Review Special Topics - Accelerators And Beams*, 3(9):092001, Sep 2000.
- [48] K. Saito. Basic Principles of SRF. Talk - Tutorial at the SRF Workshop 2005, 2005.
- [49] B. Bonin and R. W. Roeth. Q degradation of Niobium cavities due to Hydrogen contamination. In *Proceedings of the 5th Workshop on RF Superconductivity*, 1991.

- 
- [50] K. Schulze, O. Bach, D. Lupton, and F. Schreiber. Purification of Niobium. In Harry Stuart, editor, *Niobium - Proceedings of the International Symposium*, 1981.
- [51] P. Kneisel, R. Vincon, and J. Halbritter. First Results on Elliptically Shaped Cavities. *Nuclear Instruments and Methods*, 188:669–670, 1981.
- [52] D. Proch and U. Klein. Multipacting in Superconducting RF structures. *Proceedings Conference for Future Possibilities for Electron Accelerators*, 1979.
- [53] P. Kneisel, B. Lewis, and L. Turlington. Experience with High Pressure Ultrapure Water Rinsing of Niobium Cavities. In *Proceedings of the 6th Workshop on RF Superconductivity*, 1993.
- [54] A. Navitski. *Scanning field emission investigations of structured CNT and MNW cathods, niobium surfaces and photocathodes*. PhD thesis, Bergische Universität Wuppertal, 2010.
- [55] H. Padamsee, D. Proch, P. Kneisel, and J. Mioduszewski. Field strength limitations in superconducting cavities - multipacting and thermal breakdown. *IEEE Transactions on Magnetics*, 17:947–950, Jan 1981.
- [56] L. Lilje. *Experimental Investigations on Superconducting Niobium Cavities at Highest Radiofrequency Fields*. PhD thesis, Universität Hamburg, 2001.
- [57] R. Grill, W. Simader, D. Janda, M. Heilmaier, W. Singer, and X. Singer. Correlation of Microstructure, Chemical Composition and RRR-Value in High Purity Niobium (Nb-RRR). In *Proceedings of the 15th International Conference on RF Superconductivity*, 2011.
- [58] W. Singer, D. Proch, and A. Brinkmann. Diagnostic of Defects in High Purity Niobium. In *Proceedings of the 8th Workshop of Superconductivity*, 1997.
- [59] A. Brinkmann, M. Lengkeit, X. Singer, and W. Singer. Testing of Niobium Material for the European XFEL Pre-Series Production. In *Proceedings of Linear Accelerator Conference LINAC2010*, 2010.
- [60] J. Iversen, T. Buettner, A. Goessel, D. Klinke, G. Kreps, W.-D. Moeller, and C. Mueller. Development and Design of a RF-measurement machine for the European XFEL cavity fabrication. In *Proceedings of the 14th International Conference on RF Superconductivity*, 2009.
- [61] W. Singer, S. Aderhold, J. Iversen, G. Kreps, A. Matheisen, X. Singer, K. Twarowski, H. Weise, M. Pekeler, F. Scholz, and B. Spaniol. Advances in

## References

---

- Large Grain Resonators for the European XFEL. In *AIP Conf. Proc.*, volume 1352, pages 13–24, 2011.
- [62] P. Kneisel, G. Myneni, G. Ciovati, J. Sekutowicz, and T. Carneiro. Preliminary Results from Single Crystal and Very Large Crystal Niobium Cavities. In *Proceedings of the 2005 Particle Accelerator Conference*, 2005.
- [63] W. Singer, S. Aderhold, J. Iversen, G. Kreps, L. Lilje, A. Matheisen, X. Singer, H. Weise, M. Pekeler, J. Schwellenbach, F. Schoelz, B. Spaniol, and E. Stiedl. Development of Large Grain Superconducting Resonators for the European XFEL. In *Proceedings of the 2009 Particle Accelerator Conference (PAC09)*, 2009.
- [64] L. Lilje, C. Antoine, C. Benvenuti, D. Bloess, J. P. Charrier, E. Chiaveri, L. Ferreira, R. Losito, A. Matheisen, H. Preis, D. Proch, D. Reschke, H. Safa, P. Schmueser, D. Trines, B. Visentin, and H. Wenniger. Improved surface treatment of the superconducting TESLA cavities. *Nuclear Instruments and Methods in Physics Research A*, 526:213–227, 2004.
- [65] F. Schländer, S. Aderhold, D. Reschke, and K. Twarowski. Recent Results from Second Sound, T-Mapping and Optical Inspection of 1.3 GHz Cavities at DESY. In *Proceedings of the 15th International Conference on RF Superconductivity*, 2011.
- [66] P. Kneisel, R. W. Roeth, and H.-G. Kuerschner. Results from a nearly "Defect-free" Niobium Cavity. In *Proceedings of the 1995 Workshop on RF Superconductivity*, 1995.
- [67] W. C. Elmore. Electrolytic Polishing. *J. Appl. Phys.*, 10:724–727, 1939.
- [68] W. C. Elmore. Electrolytic Polishing II. *J. Appl. Phys.*, 11:797–799, 1940.
- [69] P. Kneisel. Surface treatment of Niobium. In *Proceedings of the First Workshop on RF Superconductivity*, 1980.
- [70] L. Ponto and M. Hein. Verfahren zur elektrochemischen Politur von Niob. Technical Report WUB 86-17, Bergische Universität Wuppertal, 1986.
- [71] A. Citron, G. Dammertz, M. Grundner, L. Husson, R. Lehm, and H. Lengeler. The Karlsruhe - CERN superconducting rf separator. *Nuclear Instruments and Methods*, 164(1):31 – 55, 1979.
- [72] K. Saito, Y. Kojima, F. Takaaki, S. Mitsunobu, S. Noguchi, K. Hosoyama, T. Nakazazo, T. Tajima, and K. Asano. R&D on Superconducting Cavities at KEK. In *Proceedings of the 4th Workshop on RF Superconductivity*, 1989.



- 
- [73] B. van der Horst, A. Matheisen, B. Petersen, S. Saegbarth, and P. Schilling. Update on cavity preparation for high gradient superconducting multicell cavities at DESY. In *Proceedings of the 13th International Workshop on RF Superconductivity*, 2007.
- [74] R. L. Geng and C. Crawford. Standard Procedures of ILC High Gradient Cavity Processing and Handling at Jefferson Lab. In *Proceedings of the 15th international conference on RF superconductivity*, 2011.
- [75] R. L. Geng, C. Crawford, H. Padamsee, and A. Seaman. Vertical Electropolishing Niobium Cavities. In *Proceedings of the 12th International Workshop on RF Superconductivity*, 2005.
- [76] C. Cooper, K. Saito, B. Bullock, S. Joshi, and A. Palczewski. Centrifugal Barrel Polishing of Cavities Worldwide. In *Proceedings of the 15th International Conference on RF Superconductivity*, 2011.
- [77] K. Escherich, A. Matheisen, R. Bandelmann, H. M. Zimmermann, and N. Krupka. A New High Pressure Rinsing System Established at DESY. In *Proceedings of the 14th international conference on RF superconductivity*, 2009.
- [78] J. H. Thie, A. Goessel, J. Iversen, D. Klinke, W.-D. Moeller, C. Mueller, D. Proch, R. H. Carcagno, T. N. Khabiboulline, S. Kotelnikov, A. Makulski, J. M. Nogiec, R. Nehring, M. Ross, and W. Schappert. Mechanical Design of Automatic Cavity Tuning Machines. In *Proceedings of the 14th international conference on RF superconductivity*, 2009.
- [79] J. H. Thie, A. Goessel, J. Iversen, D. Klinke, G. Kreps, W.-D. Moeller, C. Mueller, H.-B. Peters, A. A. Sulimov, D. Tischauer, D. Bhogadi, R. H. Carcagno, T. N. Khabiboulline, S. Kotelnikov, A. Makulski, R. Nehring, J. M. Nogiec, W. Schappert, and C. Sylvester. Commissioning and Upgrade of Automatic Cavity Tuning Machines for the European XFEL. In *Proceedings of the 15th International Conference on RF Superconductivity*, 2011.
- [80] J. Sekutowicz. Superconducting Elliptical Cavities. In *Proceedings of the CAS - CERN Accelerator School: RF for Accelerators*, 2010.
- [81] J Sekutowicz. *Multi-Cell Superconducting Structures for High Energy  $e^+ e^-$  Colliders and Free Electron Laser Linacs; EuCARD Editorial Series on Accelerator Science and Technology, (J-P.Koutchouk, R.S.Romaniuk, Editors), Vol.01. oai:cds.cern.ch:1343478*. EuCARD Editorial Series on Accelerator Science and Technology. 2008.

## References

---

- [82] G. Ciovati, P. Kneisel, and G. Myneni. Effect of Low Temperature Baking on Niobium Cavities. In *Proceedings of the 11th Workshop on RF Superconductivity*, 2003.
- [83] D. Reschke, L. Lilje, and H. Weise. Analysis of RF results of recent nine-cell cavities at DESY. In *Proceedings of the 14th international conference on RF superconductivity*, 2009.
- [84] D. Edwards. TESLA Test Facility Linac Design Report, 1995. [http://tesla.desy.de/TTF\\_Report/CDR/TTFcdrTab.html](http://tesla.desy.de/TTF_Report/CDR/TTFcdrTab.html).
- [85] H.D. Brueck and M. Stolper. Measurements of the Magnetic Shield for the TTF Bath Cryostat. Technical report, DESY, 1994. TESLA1994-10.
- [86] TTF Cavity Test. DESY Intranet. <http://www-mhf.desy.de/desy/ttfadm/>.
- [87] T. Buettner. private communication.
- [88] J. Kuzminski. First Cold Test of TESLA Superconducting RF Cavity in Horizontal Cryostat (CHECHIA). In *Proceedings of the 1995 Workshop on RF Superconductivity*, 1995.
- [89] D. Kostin, W.-D. Moeller, A. Goessel, and R. Lange. Testing the Flash Superconducting Accelerating Modules. In *Proceedings of the 13th International Workshop on RF Superconductivity*, 2007.
- [90] D. Reschke. Analysis of quenches using temperature mapping in 1.3 GHz SCRF cavities at DESY. In *Proceedings of the XXIV Linear Accelerator Conference*, 2008.
- [91] Q. S. Shu, B. Deppe, W.-D. Moeller, M. Pekeler, D. Proch, T. Junquera, A. Caruette, and M. Fouaidy. Experience in Design, Construction and Application of A Rotating T-R Mapping System in Superfluid He for TESLA 9-Cell Cavities. In *Proceedings of the 7th International Workshop on RF Superconductivity*, 1995.
- [92] L. Tisza. Sur la theorie des liquides quantiques. Application a l'helium liquide. *Journal de Physique et le Radium*, 1(5+8):164–172, 350–358, 1940.
- [93] L. Tisza. The Theory of Liquid Helium. *Physical Review*, 72:838–854, 1947.
- [94] Z. A. Conway, D. L. Hartill, H. Padamsee, and E. N. Smith. Oscillating Superleak Transducers for Quench Detection in Superconducting ILC Cavities cooled with Helium-II. In *Proceedings of the XXIV Linear Accelerator Conference*, 2008.

- 
- [95] F. Schlander, E. Elsen, and D. Reschke. Second Sound as an Automated Quench Localisation Tool at DESY. In *Proceedings of the 15th International Conference on RF Superconductivity*, 2011.
- [96] K. Shepard, C. Scheibelhut, P. Markovich, R. Benaroya, and L. Bollinger. Development and production of superconducting resonators for the argonne heavy ion linac. *Magnetics, IEEE Transactions on*, 15(1):666 – 669, jan 1979.
- [97] R. A. Sherlock and D. Edwards. Oscillating Superleak Second Sound Transducers. *Review of Scientific Instruments*, 41(11):1603, 1970.
- [98] F. Schlander, S. Aderhold, E. Elsen, and D. Reschke. Progress on diagnostic tools for superconducting high-gradient cavities. In *Proceedings of Linear Accelerator Conference LINAC2010*, 2010.
- [99] Rabi T. Wang, William T. Wagner, and Russell J. Donnelly. Precision second-sound velocity measurements in helium II. *Journal of Low Temperature Physics*, 68:409–417, 1987. 10.1007/BF00682305.
- [100] Y. Maximenko and D. Sergatskov. Quench Dynamics in SRF Cavities: Can We Locate the Quench Origin with 2nd Sound? In *Proceedings of 2011 Particle Accelerator Conference*, 2011.
- [101] ZhenChao Liu, Michael Kelly, and Alireza Nassiri. New method to improve the accuracy of quench position measurement on a superconducting cavity by a second sound method. *Phys. Rev. ST Accel. Beams*, 15:092001, Sep 2012.
- [102] F. Schlander and E. Elsen. 2nd Sound as quench localisation tool. Technical report, ILC HiGrade, 2010. <http://www.ilc-higrade.eu/e83212/>.
- [103] Y. Iwashita, H. Hayano, and Y. Tajima. Development of high resolution camera and observations of superconducting cavities. In *Proceedings of the 11th European Particle Accelerator Conference (EPAC 08)*, 2008.
- [104] S. Aderhold and D. Reschke. High-Gradient SRF Research at DESY. In *XXIV International Symposium on Lepton and Photon Interactions at High Energies*, 2009.
- [105] S. Aderhold. *Study of Field-Limiting Defects in Superconducting RF Cavities for Electron Accelerators*. PhD thesis, Hamburg University, to be published.
- [106] S. Aderhold. Optical Inspection of SRF Cavities at DESY. In *Proceedings of the 2010 International Particle Accelerator Conference (IPAC 2010)*, 2010.
- [107] S. Aderhold. private communication.
- [108] S. Karstensen. Software for Image Acquisition for OBACHT.

## References

---

- [109] M. Wenskat, S. Aderhold, E. Elsen, S. Karstensen, F. Schländer, and L. Steder. Image Processing for Characterisation of Surfaces of Superconducting RF Cavities. In *Proceedings of the 2012 International Particle Accelerator Conference (IPAC 2012)*, 2012.
- [110] K. Watanabe, H. Hayano, E. Kako, S. Noguchi, T. Shishido, Y. Yamamoto, and Y. Iwashita. Repair Techniques of Superconducting Cavity for Improvement Cavity Performance at KEK-STF. In *Proceedings of the 2010 International Particle Accelerator Conference (IPAC 2010)*, 2010.
- [111] M. Ge, G. Wu, J. Ruan, J. Ozelis, E. Borissov, T. Nicol, D. Hicks, D. Sergatskov, and L. D. Cooley. Repair SRF Cavities by Re-Melting Surface Defects via High Power Laser Technique. In *Proceedings of the 15th International Conference on RF Superconductivity*, 2011.
- [112] M. J. Kelley, S. Singaravelu, J. M. Klopff, G. Krafft, and C. Xu. Laser Melt Smoothing of Niobium Superconducting Radio Frequency Cavity Surfaces. In *Proceedings of the 15th International Conference on RF Superconductivity*, 2011.
- [113] F. Schländer. Statistical analysis of quench locations of 1.3 GHz superconducting rf cavities at DESY. Technical report, ILC HiGrade, 2012. <http://www.ilc-higrade.eu/e83212/>.
- [114] J. Iversen, R. Bandelmann, G. Kreps, W.-D. Moeller, D. Proch, J. Sekutowicz, and W. Singer. A Review of the 1.3 GHz Superconducting 9-cell Cavity Fabrication for DESY. In *Proceedings of Linear Accelerator Conference LINAC2010*, 2010.
- [115] S. Aderhold, E. Elsen, F. Schländer, and L. Steder. A Common Cavity Coordinate System. Technical report, ILC HiGrade, 2011. <http://www.ilc-higrade.eu/e83212/>.
- [116] B. van der Horst, M. Schalwat, N. Steinhau-Kuehl, and A. Matheisen. private communication.
- [117] W. Singer, X. Singer, and J. Iversen. private communication.
- [118] J. Sekutowicz. private communication.
- [119] J. Eschke. private communication.
- [120] X. Singer, S. Aderhold, A. Ermakov, D. Reschke, W. Singer, K. Twarowski, and M. Hoss. Investigation of Samples Separated From Prototype Cavities of the European XFEL. In *Proceedings of the 15th International Conference on RF Superconductivity*, 2011.

- 
- [121] J. Knobloch and R. Freyman. Effect of High-Pressure Rinsing on Niobium. Technical report, 1998.
- [122] F. Palmer. *Influence of Oxide Layers on the Microwave Surface Resistance of Superconducting Niobium*. PhD thesis, Cornell University, 1988.
- [123] D. Kostin. private communication.
- [124] X. Singer, J. Iversen, W. Singer, K. Twarowski, B. Spaniol, F. Schoelz, and H.-G. Brokmeier. Material for Fabrication of Large Grain Cavities for European XFEL. In *Proceedings of the 15th International Conference on RF Superconductivity*, 2011.
- [125] W. Weingarten. private communication.
- [126] R. L. Geng. Overview of High Gradient SRF R&D for ILC Cavities at Jefferson Lab. In *Proceedings of the 14th international conference on RF superconductivity*, 2009.
- [127] R. L. Geng, S. Castangnola, C. Crawford, D. Forehand, B. Golden, C. Reece, and S. Williams. Improving gradient and Q performance of BCP etched multi-cell cavities by applying a light EP. In *Proceedings of the 14th international conference on RF superconductivity*, 2009.
- [128] G. Ciovati, G. Myneni, F. Stevie, P. Maheshwari, and D. Griffis. High field Q slope and the baking effect: Review of recent experimental results and new data on Nb heat treatments. *Phys. Rev. ST Accel. Beams*, 13:022002, Feb 2010.
- [129] Z.H. Sung, A. A. Polyanskii, P.J. Lee, A. Gurevich, and Larbalestier. Suppressed Superconductivity on the Surface of Superconducting RF Quality Niobium for Particle Accelerating Cavities. In *AIP Conf. Proc.*, volume 1352, pages 142–150, 2011.
- [130] T. Junginger. private communication.
- [131] F. Schlander and H. Vennekate. Investigations on Improvements of Oscillating Superleak Transducers. Technical report, ILC HiGrade, 2011. <http://www.ilc-higrade.eu/e83212/>.
- [132] W. Pfuetzner. Sputtering of OST diaphragms at Hamburg University.



# Danksagung

Nach nun etwas über 13 Jahren seit dem Entschluss, Physik zu studieren ist sowohl das Studium als auch die Promotion in Physik erfolgreich abgeschlossen. Ich möchte mich bei allen, die mich auf diesem Weg begleitet haben, ganz herzlich bedanken. In allen Höhen und Tiefen, die sowohl Schule, Studium und die Promotion so mit sich brachten, wurde mir der Rücken immer von meinen Eltern frei gehalten. Dafür ein ganz herzliches Dankeschön.

Vielen herzlichen Dank an die Kollegen am Institut für Kernphysik der TU Darmstadt, bei denen ich etwa die Hälfte meines Studiums verbracht habe.

Für das Herstellen der notwendigen Kontakte, um zu DESY zu wechseln, möchte ich mich bei Bernhard Holzer und Hans Weise bedanken.

Direkt hieran folgt ein großes Dankeschön an Eckhard Elsen: Danke für die Betreuung und die ganzen Möglichkeiten, die ich nutzen konnte, um internationale Kontakte mit Kollegen zu knüpfen.

Ein weiteres großes Danke geht an Detlef Reschke, dessen Literaturfundus und Wissen meine Recherchen doch oft erheblich verkürzte.

Für Hilfe beim Aufbau und Einrichtung meines Messaufbaus bedanke ich mich sehr herzlich bei Torsten Külper, Uwe Cornett und Carsten Müller samt Kollegen.

Fragen zu Cavities und den Messapparaturen, oder auch technische Probleme traten und treten natürlich immer wieder auf. Für Antworten und Problemlösungen vielen Dank an Lutz Lilje, Jacek Sekutowicz, Denis Kostin, Krzysztof Twarowski, Arne Brinkmann, Jens Iversen, Daniel Klinke, Wolf-Dietrich Möller, Axel Matheisen, Birte van der Horst, Marco Schalwat, Nico Steinhilber-Kuehl, Andreas Schmidt, Waldemar und Xenia Singer, Jürgen Eschke, Thomas Feldmann, und die ganze MKS Truppe in der Halle 3. Für die Informationen zu statistischer Analyse bedanke ich mich bei Christoph Rosemann.

Für das Lesen und Kommentieren der Frühversionen meiner Dissertation bedanke ich mich bei Tobias Weilbach, Sebastian Jaksch, Aliaksandr Navitski, Lea Steder, Lutz Lilje und Detlef Reschke. Ausserdem ein großes Danke an alle Zuhörer bei den Probevorträgen für die Disputation.

Ein großes Dankeschön geht an Eckhard Elsen, Bernhard Schmidt und Jens Osterhoff, die sich die Zeit genommen haben, die Dissertation und/oder die Disputation zu begutachten. Vielen Dank auch an die Fragesteller Karsten Büßer, Inna Conrad, Denis Kostin, Lutz Lilje, Wolf-Dietrich Möller, Aliaksandr Navitski, Detlef Reschke, Nicholas Walker und Hans Weise, die an meiner Disputation teilgenommen haben.

## Danksagung

---

Ein großer Dank gilt auch allen Kollegen in der Arbeitsgruppe FLA, die ich bei Fragen jederzeit ansprechen konnte. Für messtechnische Fragen und Programmierung fand ich bei Sven Karstensen immer ein offenes Ohr. Des Weiteren konnte ich bei allgemeineren Fragen, insbesondere bei Beschaffungsfragen, immer Gert Falley und Jörn Schaffran 'beschäftigen'.

Danke auch an meine Bürokollegen Marc, Sebastian und Timon, sei es für kurzweilige Unterhaltung während der Arbeit, Diskussionen zu Fragen oder auch für abendliche Programmpunkte, die nichts mit Arbeit zu tun hatten. Für viele nette Abende und Freizeitgestaltung bedanke ich mich ganz herzlich bei Wolf, Dirk, Niladri, Thorben, Björn, Kirsten und Clemens.

Während meiner Zeit bei DESY bestand die Möglichkeit, auch eine Messreihe am CERN durchzuführen. Dafür möchte ich mich bei Tobias Junginger, Kitty Liao, Hannes Vennekate und Wolfgang Weingarten bedanken, die diese Messung ermöglichten. Ausserdem gab es sehr informative Gespräche, die einen Teil dieser Arbeit auch prägten.

Für die Hilfe beim Besputtern der OST Membrane und die Verwendung der Sputteranlage bedanke ich mich bei Wolfgang Pfützner aus der Forschungsgruppe Grenzflächenphysik an der Uni Hamburg.

Special thanks for the possibility to visit the cavity test facility at Cornell University to Georg Hoffstaetter, Zack Conway and Don Hartill. Thank you for providing 8 OSTs and help and support on second sound.